

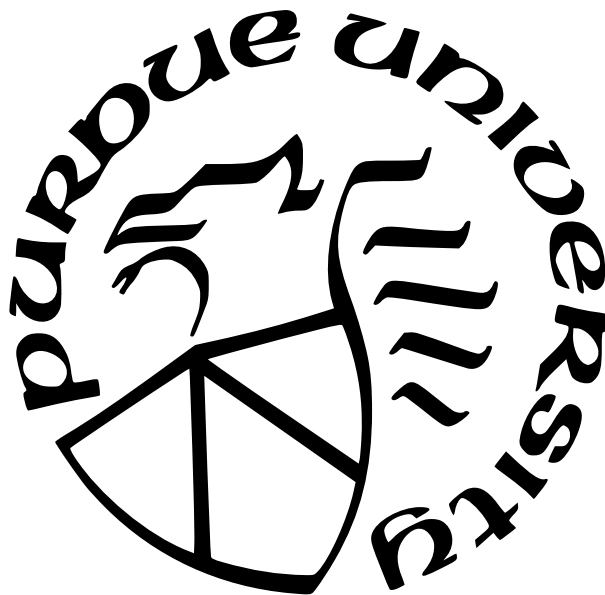
**MULTI-PHOTON IONIZATION STUDIES OF CORRELATION
EFFECTS IN EXCITED ATOMS**

by
Yimeng Wang

A Dissertation

*Submitted to the Faculty of Purdue University
In Partial Fulfillment of the Requirements for the degree of*

Doctor of Philosophy



Department of Physics and Astronomy

West Lafayette, Indiana

May 2022

**THE PURDUE UNIVERSITY GRADUATE SCHOOL
STATEMENT OF COMMITTEE APPROVAL**

Dr. Chris Greene, Chair

Department of Physics and Astronomy

Dr. Francis Robicheaux

Department of Physics and Astronomy

Dr. Daniel Elliott

Department of Physics and Astronomy

Dr. Yulia Pushkar

Department of Physics and Astronomy

Approved by:

Dr. Gabor Csathy

To my parents, who have always been my constant support.

ACKNOWLEDGMENTS

First and foremost, I would like to give my deepest appreciation to my advisor, Prof. Chris H. Greene, for his enthusiastic guidance, patient teaching and constant support during my entire graduate study. I would never have been able to complete the work in this thesis without his help. I am honored to have had the opportunity to work and learn from Chris, whose energetic and hard-working nature has been an inspiration for me on how to grow as a scientist.

I would also like to thank my experimental collaborators, Prof. Dan M. Stamper-Kurn, Prof. Niranjana Shivaram and Dr. Fang Fang, not only for their works, but also for their helpful and fruitful discussions, in which I have greatly benefited from. I would also like to thank Prof. Francis Robicheaux and Prof. Dan Elliott, it is based on their previous projects that I could develop parts of my work. I would further like to extend my thanks to Francis for all of the interesting and knowledgeable discussions during the weekly lunch meetings. I also want to thank my academic colleagues in Greene's group, for all of their help and support during my time in the office. Further, I would like to give thanks to all my committee members for their kind support.

I would also like to thank all my friends who have given me encouragement and provided beneficial suggestions. Last and most importantly, I would like to thank my parents for all of their guidance, love, and support. To them, I dedicate this thesis.

This work was supported financially by the U.S. Department of Energy, Office of Science.

TABLE OF CONTENTS

LIST OF TABLES	8
LIST OF FIGURES	9
ABSTRACT	15
1 INTRODUCTION	16
2 PHYSICS BACKGROUND	18
2.1 Theories	18
2.1.1 Channels and resonances	18
2.1.2 Fano's model for Fano-Feshbach resonance	21
2.2 Solving Schrodinger's equation outside the reaction zone	24
2.2.1 Quantum defect formalism	24
2.2.2 Multi-channel quantum defect theory	27
2.3 A full correlated-electron calculation	29
2.3.1 Streamlined R -matrix method	29
Applications to helium and barium	32
3 APPLICATION TO MULTI-PHOTON IONIZATION	33
3.1 Light-atom interaction and Wigner algebra	33
3.2 Multi-photon ionization of helium	37
3.2.1 Above-threshold ionization	40
Inhomogeneous R -matrix method	40
Integration of free-free transition	42
3.2.2 Gailitis-Damburg treatment of electric dipole moment	43
3.2.3 Spectrum for two-photon ionization	45
Two-photon Linear-polarized ionization	45
Two-photon Trefoil field ionization	48
3.2.4 Spectrum for three-photon ionization	49

3.3	Multi-photon ionization of barium	51
3.3.1	Hyperfine depolarization effects	53
3.3.2	Spectrum for multiphoton ionization	55
4	THE CORRELATION EFFECTS OF ATOMIC HELIUM	58
4.1	Classification scheme	58
4.1.1	Group description of electrons in Coulomb potential	58
4.1.2	Hyperspherical description of electronic correlations	62
4.2	The study of propensity rules	64
5	THE ENTANGLED-PHOTON IONIZATION OF ATOMIC HELIUM	72
5.1	Gedanken experiment inside a spheroid cavity	73
5.1.1	Estimations on correlation time and rate	73
5.1.2	Geometry of the cavity	79
5.2	Experimental set-up and outlooks	82
6	SINGLE-CHANNEL COHERENT CONTROL OF ATOMIC HELIUM	87
6.1	Theoretical description of single channel coherent control	88
6.2	Results	92
6.2.1	Phase- and amplitude- sensitive control	92
6.2.2	Frequency-sensitive control	95
7	MULTI-CHANNEL COHERENT CONTROL AND PHASE LAG OF ATOMIC BARIUM	101
7.1	Background	101
7.1.1	Theoretical description of multi-channel coherent control	102
7.1.2	The blow-up of phenomenological model description	105
7.2	Results	110
8	SUMMARY	114
	REFERENCES	116

A COLD COLLISIONS	128
A.1 Cold collisions of ${}^7\text{Li}$ - ${}^{87}\text{Rb}$ and ${}^6\text{Li}$ - ${}^6\text{Li}$	128
A.2 ${}^7\text{Li}$ - ${}^{87}\text{Rb}$ relaxation experiments	131
A.2.1 Comparison with cross dimensional relaxation experiments	131
A.2.2 Comparison with spin relaxation experiments	135
VITA	137

LIST OF TABLES

3.1	The energies(E) and and decay widths(Γ) for the first three doubly-excited levels lying just below the $N = 2$ threshold (upper) and $N = 3$ threshold (lower), determined by previous works(given by the superscripts) and our calculations. (-x) indicates 10^{-x} . All the unit is in atomic unit(a.u.)	47
7.1	Channels relevant to evaluating equations 7.1-7.5, represented by total angular momentum and parity J_f^π and jj - coupled basis $n_c L_c J_c(l, j)$ (the subscript c denotes ion core). The row “channel a(b)” lists the angular momenta for the fragmentation electron. The row “resonance” gives the angular momenta of the autoionizing states that converge to the $5d_{5/2}$ threshold.	105
7.2	The resonances from our calculation (position E and width Γ) and earlier experiments (Ref. [138, 139]). Most experimental two-photon resonances are missing, because of the strong dominance of $J_f = 1$ partial wave. Our classification of the resonances is shown in the $J_f(nl_j)$ basis. For those overlapped resonances, the upper index of Γ give the J_f	109
A.1	Measured cross-dimensional relaxation rates $\tau^{(ex)}$ and comparisons to theory for several experimental settings. Monte-Carlo simulations for atoms interacting via s-wave-only collisions with an energy-independent cross section, under conditions matching the experimental setting, are used to quantify the cross-dimensional relaxation cross sections $\sigma_{cdr}^{(ex)}$, which matches the experimental relaxation time $\tau^{(ex)}$, and $\sigma^{(th)}$, which matches the theoretically predicted relaxation time $\tau^{(th)}$. This table is from [149].	132
A.2	Candidates with largest and smallest cross section from alternative potentials	132
A.3	Comparison between experiment and theoretical calculations for three spin-dependent collision processes at $50\mu K$. This table is from [150].	136

LIST OF FIGURES

2.1	Schematics of closed and open channels for autoionization (a) and atomic scattering (b) processes. (a). Autoionization of the helium $2s2p$ state. The dashed line gives the total energy for $2s2p$ bound state, which is degenerate with the $1s\epsilon p$ scattering states. (b). A particle flies in from an open channel and transitions to a closed channel in the valence region, forming a long-lived metastable state. Reprint from [18].	20
3.1	Energy diagram of relevant levels in the two-photon ionization of helium. The shaded regions show the energy ranges for the final and intermediate states. (a) Two identical photons $\omega_1 = \omega_2$. The intermediate energies are above the $N = 1$ threshold, and there are no intermediate-state resonances involved, only an open ionization continuum. (b) Trefoil field $\omega_1 = 2\omega_2$. Some of the intermediate states are above threshold, and two intermediate resonances $1s2p$ and $1s3p$ are involved.	38
3.2	Schematic diagram of two-photon ionization channels allowed by electric-dipole selection rules for (a) parallel linearly polarized and (b) two opposite circularly polarized fields. $^{2S+1}L^\pi$ are labeled for each step of ionization. The $^1P^e$ state is a parity-unfavored state whose lowest channel becomes open at the $N = 2$ hydrogenic threshold.	38
3.3	The comparison of calculations with (solid curve) and without (dashed curve) the Gailitis-Damburg dipole term for two-photon ionization cross section up to the $N = 2$ (a) and $N = 3$ (b) threshold. With the Gailitis-Damburg dipole term, the lineshapes change dramatically once the outer electron is outside the box.	44
3.4	Partial cross sections (left) and $\beta_{2,4}$ parameters (right), as given in the label. The energy scale in the two highest panels is shown in terms of single photon energy. The blue points are taken from Boll <i>et al.</i> [59], as are the blue dashed curves for $\beta_{2,4}$. Their calculation is based on a $2 fs$ pulse duration so the narrow resonances are not resolved. The middle and lowest panels show an expanded version of the partial cross sections and $\beta_{2,4}$ parameters near $N = 2$ and $N = 3$ threshold, respectively, and are given on an effective quantum number scale for the outer electron, $\nu = 1/\sqrt{2(E_{N=2} - E_f)}$ and $\nu = 1/\sqrt{2(E_{N=3} - E_f)}$. This figure is taken from Ref.[58].	46
3.5	Combining a right-circularly polarized infrared driver (red arrows) with its left-circularly polarized second harmonic (blue arrows) at equal intensities yields a trefoil-shaped electric field (purple curve), which can guide electrons back to their parent ion to generate high harmonics with controllable polarization. Reprint from [63].	48
3.6	Partial wave cross sections (upper) and $\beta_{1,2,3,4}$ parameters (lower) for trefoil field ionization around $N = 2$ threshold. The parity unfavored state occurs when the energy is above $N = 2$ threshold at -0.5 a.u. The two identified peaks are from the $1s2p$, $1s3p$ intermediate resonance. This figure is taken from Ref.[58].	49

3.7	Three-photon-ionization cross section of helium with identical linearly polarized photons for (a) final state between $N = 2$ and $N = 1$ thresholds, our calculation(solid lines) are compared with Ref.[51](dashed lines); and (b) final state above $N = 2$ threshold.	50
3.8	The quantum defect μ below $N = 3$ threshold is plotted versus the effective quantum number ν for $^1P^o$ (left) and $^1F^o$ (right) wave bound states. The black crosses are the truncated diagonalization calculation from [52]. The grey dashed curve has slope -1 since $\sin \pi(\mu + \nu) = 0$. The resonances are given in terms of $_N(K, T)^A$ quantum numbers	50
3.9	(a) The energy level diagram for the barium for $\omega - 2\omega$ interference scheme. The ground state barium is firstly excited by a linearly-polarized pump laser (ω_p) to $e_1 = 6s6p$ (1P_1) state, then by the concurrent one- and two-photon ionization, the atom reaches the shaded energy region, which can decay into either the continua associated with the $6s_{1/2}$ or the $5d_{3/2}$ ionic state. (b) The angular momenta J and parity π allowed by the electron-dipole selection rule (For the single photon $q = 1$ pathway, replace J_{e_2} by J_f). When the pump and ionization photons are both polarized along z -axis, the red paths are allowed only when the effect from hyperfine depolarization is included in the initially excited e_1 state. This figure is taken from Ref.[64].	52
3.10	Two-photon generalized cross sections for $6s_{1/2}$ (blue) and $5d_{3/2}$ (red). The strong peak around 47549.5 cm^{-1} in the spectrum is due to the existence of an intermediate state resonance $5d7s \ ^3D_1$ state, which has total angular-momentum $J = 1$ and therefore exists only when there is depolarization[39].	56
3.11	The photoelectron angular distribution parameters β_k for ionization process with $q = 1, 2$. Our calculations (solid curves) are compared to the experimental results (points) from Ref. [37] Fig. 6 and 7. Calculations assuming $I = 0$ is given in dashed lines for reference. The left and right panels gives β parameters for channel $6s^{1/2}$ and $5d^{3/2}$. This figure is taken from Ref.[64].	57
4.1	Subtower and complete tower of $SO(4, 2)$ of scaled hydrogenic state. Reprint from Ref. [71], Fig.1.	59
4.2	Possible values of K and T labeling resonance channels of H -like systems for (a) parity favored $\pi = (-1)^L$ and (b) parity unfavored $\pi = (-1)^{L+1}$ states. The lines connecting the points represent channels coupling between \vec{l}_2^2 . Reprint from Ref. [4], Fig.1, 2.	61
4.3	Hyperspherical potential curves for $^1S^e$, $^1P^o$, $^1D^e$, and $^1F^o$ for the helium atom that converge to the He^+ $N=3$ threshold. Reduced units with $Z = 1$ are used, as defined by Lin, namely the horizontal axis has units of Bohr radius divided by $Z = 2$ while the vertical (energy) axis has units of Hartree multiplied by Z^2 . Reprinted from Fig.1. of Lin.[70].	63

- 4.4 A demonstration on photoionization propensity rule for $\Delta T = 1$ and $K = K_{max}$ for $\pi = (-1)^L$ states, the desirable transition from ground state $1(0,0)^+$ are colored in red. Other colors of the lattice indicate different values for $v = \frac{1}{2}(N - 1 - K - T)$ 64
- 4.5 The two-photon ionization partial cross sections for (a) $1S^e$ symmetry and (b) $1D^e$ symmetry are shown for each open channel. The effective quantum number ν is relative to $N = 3$ He⁺ threshold. The $1S^e$ excited state resonances do obey the same photoabsorption propensity rule that was previously found to hold rather accurately for one-photon absorption processes. This figure is taken from Ref.[58]. 66
- 4.6 The three-photon ionization partial cross sections for (a) $1P^o$ symmetry and (b) $1F^o$ symmetry are shown for each open channel. The effective quantum number ν is relative to $N = 3$ He⁺ threshold. The photoabsorption propensity rules for one-photon absorption processes can not be applied to those results. This figure is taken from Ref.[58]. 67
- 4.7 Time delay analysis for $1S^e$. The left figure shows the eigenvalues of the time-delay matrix and the right figure shows partial decay probabilities. The dashed lines give the position for the peaks of q_{tot} , which correspond to resonances $N\{v\}^A$ from left to right, $3\{1\}^+$, $3\{0\}^+$, and $3\{2\}^+$. This figure is taken from Ref.[58]. . 68
- 4.8 Time delay analysis for $1D^e$, as in Fig. 4.7. The $N\{v\}^A$ quantum numbers of the resonances are from left to right, $3\{0\}^-$, $3\{1\}^0$, $3\{2\}^0$, $3\{0\}^+$, $3\{0\}^+$ and $3\{1\}^+$. This figure is taken from Ref.[58]. 68
- 4.9 The quantum defect μ below $N = 3$ threshold is plotted versus the effective quantum number ν for $1S^e$ (left) and $1D^e$ (right) wave bound states. The black crosses are the truncated diagonalization calculation from [52]. The grey dashed curve has slope -1 and each bound state must lie on one of them because of the QDT condition $\sin \pi(\mu + \nu) = 0$. This figure is taken from Ref.[58]. 69
- 4.10 The (a) effective quantum numbers and (b) quantum defects for the doubly-excited levels with same $N(K, T)^A$ but different $^{2S+1}L^\pi$. In each series of $N(K, T)^A$ states ($A \neq 0$). For each rotor series, the levels with higher L lie slightly higher. 70
- 5.1 A schematic diagram of entangled-photon generation and absorption in an spheroid cavity. The emission and absorption atoms are placed in the two foci of the spheroid, the photons are reflected by the boundary of the cavity, and propagate through equal pathway to reach the absorber. The shape of the cavity will influence the rate of this process, by a geometry factor as discussed in Eq.5.12. . 74
- 5.2 Schematic sketch of the absolute value of a typical two-photon wave function in frequency domain and time domain. Recopied from Ref. [79]. 74
- 5.3 (a) The photon correlation function $\langle vac|E(t_2)E(t_1)|2ph\rangle$ (up to a constant factor) as a function of time difference $(t_2 - t_1)$, which indicates the correlation time is around 1.93×10^{-16} sec. (b) An attosecond pump-probe photoionization scheme using entangled bi-photons. 78

5.4	A plot of geometry parameter Θ versus the aspect ratio a/b in an log-log scale. When $a = b$, the cavity is a sphere and the geometry parameter obtained its maximum $\Theta = \frac{64\pi^2}{27}$	81
5.5	Generation of entangled bi-photons in the XUV via two-photon decay of the $1s2s$ 1S_0 state excited by: (a) 4-photon excitation using a narrow band 240 nm laser. (b) Two-step sequential excitation via the $1s2p$ state using a high photon flux helium lamp and a 2059 nm coupling laser. (c) The SCRAP technique using a multiphoton pump pulse and a Stark shifting pulse which enable rapid adiabatic passage.	82
5.6	Proposed experimental scheme to generate XUV entangled photons as described in 5.5 and measure their correlation time. The emitted entangled bi-photons are collected within a large solid angle in a direction orthogonal to the excitation laser propagation direction. The bi-photons are collimated by a toroidal mirror and then split into two independently time delayed paths before being focused by a second toroidal mirror at a target gas jet in a vacuum chamber. Entangled two-photon absorption in helium can be measured as a function of time delay using photon detectors or by collecting helium ions after ionization by a high repetition rate femtosecond laser.	83
6.1	Schematic energy level diagram of helium for the relevant transitions. The He ground state is ionized, with the one and two-photoionization pathways indicated by arrows. The shaded regions show the energy ranges considered for the final and intermediate states, both of which are between the $N = 1$ and $N = 2$ thresholds. The dashed lines give the lowest few bound and autoionizing energy levels[5] below the $N = 1$ and $N = 2$ thresholds, respectively, with $^{2S+1}L^\pi$ spectroscopic labels from left to right as $^1S^e, ^1P^o$ and $^1D^e$. The autoionization levels that are relevant to our calculations are those above the $N = 1$ thresholds. There are no intermediate-state resonances involved in the frequency range considered, only an open ionization continuum. This figure is taken from Ref.[125].	89
6.2	The directional asymmetry α_L versus relative phase $\Delta\Phi$ and the reduced field strength $\chi = \mathcal{E}_\omega^2/\mathcal{E}_{2\omega}$ at an arbitrary single energy. The former shows a sinusoidal modulation, while the latter has a single extremum at χ_0	93
6.3	(a). The solid curve shows the maximized ratio of lower-oriented electrons α_L^{max} obtained by optimizing the reduced field strength $\chi = \mathcal{E}_\omega^2/\mathcal{E}_{2\omega}$ and optical phase $\Delta\Phi$ at each energy. The dashed curve shows the α_L when $\chi = 1$. The background vertical lines give the position of resonances (with different symmetries indicated by different line-types); those positions are near the local minima of the α_L -curves. (b). The directional asymmetry phase φ as the solid curve, namely the optical phase corresponding to α_L^{max} . φ experiences a dramatic change over 2π or $\pm\pi$ across a resonance, which can be traced back to the dipole transition moment phases ϕ_l that are shown as dashed curves. This figure is taken from Ref.[125].	94

- 6.4 The differences in photoelectron directional asymmetry $|\alpha_L^{(1)} - \alpha_L^{(2)}|$ are shown for all possible $(\varepsilon_1, \varepsilon_2)$ from -0.5 a.u. to -0.9 a.u. . $\Delta\Phi$ and χ are chosen to optimize the difference $|\alpha_L^{(1)} - \alpha_L^{(2)}|$ at each value of the two energies on the plane. The bright grids indicate places where the energy pairs have a large angular asymmetry, and they show a close overlap with the “resonance mesh” of horizontal and vertical stripes. The blue point near the S-wave $2p^2$ resonance indicates the energies considered in Fig. 6.5. This figure is taken from Ref.[125]. 96
- 6.5 An example demonstrating how frequency-sensitive control can almost completely redirect the photoelectrons. The parameters are given in the figure. At $\Delta\Phi = 0.63\pi$ (dashed vertical line) $\alpha_L^{(1)} - \alpha_L^{(2)}$ is maximized, with the values marked on the ticks. A polar plot of $\frac{dW(\theta)}{d\Omega}$ using the parameters indicated by the dashed lines is given in the right panel. With two very close frequencies, one that drives most photoelectrons along the polarization axis $+\hat{z}$, while the other opposite to that direction. This figure is taken from Ref.[125]. 97
- 6.6 $\frac{dW}{d\Omega}$ for six energy points between -0.6224 and -0.6213 a.u. , which demonstrates how the PAD changes across the S-wave $2p^2$ resonance at -0.6219 a.u. . When the energy is closest to the resonance energy, its PAD is almost symmetric in both directions. 98
- 6.7 The ionization rate of photoelectron escaping with different kinetic energies($K.E.$), with laser intensities $I_\omega = 2.0 \times 10^{13} \text{ W cm}^{-2}$ and $I_{2\omega} = 1.10 \times 10^{12} \text{ W cm}^{-2}$. $\Delta_{1s,g} = E_{1s} - E_g = 24.58 \text{ eV}$ is the energy difference from the $1s$ threshold and the ground state. The ionization rate at $\omega - \Delta_{1s,g}$ is about 100 times larger than the rate for $2\omega - \Delta_{1s,g}$, which makes it challenging to detect the directional asymmetry properties of the faster electrons, although the two different energies are readily discriminated. This figure is taken from Ref.[125]. 99
- 7.1 (a) Energy level diagram for the barium $\omega - 2\omega$ interference scheme starts from $e_1 = 6s6p (^1P_1)$ state (for full ionization steps, see Fig.3.9). The excited atom can decay into either the continua associated with the $6s_{1/2}$ or the $5d_{3/2}$ ionic state. The relevant threshold energy levels are given in the figure in atomic unit and cm^{-1} . (b) The angular momenta J and parity π allowed by the electron-dipole selection rule with all photons polarized along z-axis, as introduced in Fig.3.9. The quantum numbers in green and red give the final states for the one- and two-photon ionizations. 102
- 7.2 Recopy of Fig. 11 and 12 in Ref.[37]. Left panel: Resulting phase lag between the two photoionization channels calculated using the autoionizing parameters presented in Ref.[37], Tables I and II. Locations of resonances are marked with dashed and solid arrows at the top. Right panel: Calculated phase lag due to the variation of the outgoing electron waves. First row, ϕ_0 variation for the fast-electron channel; second row, ϕ_0 variation for the slow-electron channel; third row, ϕ_0 variation. The variation of the phase lag was calculated to be as large as 210° 106

7.3	Comparison of our calculated phase lag $\Delta\delta = \delta_0^{(a)} - \delta_0^{(b)}$ (solid curve) with the experimental results [38] (blue points) versus energy in cm^{-1} . The top label gives the effective quantum number $\nu = [2(E_{5d_{5/2}} - E)]^{-\frac{1}{2}}$. The dashed curves are δ_0 for $a = 6s_{1/2}$ (upper) and $b = 5d_{3/2}$ (lower) channels. The arrows and the diamonds on the top and bottom give the positions of the two- and one-photon resonances, and their colors correspond to the colors in Fig. 7.4. This figure is taken from Ref.[64].	108
7.4	Partial cross-sections for two- and one-photon ionization, separately. The solid (dashed) curves give partial cross sections for $a = 6s_{1/2}$ ($b = 5d_{3/2}$) channel. Resonance identification and their comparisons with experiment are given in Table. 7.2. This figure is taken from Ref.[64].	111
7.5	Time delay analysis for $J_f^\pi = 1^o$ resonances. The upper figure shows the eigenvalues of the the time-delay matrix and the lower figure shows partial decay probabilities.	112
7.6	Time delay analysis for $J_f^\pi = 2^e$ resonances. The upper figure shows the eigenvalues of the the time-delay matrix and the lower figure shows partial decay probabilities.	113
A.1	Threshold energies for (a) ${}^7\text{Li}{}^{87}\text{Rb}$ for $M = -2$ manifold for arbitrary L and (b) ${}^6\text{Li}_2$ for $M = 0, -1, -2$ and -3 manifold for $L = 0, 1$. The dashed curves are the entrance channels in the experiments we compared with.	129
A.2	(a) Threshold energies single ${}^6\text{Li}$ atom. (b) The s-wave scattering length near the ${}^6\text{Li}_2$ resonances for 1+3, 2+3,and 1+2 collision, our calculations (dashed lines) agree with the calculations from Ref. [141] supplemental material (solid lines).	130
A.3	Comparison of theoretical and experimentally determined cross section. Solid blue(orange) line is s(p) wave ${}^7\text{Li}{}^{87}\text{Rb}$ interspecies cross section calculated by quantum defect theory(QDT). Red circles represent σ_{cdr} determined by experimental measurements. Error bars are statistical. Blue circles are σ_{cdr} determined by Monte Carlo simulation using the theoretical differential cross section. Both the experimental and theoretical points are placed at the averaged collisional energy under experimental condition. Inset: Determine σ_{cdr} at through matching. Solid black spots are Monte-Carlo simulated results. The solid blue line is a linear fit: $\tau = k/\sigma_{cdr}$. The red circle represents experimental result. The blue circle represents Monte Carlo simulation. Reprint from [149].	133

ABSTRACT

Based on the multichannel quantum defect method and streamlined R -matrix treatment, this thesis studies the multi-photon ionization spectrum for atomic helium and barium, and explores the electronic correlations of these atoms. For the helium atom, the above-threshold-ionization spectra have been calculated, with two linearly polarized photons, two oppositely circularly polarized photons, and three linearly polarized photons. The propensity rules for the single-photon ionization and autoionizing decay have been extended into the multi-photon region, showing that the excitation rules are not always satisfied for the most prominent channel. In a separate project, based on the spontaneous two-photon decay of the helium $1s2s\ ^1S^e$ excited state that has a rather long lifetime, one can create photon pairs that are entangled in time, frequency, and polarization. Experimental schemes are proposed to use them as a laser source to ionize another helium. Finally, we considered the one- and two-photon pathway coherent control of atomic helium and barium near their autoionizing levels. For the helium atom, we proposed a controlling scheme that can flip 90 % of the photocurrent by a slight change of laser frequency. For the barium atom, we computed the phase lag between $6s_{1/2}$ and $5d_{3/2}$ ionization continua, which agrees with the experimental results that a previous phenomenological model failed to reproduce. Our treatment also develops formulas to describe the effects of hyperfine depolarization on multiphoton ionization processes, and it identifies resonances that had not been observed and classified in previous experiments.

1. INTRODUCTION

Electron correlations in atoms with two active electrons have been the topic of many theoretical studies[1, 2, 3, 4, 5, 6, 7, 8, 9, 10], because the ability to solve a classic quantum three-body problems where long-range correlations exist between the particles can be the foundation of solving other strong correlation systems. The properties of correlated electrons in those atoms can be approached by photoionization spectroscopy. However, their multichannel spectra often exhibit extraordinary complexity which requires a powerful and practical approach to explain them.

The first calculation of multichannel spectra was conducted within a close-coupling framework by Burke and Smith [11]. Since that work, two major developments have greatly enhanced those calculations, one is the multichannel quantum-defect theory (MQDT) developed by Seaton [6, 7], the other is the implementation of the R -matrix approach[12, 13, 14, 15, 16, 17]. In this thesis, we present calculations of atomic spectra based on MQDT and the R -matrix method, which can reproduce the spectra involved and provide a simple interpretation of those seemingly irregular resonant spectra and their underlying electron dynamics.

The dissertation is organized as follows. Chapter 2 reviews the basic theory and methods we used to solve the Schrodinger equations relevant to the photoionization projects; those methods include the MQDT and R -matrix method; Chapter 3 introduces the way those techniques are being applied to calculate the spectroscopy and ionization cross sections for atomic helium and barium, with more than one open channels involved. Chapters 4-6 focus on the spectroscopy properties of helium: In Chapter 4 we discuss the electronic correlation and extend the propensity rule, which guides the single-photon ionization of helium, into multi-photon regime. Chapter 5 raises a possible source to generate entangled-photon pairs, based on the spontaneous two-photon decay of an initially-excited helium atom; we demonstrate applicable experimental set-ups for this proposal. Chapter 6 explores the one- and two-photon coherent control of helium, to demonstrate interference of optical pathways into photoelectron angular distributions. In Chapter 7 we study the spectroscopy properties of barium, aiming to reproduce the phase-lag behavior from one- and two-photon coherent con-

trol from experiments, which were not correctly predicted by a previous phenomenological model. Chapter 8 summarizes this dissertation. The appendix includes our calculations on cold collisions of two alkali-metal atoms, especially, calculations for ${}^7\text{Li}{}^87\text{Rb}$ are compared with a cross-dimensional relaxation experiment and spin relaxation experiment.

2. PHYSICS BACKGROUND

This chapter will introduce the basic concepts (Sec.2.1) and methods (Sec.2.2 and 2.3) used in this thesis. Sec.2.1 introduces the multi-channel picture and Fano-Feshbach resonance. Then the Sec.2.2 and Sec.2.3 demonstrate the methods we used to solve the two-electron time independent Schrodinger equation, with different methods depending on whether the outermost electron is outside (Sec.2.2) or inside (Sec.2.3) the reaction zone. We use atomic units unless otherwise specified ($\hbar = e = m_e = 1$) throughout this thesis.

2.1 Theories

2.1.1 Channels and resonances

In this subsection, we will introduce the basic ideas about atomic spectroscopy. Many widely-used concepts, such as channels and resonances, come from the scattering theory, which is the starting point of our discussion. Later we will demonstrate how parallels can be drawn between the scattering theory and atomic spectroscopy, and how a family of resonances with similar characteristics can be approached by a multi-channel picture.

A particle being studied by the scattering theory would start and end at positions far away from all the interactions: $V(r) \rightarrow 0$ ($r \rightarrow \infty$), whose asymptotic radial wave function can be parameterized as:

$$\begin{cases} j_l(kr) \xrightarrow{r \rightarrow \infty} \frac{1}{2kr} [e^{i(kr - (l+1)\pi/2)} + e^{-i(kr - (l+1)\pi/2)}] & \text{no scattering, } V(r) \equiv 0 \\ \psi_l(r; k) \xrightarrow{r \rightarrow \infty} \frac{1}{2kr} [e^{-i(kr - l\pi/2 + \delta_l(k))} - e^{i(kr - l\pi/2 + \delta_l(k))}] \end{cases} \quad (2.1)$$

Here we fixed the angular momentum l (since only an isotropic potential $V(r)$ is considered, unless otherwise specified). A phase-shift $\delta_l(k)$ could parameterize all the information about the interaction potential $V(r)$ (For simplicity we assume the background phaseshift $\delta_{bg} = 0$). $\delta_l(k)$ gives the difference between a scattering wave function $\psi_l(r; k)$ and the radial component of a plane wave $e^{i\vec{k} \cdot \vec{r}}$. It defines the scattering matrix $S^{phys} = e^{2i\delta_l(k)}$, which will be widely used in our spectroscopy calculations.

In addition, a bound atom can be described in a scattering picture, only that the energy of an incident electron is less than the binding potential energy at infinity. The complicated electron-core interaction can then be represented by the “quantum defect” μ_l , which modifies the Rydberg spectrum for alkali atoms as:

$$E_n = -\frac{1}{2n^2} \rightarrow E_n = -\frac{1}{2(n - \mu_l)^2}$$

The quantum defect μ_l has only weak dependence with energy, and equals to the zero-energy limit of the scattering phase shift $\delta_l(k)$: $\delta_l(k) \xrightarrow{k \rightarrow 0} \pi\mu_l$ (Seaton’s Theorem). This reveals the fact that, although a small change of energy can be important to the scattering processes, at a short distance where the kinetic energy of the particle is extremely large, the physics will be not sensitive to a small change of energy, therefore the system can be described by such a nearly energy-independent parameter.

For more complicated atoms such as the alkaline earths, the situation becomes even more complicated and interesting. Besides the Coulomb interaction from the nonhydrogenic ionic core, a strong correlation $\frac{1}{|r_1 - r_2|}$ couples the two outermost electrons, which endows those atoms with a much more complicated spectrum: More than one Rydberg series exist and their energy levels converge to different ionization thresholds, and sometimes they affect each other[1]. The asymptotic behavior of a scattered electron in those atoms can be described by the multichannel quantum defect theory (MQDT), which was generalized by Seaton from single-channel quantum defect theory[7].

In this thesis, we study the problems relevant to the single ionization of atoms with two active electrons, where one of the electrons stays close to the ion core (electron 1), while the other (electron 2) escapes very far away (the energy range we considered is far below the double ionization threshold, and in that range only one of the electrons is able to leave the ionic core). To tackle those doubly-excited states, we divide the system into two parts, a short-ranged reaction zone (when the outermost electron $r_2 < R_0$), and a long-ranged zone ($r_2 > R_0$), by assuming an artificial box with a large radius R_0 , the electronic correlation is only regarded inside the box($r_2 < R_0$). Once an electron leaves the reaction zone, it feels an overall interaction from the other part of the system and behaves just like in the field of an

alkaline atom. The Hamiltonian of the system is approximated in the outermost region to be asymptotically separable, as is demonstrated below for the Hamiltonian of helium:

$$H_0(\vec{r}_1, \vec{r}_2) = \sum_{i=1,2} \left(-\frac{\nabla_{\vec{r}_i}^2}{2} - \frac{2}{r_i} \right) + \frac{1}{|\vec{r}_1 - \vec{r}_2|} \xrightarrow{r_2 > R_0} \left(-\frac{\nabla_{\vec{r}_1}^2}{2} - \frac{2}{r_1} \right) + \left(-\frac{\nabla_{\vec{r}_2}^2}{2} - \frac{1}{r_2} \right) \quad (2.2)$$

$$H_0(\vec{r}_1, \vec{r}_2)\Psi(\vec{r}_1, \vec{r}_2) = E\Psi(\vec{r}_1, \vec{r}_2) \quad E = E^{thresh} + \varepsilon$$

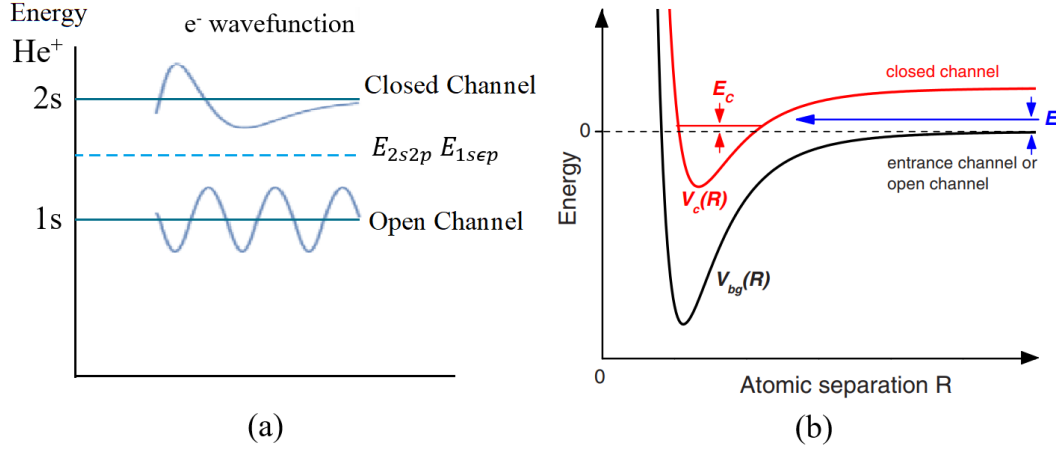


Figure 2.1. Schematics of closed and open channels for autoionization (a) and atomic scattering (b) processes. (a). Autoionization of the helium $2s2p$ state. The dashed line gives the total energy for $2s2p$ bound state, which is degenerate with the $1s\epsilon p$ scattering states. (b). A particle flies in from a open channel and transitions to a closed channel in the valence region, forming a long-lived metastable state. Reprint from [18].

The idea of a “channel” is introduced to describe the asymptotic Hamiltonian by an independent-electron picture, with the total wave function written as the sum of products of two separate factors, $\Psi(\vec{r}_1, \vec{r}_2) \xrightarrow{r_2 > R_0} \sum_i \Phi_i(\vec{r}_1, \Omega_2)\psi_i(r_2)/r_2$ (the channel function $\Phi_i(\vec{r}_1, \Omega_2)$ describes the motion of electron 1 and the angular motion of electron 2). Within each channel, electron 1 is simply in a hydrogenic state, while electron 2 can be parameterized by the quantum defect parameters and standard Coulomb wavefunctions. The total energy can be separated into E_i^{thresh} and ε_i for each channel, which are respectively the energy carried by $\Phi_i(\vec{r}_1, \Omega_2)$ and by $\psi_i(r_2)$. ε_i can be positive ($\varepsilon_i = \frac{k_i^2}{2}$) or negative ($\varepsilon_i = -\frac{1}{2\nu_i^2}$), depending on whether that channel is open or closed. For a closed channel ($E < E_i^{thresh}$), there will be

a full series of Rydberg states converging to the threshold ($\varepsilon_i = -\frac{1}{2\nu_i^2}$ with $\nu_i \rightarrow \infty$). For an open channel ($E > E_i^{thresh}$), $\psi_i(r_2)$ will be modified by a Coulomb phase shift η_i , and a short-ranged phase shift $\pi\tau_i$, whose details can be found in subsection. 2.2.1.

Fig.2.1 demonstrates the situation when the total energy E lies between two channel thresholds. When ε_i approaches one of the Rydberg series $-\frac{1}{2\nu_i^2}$, $\Psi(\vec{r}_1, \vec{r}_2)$ will be a superposition of a bound state and continuum states, which is a so-called autoionization state, a state where an atom can ionize automatically without the aid of photons. As demonstrated by Fig.2.1(a), the atom was first pumped onto the doubly excited state $2s2p$, where both the electrons stay in the $n = 2$ shell. The strong repulsion between them would drive one of the electrons very far away, while the other deexcites into $1s$ shell. Fig.2.1(b) shows a quasi-bound state in an atom-atom collision (which will be discussed in the Appendix), where an atom flies in from an open channel to approach the other atom. The correlation between them will excite their internal degrees of freedom (spin) to a higher level, trapping the two atoms with each other into a metastable state which has a rather long lifetime [19]. Both processes will present a strong feature experimentally, the ‘‘Fano-Feshbach resonance’’. In the next subsection, we will introduce Fano’s model for the resonance, and demonstrate how the autoionizing states and scattering states can interfere with each other and exhibit a dip or an asymmetrical ‘‘Fano lineshape’’.

2.1.2 Fano’s model for Fano-Feshbach resonance

Two principal categories of resonances can be observed in experiments: the shape resonances and the Fano-Feshbach resonances[20]. Shape resonances can be observed when the de Broglie wavelength of the particle matches the distance between the two turning points of the potential barrier, and therefore establish a standing wave pattern and become a metastable state. Fano-Feshbach resonances, as already demonstrated by Fig. 2.1, come from the correlation between the particles, in which a single bound state is embedded in the continuum and forms a long-lived metastable state.

In this subsection, we will introduce Fano’s theory and demonstrate how a discrete bound state $|\phi\rangle$ embedded in the continuum $\{|\varepsilon\rangle\}$ can cause an asymmetrical Fano-Feshbach line-

shape[21]. The idea of discrete-continuum interactions raised by Fano has been widely used in different fields, such as the “Anderson impurity model” in condensed-matter physics[22], and the “unified theory of nuclear reactions” of Feshbach[23]. Following Fano’s formalism, we consider the relevant matrix elements between $|\phi\rangle$ and energy-normalized states $\{|\varepsilon\rangle\}$, connected by the autoionization Hamiltonian H whose matrix elements are:

$$\langle\varepsilon'|H|\varepsilon\rangle = \varepsilon\delta(\varepsilon - \varepsilon') \quad \langle\phi|H|\phi\rangle = \varepsilon_\phi \quad \langle\phi|H|\varepsilon\rangle = V_\varepsilon \quad (2.3)$$

The set of $|\phi\rangle$ and $\{|\varepsilon\rangle\}$ are complete and orthogonal with each other. The energy eigenstate $|\Psi_E\rangle$ can therefore be expanded into this complete set as,

$$|\Psi_E\rangle = a(E)|\phi\rangle + \int d\varepsilon' b_{\varepsilon'}(E)|\varepsilon'\rangle \quad (2.4)$$

By projecting $\langle\varepsilon|$ onto the Schrodinger equation $H|\Psi_E\rangle = E|\Psi_E\rangle$, the coefficient $b_\varepsilon(E)$ can be expressed as,

$$b_\varepsilon(E) = \frac{V_\varepsilon}{E - \varepsilon} a(E) \Rightarrow b_\varepsilon(E) = \left[\frac{\mathcal{P}}{E - \varepsilon} + \pi\eta(E)\delta(E - \varepsilon) \right] V_\varepsilon a(E) \quad (2.5)$$

The right-hand side isolates out the singularity at $E = \varepsilon$ by writing it into the principal value \mathcal{P} and a delta function. The real parameter $\eta(E)$ can be obtained from the self-consistency requirement. By projecting $\langle\phi|$ onto the Schrodinger equation, one can obtain,

$$\varepsilon_\phi a(E) + \int d\varepsilon' V_{\varepsilon'} b_{\varepsilon'}(E) = E a(E) \quad (2.6)$$

The autoionizing energy eigenstate given by Fano’s model is,

$$\begin{aligned} |\Psi_E\rangle &= a(E) \left[|\phi\rangle + \pi\eta(E)V_E|\varepsilon\rangle + \int d\varepsilon' \frac{\mathcal{P}}{E - \varepsilon'} V_{\varepsilon'} |\varepsilon'\rangle \right] \\ \eta(E) &= \frac{E - \varepsilon_\phi - F(E)}{\pi|V_E|^2} \quad F(E) = \mathcal{P} \int d\varepsilon' \frac{|V_{\varepsilon'}|^2}{E - \varepsilon'} \end{aligned} \quad (2.7)$$

$|E\rangle$ is the primitive basis continuum state whose energy lies at the delta function singularity, $\delta(E - \varepsilon)$. The coefficient $a(E)$ can be obtained from the energy normalization condition: $\langle \Psi_{E'} | \Psi_E \rangle = \delta(E' - E)$, as:

$$|a(E)|^2 = \frac{1}{\pi^2 |V_E|^2 (\eta(E)^2 + 1)} = \frac{|V_E|^2}{[E - \varepsilon_\phi - F(E)]^2 + \pi^2 |V_E|^4} \quad (2.8)$$

The single bound state $|\phi\rangle$ in Eq. 2.7 is admixed into the continuum as a Lorentzian which peaks at the resonance energy $E_{res} = \varepsilon_\phi + F(E)$, with full width of the half maximum (FWHM) $\Gamma = 2\pi |V_E|^2$. The autoionizing eigenstate $|\Psi_E\rangle$ can be written into the superposition of two parts, one is the continuum-modified discrete state $|\Phi\rangle = |\phi\rangle + \mathcal{P} \int d\varepsilon \frac{V_\varepsilon}{E - \varepsilon} |\varepsilon\rangle$, the other is the flat continuum state $|E\rangle$, as following:

$$|\Psi_E\rangle = |\Phi\rangle \frac{1}{\pi V_E^*} \sin \Delta(E) - |E\rangle \cos \Delta(E) \quad (2.9)$$

The phase-shift $\Delta(E)$ are defined by: $\tan \Delta(E) = -1/\eta(E)$. Now we consider a photoionization process, that an atom transit from initial state $|i\rangle$ to a continuous state $|E\rangle$. Two ionization pathways are involved: the direct transition $|i\rangle \rightarrow |E\rangle$, and resonance-mediated transition $|i\rangle \rightarrow |\Phi\rangle \rightarrow |E\rangle$. The interference between the paths can change the lineshape of the resonance from a symmetric Lorentzian into the asymmetric Fano lineshape, which is controlled by a Fano- q parameter, defined by the relative strength of the two pathways. The transition probability into the autoionizing eigenstate $|\Psi_E\rangle$ can be rearranged into the transition probability into flat continuum $|E\rangle$ multiplying a factor:

$$|\langle \Psi_E | T | i \rangle|^2 = |\langle E | T | i \rangle|^2 \frac{(q + \tilde{\varepsilon})^2}{1 + \tilde{\varepsilon}^2} = |\langle E | T | i \rangle|^2 (\cos \Delta(E) - q \sin \Delta(E))^2 \quad (2.10)$$

$$q = \frac{\langle \Phi | T | i \rangle}{\pi V_E^* \langle E | T | i \rangle} \quad \tilde{\varepsilon} = \frac{E - E_{res}}{\Gamma/2} = -\cot \Delta(E)$$

From the equation above, $q \rightarrow \infty$ indicates a Lorentzian lineshape, when the direct transition is negligible compares to the resonance-mediated transition. $q = 0$ indicates a window resonance that exhibits a dip at $E = E_{res}$, because the resonance-mediated transition is forbidden, and coupling V_E would move the population from continuum to the metastable

bound state. In Chapter 7 we will compare the direct and resonance-mediated transitions, as a phenomenological model to address the coherent control and phase lag properties in atomic barium.

2.2 Solving Schrodinger's equation outside the reaction zone

2.2.1 Quantum defect formalism

Before introducing the multichannel quantum defect theory (MQDT) to study the electronic correlation, in this subsection, we consider only a single channel and demonstrate how quantum defect theory works in solving the asymptotic radial wave function for a single electron in a Coulomb potential with an attractive or repulsive dipole term [24, 25, 26]:

$$-\frac{\psi''(r)}{2} + \left[-\frac{1}{r} + \frac{l(l+1)}{2r^2} \right] \psi(r) = \varepsilon \psi(r) \quad (2.11)$$

The wavefunction can be written as $\psi(r) = f(r) \cos(\pi\mu_l) - g(r) \sin(\pi\mu_l)$, where $f(r)$ and $g(r)$ are real regular and irregular solutions of Eq. 2.11. When $\varepsilon \geq 0$, $\pi\mu_l$ equals to the usual scattering phase-shift, otherwise, μ_l parameterizes the bound-state energy $\varepsilon_n = -\frac{1}{2(n-\mu_l)^2}$. As $\mu_l \rightarrow 0$, the system turns from a “defective” non-hydrogenic atom into a “perfect” hydrogenic atom. A proper choice of (f, g) can simplify the MQDT formalism. In principle, any two regular and irregular linear-independent solutions to Eq.2.11 should work. However, to avoid non-physical singularities and non-analytical or rapid energy-dependence that can cause difficulty in numerical evaluation, the basis function (f, g) is chosen to obey the following[7]:

1. $f \rightarrow 0$ as $r \rightarrow 0$
2. When $\varepsilon \geq 0$, (f, g) are always linear independent to the maximum extent:

$$\begin{aligned} f &\xrightarrow{r \rightarrow \infty} \sqrt{\frac{2}{\pi k}} \sin [kr + \ln(kr)/k + \eta] \\ g &\xrightarrow{r \rightarrow \infty} -\sqrt{\frac{2}{\pi k}} \cos [kr + \ln(kr)/k + \eta] \end{aligned} \quad (2.12)$$

3. When $\varepsilon < 0$, (f, g) join smoothly onto $\varepsilon \geq 0$:

$$\begin{aligned} f &\xrightarrow{r \rightarrow \infty} \sqrt{\frac{\nu}{\pi}} (\sin \beta D^{-1} r^{-\nu} e^{r/\nu} - \cos \beta D r^{\nu} e^{-r/\nu}) \\ g &\xrightarrow{r \rightarrow \infty} -\sqrt{\frac{\nu}{\pi}} (\cos \beta D^{-1} r^{-\nu} e^{r/\nu} + \sin \beta D r^{\nu} e^{-r/\nu}) \end{aligned} \quad (2.13)$$

Now we consider the case when there is no dipole interaction, that l is a non-negative integer. To avoid the energy analytical problems across $\varepsilon = 0$, we consider analytical solutions, whose lowest order in the expansion of ν (or i/k) is normalized to be the 0 th order:

$$f_0(r) = \begin{cases} \frac{\nu^{l+1}}{(2l+1)!} M_{\nu, l+\frac{1}{2}}(2r/\nu) & \varepsilon = \frac{-1}{2\nu^2} < 0 \\ \frac{i^{l+1}}{k^{l+1}(2l+1)!} M_{i/k, l+\frac{1}{2}}(-2ikr) & \varepsilon = \frac{k^2}{2} \geq 0 \end{cases} \quad (2.14)$$

The analytical solution g_0 is a linear combination of Whittaker M and Whittaker W functions, $Wrons[f_0(r), g_0(r)] = f_0'(r)g_0(r) - f_0(r)g_0'(r) = 2/\pi$, being maximal linearly independent with f_0 . When ε is far below the threshold, (f_0, g_0) can be used as an alternative pair of (f, g) . The analytical basis (f_0, g_0) are connected to (f, g) by r -independent parameters:

$$\begin{cases} f^{(\nu)}(r) = A^{1/2} f_0(r), & g^{(\nu)}(r) = A^{-1/2} g_0(r) & \varepsilon = \frac{-1}{2\nu^2} < 0 \\ f^{(k)}(r) = B^{1/2} f_0(r), & g^{(k)}(r) = B^{-1/2} [g_0(r) + \mathcal{G} f_0(r)] & \varepsilon = \frac{k^2}{2} \geq 0 \end{cases} \quad (2.15)$$

which are:

$$\begin{aligned} A &= \frac{\Gamma(l+1+\nu)}{\nu^{2l+1}\Gamma(\nu-l)} \quad (\nu > l) & B &= \frac{k^{2l+1}e^{\pi/k}}{2\pi} |\Gamma(l+1-i/k)|^2 \quad \mathcal{G} = 0 \\ \eta &= \frac{\ln 2}{k} - \frac{l\pi}{2} + \text{arg} \left[\Gamma \left(l+1 - \frac{i}{k} \right) \right] & \beta &= \pi(\nu-l) \end{aligned} \quad (2.16)$$

The phase shifts η and β are chosen to force the physical solution $\psi(r)$ to satisfy the incoming wave boundary condition when $\varepsilon > 0$ (see Ref.[27]), satisfies the decaying boundary condition when $\varepsilon < 0$:

$$\begin{aligned} \psi(r) &\xrightarrow{r > R_0} f(r) \cos \beta + g(r) \sin \beta \\ &= \nu^{3/2} [\nu^2 \Gamma(l+1+\nu) \Gamma(\nu-l)]^{-1/2} W_{\nu, l+\frac{1}{2}}(2r/\nu) \xrightarrow{r \rightarrow \infty} e^{-r/\nu} \end{aligned} \quad (2.17)$$

When both the dipole and centripetal term exist and result in an overall repulsive potential in Eq.2.11, l is still a real number, but not an integer. The QDT parameters (Eq. 2.16) and $f_0(r)$ (Eq.2.14) for integer l can be extended into non-integer and non-half-integer case (we denote them as $f_0(l, r)$ and A_l etc.). Note that $f_0(l, r)$ and $f_0(-l - 1, r)$ are two linear-independent solutions of Eq.2.11, and (f, g) can be determined as,

$$\begin{cases} f^{(\nu)}(l, r) = A_l^{1/2} f_0(l, r) \\ g^{(\nu)}(l, r) = \frac{1}{\sin(\beta_l - \beta_{-l-1})} \left[-A_l^{1/2} f_0(l, r) \cos(\beta_l - \beta_{-l-1}) + A_{-l-1}^{1/2} f_0(-l - 1, r) \right] \\ f^{(k)}(l, r) = B_l^{1/2} f_0(l, r) \\ g^{(k)}(l, r) = \frac{1}{\sin(\eta_l - \eta_{-l-1})} \left[-B_l^{1/2} f_0(l, r) \cos(\eta_l - \eta_{-l-1}) + B_{-l-1}^{1/2} f_0(-l - 1, r) \right] \end{cases} \quad (2.18)$$

When the dipole and centripetal term result in an overall attractive potential, the ‘‘angular momentum’’ becomes a complex number, $l = -\frac{1}{2} + i\alpha$. The maximal linearly independent analytical basis functions are,

$$\begin{cases} f_0(\alpha, r) = \begin{cases} \frac{1}{\sqrt{\alpha\pi}} \text{Im}[\nu^{\frac{1}{2} + i\alpha} M_{\nu, i\alpha}(2r/\nu)] \xrightarrow{r \rightarrow \infty} J_f^+ r^\nu e^{-r/\nu} + J_f^- r^{-\nu} e^{r/\nu} \\ \frac{1}{\sqrt{\alpha\pi}} \text{Im}[(i/k)^{\frac{1}{2} + i\alpha} M_{i/k, i\alpha}(-2ikr)] \xrightarrow{r \rightarrow \infty} f_0^{asy}(\alpha, r) \end{cases} \\ g_0(\alpha, r) = \begin{cases} -\frac{1}{\sqrt{\alpha\pi}} \text{Re}[\nu^{\frac{1}{2} + i\alpha} M_{\nu, i\alpha}(2r/\nu)] \xrightarrow{r \rightarrow \infty} J_g^+ r^\nu e^{-r/\nu} + J_g^- r^{-\nu} e^{r/\nu} \\ -\frac{1}{\sqrt{\alpha\pi}} \text{Re}[(i/k)^{\frac{1}{2} + i\alpha} M_{i/k, i\alpha}(-2ikr)] \xrightarrow{r \rightarrow \infty} g_0^{asy}(\alpha, r) \end{cases} \end{cases} \quad (2.19)$$

The negative energy QDT parameter can be obtained from $f_0(\alpha, r) \cos \beta_\alpha + g_0(\alpha, r) \sin \beta_\alpha \rightarrow e^{-r/\nu}$,

$$\tan \beta_\alpha = \frac{i \left[\nu^{1/2 - i\alpha} \Gamma(1 - 2i\alpha) \Gamma(1/2 + i\alpha - \nu) - \nu^{1/2 + i\alpha} \Gamma(1 + 2i\alpha) \Gamma(1/2 - i\alpha - \nu) \right]}{\nu^{1/2 - i\alpha} \Gamma(1 - 2i\alpha) \Gamma(1/2 + i\alpha - \nu) + \nu^{1/2 + i\alpha} \Gamma(1 + 2i\alpha) \Gamma(1/2 - i\alpha - \nu)} \quad (2.20)$$

$$A_\alpha = 1$$

For positive energy, since $f_0^{asy}(dg_0^{asy})(\alpha, r)$ and $g_0^{asy}(df_0^{asy})(\alpha, r)$ are oscillatory and proportional to $\sin(kr + \delta_{bg})$ and $\cos(kr + \delta_{bg})$, the r -independent QDT parameters can be obtained by the following formulas (in the following formulas, $r \rightarrow \infty$),

$$\begin{aligned} B_\alpha &= \frac{\pi}{2} \frac{f_0^{asy}(\alpha, r)^2 + df_0^{asy}(\alpha, r)^2}{k} & \eta_\alpha &= \tan^{-1} \left[\frac{df_0^{asy}(\alpha, r)}{kf_0^{asy}(\alpha, r)} \right] - (kr + \ln kr/k) \\ \mathcal{G}_\alpha &= B_\alpha^{-1} \tan \left\{ \tan^{-1} \left[\frac{df_0^{asy}(\alpha, r)}{kf_0^{asy}(\alpha, r)} \right] - \tan^{-1} \left[\frac{dg_0^{asy}(\alpha, r)}{kg_0^{asy}(\alpha, r)} \right] \right\} \end{aligned} \quad (2.21)$$

2.2.2 Multi-channel quantum defect theory

In this subsection we continue the discussion on the asymptotic wavefunction $\Psi(\vec{r}_1, \vec{r}_2)$ for alkaline earth atoms. Although we have neglected the correlation and described the system asymptotically by a separable Hamiltonian (Eq.2.2), the effect of the correlation persists in its wavefunction, by the mixing of different channels. The asymptotic wavefunction can be written as a summation of different channels, $\Psi(\vec{r}_1, \vec{r}_2) \xrightarrow{r > R_0} \mathcal{A} \sum_i \Phi_i(\vec{r}_1, \Omega_2) \psi_i(r_2)/r_2$, each channel describes a different free particle limit of the system with energy E_i^{thresh} and $\varepsilon_i = E - E_i^{thresh}$. As we have shown in the last subsection, in the single channel picture, $\psi(r) = f(r) \cos \pi\mu_l - g(r) \sin \pi\mu_l$, the quantum defect μ_l determines all the information about the potential inside the reaction zone $V(r < R_0)$. In multi-channel systems where there are total N channel functions $\Phi_i(\vec{r}_1, \Omega_2)$, for any energy E , the number of degenerate solutions $\Psi_\beta(\vec{r}_1, \vec{r}_2)$ equals to the number of channel functions:

$$\Psi_\beta(\vec{r}_1, \vec{r}_2) = \mathcal{A} \left[r_2^{-1} \sum_{i=1}^N \Phi_i(\vec{r}_1, \Omega_2) \psi_{i\beta}(r_2) \right] \quad (2.22)$$

The multi-channel quantum defect theory (MQDT) treats the $N \times N$ fragmented wavefunction matrix $\psi_{i\beta}(r)$ instead of a single function $\psi(r)$. One can expand $\psi_{i\beta}(r)$ into the regular and irregular solution of Eq. 2.11, (f_i, g_i) as,

$$\psi_{i\beta}(r) = f_i(r)I_{i\beta} - g_i(r)J_{i\beta}$$

This equation can be reformulated into a standard set of linearly independent solutions as [1, 28],

$$M_{ij}(r) = [\underline{\psi}(r)\underline{I}^{-1}]_{ij} = f_i(r)\delta_{ij} - g_i(r)K_{ij} \quad K_{ij} = \sum_{\alpha} U_{i\alpha} \tan(\pi\mu_{\alpha}) U_{\alpha j}^{\dagger} \quad (2.23)$$

Matrices \underline{I} and \underline{J} are determined by the R -matrix which includes the boundary conditions at $r = R_0$, $\underline{R} = \underline{\psi}(R_0) [\underline{\psi}'(R_0)]^{-1} = \underline{M}(R_0) [\underline{M}'(R_0)]^{-1}$. The reaction matrix \underline{K} captures all the information about short-range physics and channel coupling, it corresponds to $\tan(\pi\mu_l)$ in the single-channel QDT. To find out how the \underline{K} matrix relates to the open channels scattering phase shift $\pi\tau_i$, we separate \underline{M} in into open ($\varepsilon_o > 0$) and closed ($\varepsilon_c < 0$) components as:

$$\begin{pmatrix} \underline{M}_{oo} & \underline{M}_{oc} \\ \underline{M}_{co} & \underline{M}_{cc} \end{pmatrix} = \underline{f}(r) - \underline{g}(r) \begin{pmatrix} \underline{K}_{oo} & \underline{K}_{oc} \\ \underline{K}_{co} & \underline{K}_{cc} \end{pmatrix} \quad (2.24)$$

As discussed in Eq. 2.17, the physical boundary conditions for the closed channels are proportional to $\underline{f}(r) + \underline{g}(r) \tan \underline{\beta}$. We can therefore eliminate all the closed channels and obtain the physical solution matrix by applying the $N \times N_o$ transformation matrix $\underline{B} = (\underline{B}_o, \underline{B}_c)^T$,

$$\underline{M}^{phys}(r) = \underline{M}(r)\underline{B} = \begin{pmatrix} [\underline{f}_o(r) - \underline{g}_o(r)\tilde{\underline{K}}]B_o \\ [\underline{f}_c(r) + \tan \underline{\beta}_c \underline{g}_c(r)]B_c \end{pmatrix} \quad (2.25)$$

The \underline{B} and $\tilde{\underline{K}}$ are,

$$\begin{aligned} \underline{B}_o &= \underline{1}_{oo}, & \underline{B}_c &= -(\underline{K}_{cc} + \tan \underline{\beta})^{-1} \underline{K}_{co} \\ \tilde{\underline{K}} &= \underline{K}_{oo} - \underline{K}_{oc}(\underline{K}_{cc} + \tan \underline{\beta})^{-1} \underline{K}_{co} \end{aligned} \quad (2.26)$$

The eigenvalues of $\tilde{\underline{K}}$ are $\tan(\pi\tau_{\rho})$ ($\rho = 1, \dots, N_o$), which are the scattering eigenphase shifts coming from the reaction zone. When the energy increases across a single isolated resonance,

the $\sum_\rho \tau_\rho$ increases by 1. Instead of using the real basis ($\underline{f}, \underline{g}$) to represent $\underline{M}^{phys}(r)$, one can use the incoming and outgoing waves ($\underline{f}^+, \underline{f}^-$) as radial basis functions:

$$\begin{aligned} f_i^+(r) &= \frac{1}{\sqrt{2}}[if_i(r) - g_i(r)] \rightarrow \frac{1}{\sqrt{\pi k_i}} r^{i/k_i} e^{i(k_i r + \eta_i)} \text{ when } \varepsilon \geq 0 \\ f_i^-(r) &= \frac{-1}{\sqrt{2}}[if_i(r) + g_i(r)] \rightarrow \frac{1}{\sqrt{\pi k_i}} r^{-i/k_i} e^{-i(k_i r + \eta_i)} \text{ when } \varepsilon \geq 0 \end{aligned} \quad (2.27)$$

The scattering matrix \underline{S} is introduced as:

$$M_{ij}(r) = \frac{1}{i\sqrt{2}} f_i^+(r) \delta_{ij} - \frac{1}{i\sqrt{2}} f_i^-(r) S_{ij}^\dagger \quad \underline{S} = (\underline{1} + i\underline{K})(\underline{1} - i\underline{K})^{-1} \quad (2.28)$$

The physical wave functions in open channels can be written in terms of $e^{\pm ikr}$ as,

$$\begin{aligned} \underline{M}_o^{phys}(r) &= \underline{f}_o(r) - \underline{g}_o(r) \tilde{K} \xrightarrow{r \rightarrow \infty} \frac{-i}{\sqrt{2\pi k}} (e^{-ikr} - e^{ikr} \underline{S}^{\dagger phys}) \\ \underline{S}^{phys} &= e^{i\eta} (\underline{1} + i\tilde{K})(\underline{1} - i\tilde{K})^{-1} e^{i\eta} = e^{i\eta} [\underline{S}_{oo} - \underline{S}_{oc}(\underline{S}_{cc} - e^{-2i\beta})^{-1} \underline{S}_{co}] e^{i\eta} \end{aligned} \quad (2.29)$$

When the number of open channels $N_o = 1$, $S^{phys} = e^{2i\delta_l(k)}$, $\delta_l(k) = \eta_l + \pi\tau_l$, with $\pi\tau_l$ being the phase-shift resulting from the short-range potential inside the reaction zone, and η_l resulting from the long-range Coulomb phase-shift.

2.3 A full correlated-electron calculation

2.3.1 Streamlined R -matrix method

In this section we consider the multi-dimensional configuration space of the wave function $\Psi_\beta(\vec{r}_1, \vec{r}_2)$ inside the reaction zone $r_2 \leq R_0$. The idea is to use a large number of discretized basis functions to represent a solution, $\Psi_\beta(\vec{r}_1, \vec{r}_2) = \sum_k y_k(\vec{r}_1, \vec{r}_2) C_{k\beta}$, and based on that one can treat the time-independent Schrodinger equation with complicated potential and correlations. The most convenient choice of $y_k(\vec{r}_1, \vec{r}_2)$ is the anti-symmetric product of single electron wavefunctions $y_k^{(i)}(\vec{r}_i) = Y_{lm}(\Omega_i) u_k(r_i)/r_i$, which are the solutions of the ion-core Hamiltonian with potential V_{core} [29]. The full Hamiltonian for the atoms being considered

is given in Eq.2.30. Truncation is made on the basis sets by setting constraints on the maximum number of the nodes in $u_k(r_i)$, as well as the maximum l for $Y_{lm}(\Omega_i)$.

$$H_0(\vec{r}_1, \vec{r}_2) = \sum_{i=1,2} \left(-\frac{\nabla_{\vec{r}_i}^2}{2} + V_{core}(r_i) \right) + \frac{1}{|\vec{r}_1 - \vec{r}_2|} = -\frac{\nabla^2}{2} + U$$

$$V_{core}(r) = \begin{cases} -\frac{2}{r} & \text{for } He^{++} \\ -\frac{1}{r} \left[2 + (Z-2)e^{-\alpha_1^l r} + \alpha_2^l r e^{-\alpha_3^l r} \right] - \frac{\alpha_{cp}}{2r^4} \left[1 - e^{-(r/r_c)^6} \right] & \text{for } Ba^{++} \end{cases} \quad (2.30)$$

The goal of the streamlined R -matrix method is to obtain boundary conditions of the wave functions at $r_2 = R_0$ and $r_1 = R_0$ (for simplicity, we only discuss the $r_2 = R_0$ boundary), which are necessary for the MQDT treatment,

$$\Psi_\beta(\vec{r}_1, \vec{r}_2) = r_2^{-1} \sum_{i=1}^N \Phi_i(\vec{r}_1, \Omega_2) \psi_{i\beta}(r_2) \quad \partial[r_2 \Psi_\beta(\vec{r}_1, \vec{r}_2)] / \partial r_2 = \sum_{i=1}^N \Phi_i(\vec{r}_1, \Omega_2) \psi'_{i\beta}(r_2) \quad (2.31)$$

The way to approach this is to consider the eigenvalues of $\underline{R} = \underline{\psi}(R_0)(\underline{\psi}'(R_0))^{-1}$, which are $b_\beta = -\frac{1}{\Psi_\beta} \frac{\partial \Psi_\beta}{\partial n}$. In this variational method, the b_β are obtained from the stationary principle by varying over Ψ_β with fixed total energy E . We start with the Schrodinger equation $(E - H_0)\Psi_\beta = 0$ (The index β is neglected in the following discussion because we consider only one b_β value at a time),

$$E \int_V \Psi^* \Psi dv = \int_V \left(-\frac{1}{2} \Psi^* \nabla^2 \Psi + \Psi^* U \Psi \right) dv \quad (2.32)$$

According to Green's theorem,

$$\int_V (\Psi^* \nabla^2 \Psi + \nabla \Psi^* \cdot \nabla \Psi) dv = \oint_\Sigma \Psi^* \frac{\partial \Psi}{\partial n} da = -b \oint_\Sigma \Psi^* \Psi da \quad (2.33)$$

The equation above can be rearranged into a constraint on the boundary condition b ,

$$b \oint_\Sigma \Psi^* \Psi da = 2 \left[\int_V \Psi^* E \Psi dv - \int_V \left(\frac{1}{2} \nabla \Psi^* \cdot \nabla \Psi + \Psi^* U \Psi \right) dv \right] \quad (2.34)$$

Our goal is to find the optimal real coefficients \vec{C} in $\Psi = \sum_k y_k C_k$. The operators in Eq.2.34 can be recast into the matrix elements of $\{y_k\}$, that $\Lambda_{kj} = \oint_{\Sigma} y_k y_j da$, $\Gamma_{kj} = 2 \int_V y_k E y_j dv - \int_V (\frac{1}{2} \nabla y_k \cdot \nabla y_j + y_k U y_j) dv$,

$$b \sum_{kj} C_k \Lambda_{kj} C_j = \sum_{kj} C_k \Gamma_{kj} C_j \xrightarrow{\partial b[\vec{C}]/\partial C_k=0} \underline{\Gamma} \vec{C} = b \underline{\Lambda} \vec{C} \quad (2.35)$$

The optimal boundary property b should satisfy the stationary principle $\partial b[\vec{C}]/\partial C_k = 0$. By taking derivative of each \vec{C} component, one can obtain a generalized eigenvalue equation of optimal \vec{C} , which corresponds to the desirable solution $\Psi(\vec{r}_1, \vec{r}_2)$.

To vary $\{\Psi_\beta\}$ over all possible boundary conditions, not only the basis functions satisfying $y_k = 0$ at the boundary are concerned, we need to choose at least one radial function $u_k(r_2) \neq 0$ at $R_2 = R_0$. By separating the basis functions $\{y_k\}$ into closed ($\{y_c\}$) and open type ($\{y_o\}$) depending whether they are zero or not at $r_2 = R_0$, Eq.2.35 can be rearranged into,

$$\begin{pmatrix} \underline{\Gamma}^{cc} & \underline{\Gamma}^{co} \\ \underline{\Gamma}^{oc} & \underline{\Gamma}^{oo} \end{pmatrix} \begin{pmatrix} \vec{C}^c \\ \vec{C}^o \end{pmatrix} = b \begin{pmatrix} \underline{0} & \underline{0} \\ \underline{0} & \underline{\Lambda}^{oo} \end{pmatrix} \begin{pmatrix} \vec{C}^c \\ \vec{C}^o \end{pmatrix} \quad (2.36)$$

The equation above can be reduced into one much smaller in dimension, with only the open type of basis:

$$\underline{\Omega} \vec{C}^o = b \underline{\Lambda}^{oo} \vec{C}^o, \quad \underline{\Omega} = \underline{\Gamma}^{oo} - \underline{\Gamma}^{oc} (\underline{\Gamma}^{cc})^{-1} \underline{\Gamma}^{co} \quad (2.37)$$

The closed-type of coefficients are, $\vec{C}^c = -(\underline{\Gamma}^{cc})^{-1} \underline{\Gamma}^{co} \vec{C}^o$.

If we assumes only one $u_k(r_2) \neq 0$ for every combination of $Y_{lm}(\Omega_{1(2)})$ and $u_k(r_1)$ in choosing the basis sets, the dimension of $\underline{\Omega}$ equals to N , the number of channel functions $\Phi(\vec{r}_1, \Omega_2)$. In addition, the number of different eigenvalues b in Eq.2.37 is always N , no matter how many open-type basis functions are utilized (if the dimension of $\underline{\Omega}$ is larger than N , Eq.2.37 can be further reduced into an eigenvalue equation of dimension N).

Eventually, the eigenvalues b_β (or the matrix \underline{R}) lead to the reaction matrix \underline{K} as following:

$$\underline{K} = \left[\underline{f}(R_0) - \underline{f}'(R_0) \underline{R} \right] \left[\underline{g}(R_0) - \underline{g}'(R_0) \underline{R} \right]^{-1} \quad (2.38)$$

Applications to helium and barium

In the following chapters, the streamlined R -matrix method is applied to evaluate the wave functions for atomic helium and barium. Here are the parameters we choose for those calculations:

To evaluate the wave functions for helium, the single-electron radial functions are constructed by B-splines. For final state energy up to $N = 2$ threshold, the R -matrix box $R_0 = 15 \text{ a.u.}$, the maximum number of nodes in radial functions is 18 (plus 2 open-typed radial basis), and the allowed single electron angular momenta are $l = 0 - 4$. The number of closed configurations are 855, 1296, and 1656 for the $L = 0$, $L = 1$, and $L = 2$ final states, with the number of channel functions being 3, 4, and 4, respectively. For final state energy up to the $N = 3$ threshold, $R_0 = 34 \text{ a.u.}$, the maximum number of radial nodes equals to 38 (plus 2 open-typed radial basis), and the allowed single electron angular momenta are $l = 0 - 9$. The number of closed configurations for $L = 0$, $L = 1$, and $L = 2$ final states are, 3990, 6787 and 9286, respectively; with their number of channels being 6, 9, and 10.

For the barium R -matrix calculation, the final energy is above $6s^{1/2}$ and $5d^{3/2}$ but below $5d^{5/2}$ threshold. The $R_0 = 60 \text{ a.u.}$, the maximum number of radial nodes is 60 (plus 2 open-typed radial basis), and the allowed single electron angular momenta are $l = 0 - 4$ (with $j = |l \pm 1/2|$). Besides, the lowest number of nodes is restricted to be no greater than 9, while the highest number of nodes is no greater than 21, or 25 for the intermediate and final states. These conditions result in 522, 1270, and 1750 closed configurations for intermediate states with $J=0$, 1, and 2, respectively; and 1584, 2160, and 2304 closed configurations for final states with $J=1$, 2, and 3, respectively. The number of channel functions for even parity $J=0$, 1, and 2 are 3, 8, and 11; and for odd parity for $J=1$, 2, and 3 are 8, 10, and 9.

3. APPLICATION TO MULTI-PHOTON IONIZATION

Single-photon absorption has been used since the 1960s to probe doubly-excited states with extreme electron correlation in the helium atom and many other alkaline earth atoms [8, 9, 10]. In recent decades, increasing interest has derived from studying electron correlation using other types of excitation, such as non-sequential multiphoton double ionization which has received extensive attention [30, 31, 32]. Additionally, the use of multiple fields to dress the helium and alkaline earth atom Hamiltonians with infrared (IR) light has demonstrated remarkable control possibilities, both for autoionization line shapes and temporal pulse phase control. [33, 34, 35, 36, 37, 38, 39, 40, 41]

In this chapter, we will demonstrate the multiphoton ionization spectra for helium and barium, which will be the foundation of the discussions in the following chapters. Multiphoton ionization can in principle proceed either via sequential steps through one or more bound intermediate stationary states en route to ionization, or non-sequentially with either no intermediate stationary states or else through a continuous intermediate state in the ionization continuum. Our calculations are based on some early studies of doubly excited alkaline earth atoms and the polar asymmetrical two-electron systems [42, 43, 44, 45, 46, 47, 48, 49]. Some of the theoretical results presented in this chapter are currently being explored in free electron laser (FEL) experiments.

3.1 Light-atom interaction and Wigner algebra

To realize multi-photon ionization, the laser intensity needs to be strong enough for the electrons to absorb a bunch of photons simultaneously. However, the intensity of that multi-photon regime is not as strong as in the tunneling region (below about 10^{14} W/cm^2 at optical frequencies, so the tunneling time of the fragmented electron is much longer than the optical period). The light-atom interaction can be analyzed via the time-dependent

perturbation method in the multi-photon region, and the Hamiltonian for a monochromatic laser interacting with an atom with two active electrons is given below:

$$\begin{aligned}
H(\vec{r}_1, \vec{r}_2, t) &= H_0(\vec{r}_1, \vec{r}_2) + V(\vec{r}_1, t) + V(\vec{r}_2, t) \\
V(\vec{r}, t) &= \frac{1}{2} \mathcal{E}_0 \hat{\epsilon} \cdot \vec{r} e^{-i\omega t} \quad (i = 1, 2)
\end{aligned} \tag{3.1}$$

$H_0(\vec{r}_1, \vec{r}_2)$ is the non-relativistic Hamiltonian for a bare alkaline-earth atom, which is given in Eq.2.30. $V(\vec{r}_j, t)$ is the interaction between electron j and the laser field, whose amplitude is \mathcal{E}_0 , polarizes along $\hat{\epsilon}$ with angular frequency ω . The electric dipole approximation is applied ($e^{-i\vec{k}\cdot\vec{r}} \approx 1$), assuming the laser wavelength is much larger than the size of the atom. Since only absorption processes are considered, the $e^{+i\omega t}$ term is omitted in Eq.(3.1) under the usual rotating wave approximation.

The rate and generalized cross section (whose unit is $l^{2q}t^{q-1}$, sometimes abbreviated in the text by ‘‘cross section’’) for q -photon ionization are,

$$\begin{aligned}
R_{tot} &= 2\pi \left(\frac{\mathcal{E}_0}{2}\right)^{2q} \sum_f |T_{f,i}^{(q)}|^2 \delta(E_f - E_i - q\omega) \\
\sigma_{tot} &= 2\pi(2\pi\alpha\omega)^q \sum_f |T_{f,i}^{(q)}|^2
\end{aligned} \tag{3.2}$$

α is the fine structure constant, $T_{f,i}^{(q)}$ is the q -th order photon transition amplitude from the initial to the final states, whose formula is given based on a q th- order perturbation treatment:

$$T_{f,i}^{(q)} = \sum_{\varepsilon_1 \dots \varepsilon_{q-1}} \frac{\langle f | D | \varepsilon_{q-1} \rangle \dots \langle \varepsilon_2 | D | \varepsilon_1 \rangle \langle \varepsilon_1 | D | i \rangle}{[E_{\varepsilon_{q-1}} - E_i - (q-1)\omega] \dots (E_{\varepsilon_1} - E_i - \omega)} \tag{3.3}$$

$D = \hat{\epsilon} \cdot (\vec{r}_1 + \vec{r}_2)$ is the electric dipole operator in the length gauge. The intermediate energies E_{ε_j} include all the eigenvalues of H_0 that obey the usual good symmetry and angular momentum selection rules. All the continuous states are normalized per unit energy. i and f denote all the quantum numbers for the initial and final states: In $L - S$ coupling scheme, those include the principal quantum numbers (n_1, n_2) , angular momenta for orbital $[(l_1 l_2) LM]$ and spin $S = 0$ (in the $L - S$ coupling scheme, the electron pair always stays in a spin-singlet state, so we are not going to discuss it), and parity $\pi = (-1)^{l_1+l_2}$. For $J - J$

coupling scheme, the difference is in the angular momenta, whereas the angular momenta are $\{[(s_1, l_1)j_1, (s_2, l_2)j_2]JM_J\}$. The subscript 1(2) denotes the quantum numbers for the core (emission) electron. Whether an atom stays in $L - S$ or $J - J$ coupling scheme is determined by the relative strength of spin-orbital interaction and spin-spinor orbital-orbital interaction. The former one is proportional to Z^4 , therefore for heavy atoms with large Z , the spin-orbit interaction wins that L and S are no longer good quantum numbers. Examples for $L - S$ and $J - J$ coupling are atomic helium and barium, which will be discussed separately.

The angular distribution of the photoelectron, i.e., the differential generalized q -photon ionization cross-section, is given by:

$$\frac{d\sigma}{d\Omega} = 2\pi(2\pi\alpha\omega)^q \sum_{\lambda_{in}} \left| \sum_{\lambda_{co}} Y_{l_2 m_2}(\hat{k}) C_f T_{f,i}^{(q)} \right|^2 \quad (3.4)$$

The incoherent sum index λ_{in} , coherent sum index λ_{co} and Clebsch-Gordan coefficients C_f for $L - S$ and $J - J$ coupling scheme are,

$$\begin{cases} \lambda_{in} = \{n_1, l_1, \text{all the } M\} & \lambda_{co} = \{l_2, L_f\} & L - S \text{ coupling} \\ \lambda_{in} = \{n_1, j_1, J_{cs}, \text{all the } M\} & \lambda_{co} = \{j_2, J_f\} & J - J \text{ coupling} \end{cases} \quad (3.5)$$

and

$$C_f = \begin{cases} \langle l_1 m_1, l_2 m_2 | L_f, M_f \rangle & L - S \text{ coupling} \\ \langle J_{cs} M_{J_{cs}}, l_2 m_2 | J_f, M_{J_f} \rangle \langle [(j_1, s_2) J_{cs}, l_2] J_f | [(j_1, (l_2, s_2) j_2] J_f \rangle & J - J \text{ coupling} \end{cases} \quad (3.6)$$

For $J - J$ coupling, $\vec{J}_{cs} = \vec{j}_1 + \vec{s}_2$, $\vec{J}_f = \vec{J}_{cs} + \vec{l}_2$. In above equations, when $M_f(M_{J_f}) = 0$, the system has azimuthal symmetry, Eq. 3.4 can therefore be arranged into a sum of Legendre polynomials $P_k(\cos\theta)$ (θ is the polar angle between the ejected electron direction and the polarization axis) with real coefficients β_k as ($\beta_0 \equiv 1$ for normalization),

$$\frac{d\sigma}{d\Omega} = \frac{\sigma_{tot}}{4\pi} \sum_k \beta_k(\omega) P_k(\cos\theta) \quad (3.7)$$

The maximum order of k in Eq.3.7 should equal twice the step of ionization $2q$ if the initial state is the ground state or in fact any initial state that has a random distribution of magnetic sublevels. With a fixed number q , all the final states are in the same parity according to the selection rule, therefore odd orders of $\beta_k = 0$. The explicit expressions for β_k in $L - S$ coupling are given by,

$$\beta_k^{(n_1)} = \frac{1}{\sigma^{(n_1)}} \sum_{l_1} \sum_{l_2, l'_2, L_f, L'_f} (-1)^{l_1+l_2+l'_2+L_f+L'_f} T_{f,i}^{(q)} T_{i,f'}^{(q)*} [l_2] [l'_2] [L_f] [L'_f] [k]^2 \begin{pmatrix} l_2 & l'_2 & k \\ 0 & 0 & 0 \end{pmatrix} \begin{pmatrix} k & L_f & L'_f \\ 0 & 0 & 0 \end{pmatrix} \left\{ \begin{matrix} k & L_f & L'_f \\ l_1 & l'_2 & l_2 \end{matrix} \right\} \quad (3.8)$$

Similarly, for $J - J$ coupling, they are given by,

$$\beta_k^{(n_1)} = \frac{1}{\sigma^{(n_1)}} \sum_{j_1, J_{cs}} \sum_{l_2, l'_2, j_2, j'_2, L_f, L'_f} (-1)^{j_1+l_2+l'_2+J_f+J'_f} T_{f,i}^{(q)} T_{i,f'}^{(q)*} [l_2] [l'_2] [j_2] [j'_2] [J_f] [J'_f] [k]^2 [J_{cs}]^2 \begin{pmatrix} l_2 & l'_2 & k \\ 0 & 0 & 0 \end{pmatrix} \begin{pmatrix} k & J_f & J'_f \\ 0 & 0 & 0 \end{pmatrix} \left\{ \begin{matrix} k & J_f & J'_f \\ J_{cs} & l_2 & l_2 \end{matrix} \right\} \left\{ \begin{matrix} j_1 & s_1 & J_{cs} \\ l_2 & J_f & j_2 \end{matrix} \right\} \left\{ \begin{matrix} j_1 & s_1 & J_{cs} \\ l'_2 & J'_f & j'_2 \end{matrix} \right\} \quad (3.9)$$

with $\beta_k = \sum_{n_1} \frac{\sigma^{(n_1)}}{\sigma_{tot}} \beta_k^{(n_1)}$.

In above equations, superscripts on $\beta_k^{(n_1)}$ and $\sigma^{(n_1)}$ are introduced to separately identify groups of photoelectrons with different energies that are generated at the same total final state energy. They correspond to angular distribution asymmetry parameters and partial cross section for electrons with a certain escape kinetic energy in all channels having a given ionic principal quantum number $N = n_1$. $\beta_0^{(n_1)} \equiv 1$. The bracket $()$ represents the Wigner-3J symbol, while $\{\}$ represents the Wigner-6J symbol, $[L] \equiv \sqrt{2L+1}$. The derivation details largely follow the discussion in Ref. [41, 46, 50].

The Wigner algebra can also be used to evaluate the dipole matrix elements $\langle LM|D|L'M' \rangle$ in Eq.3.3 (for $J - J$ coupling replace (L, M) by (J, M_J)), by writing them into “reduced

matrix elements” which are independent of the polarization of the light, according to the Wigner-Eckart theorem:

$$\langle LM|D|L'M'\rangle = \langle LM||D||L'M'\rangle (-1)^{L-M} \sum_k (-1)^k \epsilon_{-k}^{(1)} \begin{pmatrix} L & 1 & L' \\ -M & k & M' \end{pmatrix} \quad (3.10)$$

Where $\epsilon_k^{(1)}$ are the spherical components of the rank-1 polarization tensor, $\epsilon_0^{(1)} = \hat{z}$ and $\epsilon_{\pm 1}^{(1)} = \mp 1/\sqrt{2}(\hat{x} \pm i\hat{y})$. One can further decompose the reduced dipole matrix element and extract all the angular dependence[50]. The decomposition for $L - S$ coupling gives,

$$\langle \Psi || D || \Psi' \rangle = \langle \psi_1 | r | \psi'_1 \rangle \langle \psi_2 | \psi'_2 \rangle (-1)^{1+l_2+L'} [l_1][l'_1][L][L'] \delta_{l_2 l'_2} \begin{pmatrix} l_1 & 1 & l'_1 \\ 0 & 0 & 0 \end{pmatrix} \begin{Bmatrix} l_1 & L & l_2 \\ L' & l'_1 & 1 \end{Bmatrix} \quad (3.11)$$

and the corresponding expression for $J - J$ coupling is:

$$\begin{aligned} \langle \Psi || D || \Psi' \rangle &= \langle \psi_1 | r | \psi'_1 \rangle \langle \psi_2 | \psi'_2 \rangle (-1)^{J'+j_2+l_1+l'_1+\frac{1}{2}} [l_1][l'_1][j_1][j'_1][J][J'] \delta_{l_2 l'_2} \\ &\times \begin{pmatrix} l_1 & 1 & l'_1 \\ 0 & 0 & 0 \end{pmatrix} \begin{Bmatrix} j_1 & J & j_2 \\ J' & j'_1 & 1 \end{Bmatrix} \begin{Bmatrix} l_1 & j_1 & \frac{1}{2} \\ j'_1 & l'_1 & 1 \end{Bmatrix} \end{aligned} \quad (3.12)$$

The equations above will of course respect the angular momentum selection rule, namely that each step of ionization will change the angular momentum by $|\Delta L| = 1, 0$ (or $|\Delta J| = 1, 0$) with $0 \not\rightarrow 0$, and flip the parity π from even (+1) to odd (-1). The schematic diagram for $L - S$ and $J - J$ coupled ionization steps can be found in Fig.3.2 and 3.9.

3.2 Multi-photon ionization of helium

Based on the formulas introduced in the last section, the present section will quantitatively treat the process of double excitation of helium from the ground state ($1s^2$, singlet) to the lower-lying autoionizing states, where at least one of the electrons is in either the $N = 2$ or $N = 3$ shell (Fig.3.1). This process is very much related to the two-photon double ionization[30, 31, 32], but is experimentally simpler and theoretically less demanding. The photoelectron angular distribution is computed to elucidate the strengths of interfering

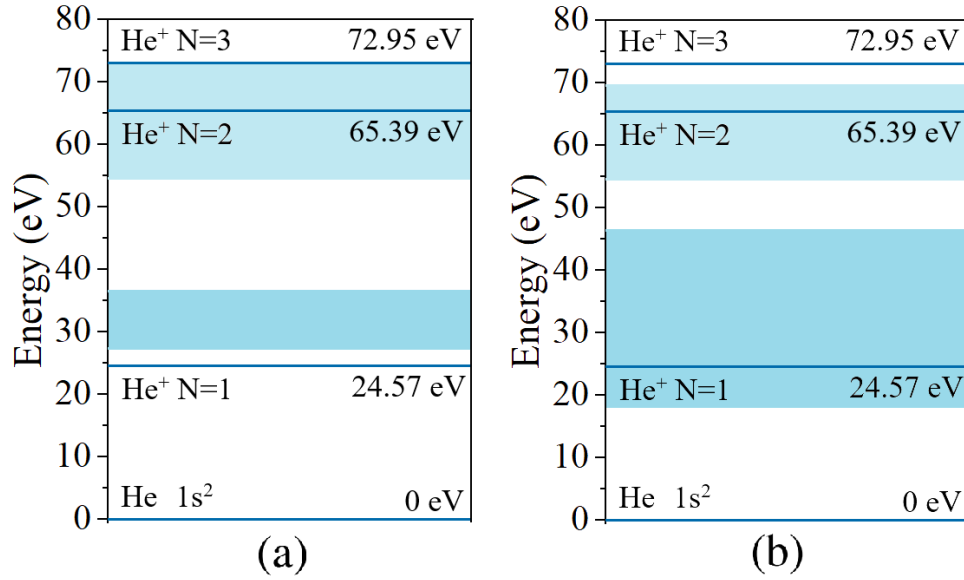


Figure 3.1. Energy diagram of relevant levels in the two-photon ionization of helium. The shaded regions show the energy ranges for the final and intermediate states. (a) Two identical photons $\omega_1 = \omega_2$. The intermediate energies are above the $N = 1$ threshold, and there are no intermediate-state resonances involved, only an open ionization continuum. (b) Trefoil field $\omega_1 = 2\omega_2$. Some of the intermediate states are above threshold, and two intermediate resonances $1s2p$ and $1s3p$ are involved.

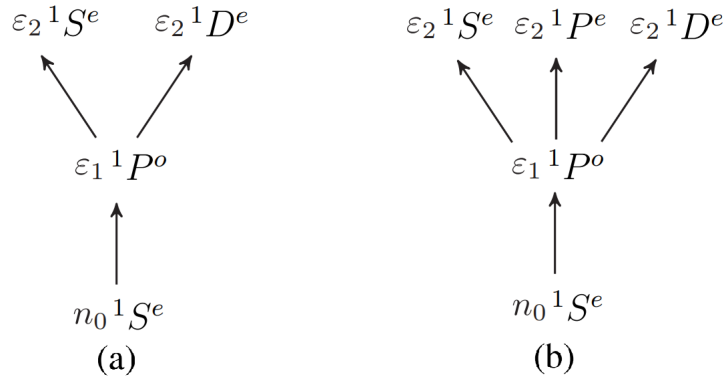


Figure 3.2. Schematic diagram of two-photon ionization channels allowed by electric-dipole selection rules for (a) parallel linearly polarized and (b) two opposite circularly polarized fields. $^{2S+1}L^\pi$ are labeled for each step of ionization. The $1P^e$ state is a parity-unfavored state whose lowest channel becomes open at the $N = 2$ hydrogenic threshold.

pathways associated with direct ionization and with correlated autoionization decay. Based on a combination of the R-matrix and generalized quantum defect methods, we achieve good consistency with some previous calculations where our results can be compared with them, and extend into higher energy ranges not routinely treated.

Especially, for two-photon ionization, two different laser fields will be treated in this section, which are: (a) The linearly polarized field, with both photons having frequency ω and polarization direction $\epsilon_0^{(1)}$, and (b) Two oppositely circularly polarized ($\hat{\epsilon}_{1,2} = \epsilon_{\pm 1}^{(1)}$) laser sources with frequencies $\omega_1 = 2\omega_2$, which is the so-called “trefoil field”. The possible values of the quantum numbers $^{2S+1}L^\pi$ allowed by the selection rules have been given in Fig. 3.2, (a) and (b). Note that with circularly polarized photons, a “parity unfavored” $^1P^e$ symmetry, for which $\pi(-1)^L = -1$, can be obtained. The energy diagrams for (a) and (b) are shown in Fig. 3.1 in eV. In atomic units, the ground state lies at $E_g = -2.903$ *a.u.* relative to the double ionization threshold, and the single ionization thresholds shown in the figure are at $E_{N=n_1} = -2/N^2$ *a.u.*. The frequency range considered for field (a) is $\omega = 1.0 - 1.35$ *a.u.*, making final states that converge to the $N = 2$ and $N = 3$ thresholds. The intermediate state lies in the continuum, making this an above-threshold ionization (ATI) process with no discrete intermediate-state resonances. For the field (b), the frequency of ω_2 is, $\omega_2 = 0.67 - 0.85$ *a.u.*, reaching final states across the $N = 2$ threshold. The intermediate states can be both bound and continuous. The $1s2p$ and $1s3p$ states are included in the shaded intermediate region, which can cause intermediate resonances. For three-photon ionization, we consider only the simplest cases, the linearly polarized field with three photons, for $\omega = 0.33 - 0.48$ and $0.80 - 0.89$ *a.u.*, which have already been calculated by previous groups [51, 52], and here, our results only confirm the validity of our calculations.

The major issue in calculating the multi-photon ionization is the evaluation of $T_{f,i}$ in Eq.6.2. Especially, for the ATI processes of helium to lower-lying autoionizing states, we will meet the following obstacles: The first is the treatment of the summation/integration over intermediate states and the continuum-continuum transition in ATI processes, which will be discussed in Subsec. 3.2.1. The other is the MQDT parameters in the Coulomb field with permanent dipole interaction from the ionic core, which will be discussed in Subsec. 3.2.2.

After solving those problems, the calculated spectrum for the laser fields discussed above will be given in Subsec. 3.2.3 and 3.2.4.

3.2.1 Above-threshold ionization

When the intermediate energies are larger than the lowest threshold $E_\varepsilon > E_{N=1}$, Eq.3.3 can be written as a mixture of sum and integration over the discrete and continuous intermediate states $|\varepsilon\rangle$ as:

$$T_{f,i} = \sum_{\varepsilon} dE_\varepsilon \frac{\langle f|D|\varepsilon\rangle\langle\varepsilon|D|i\rangle}{E_i + \omega - E_\varepsilon} \quad (3.13)$$

The difficulty in evaluating Eq.3.13 is two-fold: firstly, one needs to calculate $\langle f|D|\varepsilon\rangle$, which is an integral with two divergent functions, whose convergence is questionable. The other is the infinite sum and integration over the intermediate states. These difficulties can be solved, not by choosing wave functions $\{|\varepsilon\rangle\}$ and evaluating Eq.3.13 term by term, but by treating $\sum_{\varepsilon} \frac{|\varepsilon\rangle\langle\varepsilon|}{E_i + \omega - E_\varepsilon}$ as a Green's function which subjects to the out-going wave boundary conditions, which can be solved by the inhomogeneous R-matrix method [53, 54]. The continuum-continuum transition $\langle f|D|\varepsilon\rangle$ outside the reaction zone can either be solved asymptotically by complex coordinate rotation [55] or by an asymptotic expansion method[54]. The details of these methods can be found in Ref. [54].

Inhomogeneous R-matrix method

To solve Eq.3.13, one can replace \sum by an integral over the inhomogeneity multiplied by the Green's function, $|\Lambda_p\rangle = \int d\varepsilon |\varepsilon\rangle \frac{\langle\varepsilon|D|0\rangle}{E_i + \omega - E_\varepsilon}$. It can be obtained by solving the equation $(E - H_0)\Psi_{\Lambda_p} = D\Psi_0$, in a similar way as one solves the Schrodinger equation $(E - H_0)\Psi = 0$ by the streamlined R-matrix method (Sec.2.3).

The physical boundary condition for Ψ_{Λ_p} can be described by the multi-channel picture, $\Psi_{\Lambda_p} = \sum_i \Phi_i(\vec{r}_1, \Omega_2)\psi_{\Lambda_p,i}(r_2)$, that

$$\psi_{\Lambda_p,i}(r) = \begin{cases} f_i + ig_i \xrightarrow{r \rightarrow \infty} e^{ik_i r} & \text{open channel} \\ f_i + \tan \beta_i g_i \xrightarrow{r \rightarrow \infty} e^{-r/\nu_i} & \text{closed channel} \end{cases} \quad (3.14)$$

This boundary condition requires the time-dependent intermediate wave function to be a purely out-going wave packet. Note that this particular inhomogeneous solution Ψ_{Λ_p} can be generated by adding homogeneous solutions to an arbitrary inhomogeneous solution $\Psi_{\Lambda'_p}$, to impose the desired boundary condition:

$$\Psi_{\Lambda_p}(\vec{r}_1, \vec{r}_2) = \Psi_{\Lambda'_p}(\vec{r}_1, \vec{r}_2) + \sum_j A_j \times \Psi_j(\vec{r}_1, \vec{r}_2) \quad (3.15)$$

An arbitrary boundary condition can be chosen for $\Psi_{\Lambda'_p}$: $b_\lambda = -\frac{1}{\Psi_{\Lambda'_p}} \frac{\partial \Psi_{\Lambda'_p}}{\partial n}$, by adding homogeneous solutions $\Psi_j \xrightarrow{r_2 \rightarrow \infty} \sum_i \Phi_i(\vec{r}_1, \Omega_2) M_{ij}(r_2)$ which are non-vanishing at infinity, we can obtain Ψ_{Λ_p} having the desirable boundary conditions.

$\Psi_{\Lambda'_p}$ can be solved by using the R -matrix basis in Sec.2.3, $\Psi_{\Lambda'_p} = \vec{C}_\lambda \cdot \vec{y}$, and by applying the stationary principal $\partial b_\lambda[\vec{C}_\lambda]/\partial C_\lambda^k = 0$ to it (one must choose $b_\lambda \neq b_\beta$), the inhomogeneous equation turns into the following equation:

$$(\underline{\Omega} - b_\lambda \underline{\Lambda}^{oo}) \vec{C}_\lambda^o = 2[\vec{Z}^o - \underline{\Gamma}^{oc}(\underline{\Gamma}^{cc})^{-1} \vec{Z}^c] \quad \underline{\Omega} = \underline{\Gamma}^{oo} - \underline{\Gamma}^{oc}(\underline{\Gamma}^{cc})^{-1} \underline{\Gamma}^{co} \quad (3.16)$$

The coefficients for the closed-type basis are, $\vec{C}_\lambda^c = -(\underline{\Gamma}^{cc})^{-1}(\underline{\Gamma}^{co} \vec{C}_\lambda^o - 2\vec{Z}^c)$. The inhomogeneity is $\vec{Z} = \int_V \vec{y} D\Psi_0 dv$. Whenever it vanishes, those formulas revert to Eq. 2.37.

Once $\Psi_{\Lambda'_p}$ has been solved inside the reaction zone, it can be written into $\Psi_{\Lambda'_p} = \sum_i \Phi_i(\vec{r}_1, \Omega_2)(f_i(r_2)\lambda_i^{(f)} - g_i(r_2)\lambda_i^{(g)})$ asymptotically. The homogeneous terms $\{A_j\}$ in Eq.3.15 that matches $\Psi_{\Lambda'_p}$ onto Ψ_{Λ_p} can therefore be obtained by:

$$\begin{aligned} \vec{A} = & (\underline{K} + \underline{i})^{-1}(\vec{\lambda}^{(g)} + i\vec{\lambda}^{(f)}) - (\underline{K} + \underline{B})^{-1}(\underline{B} - \underline{i}) \\ & \times \frac{1}{2}[\vec{\lambda}^{(f)} + i\vec{\lambda}^{(g)} - i(\underline{K} - \underline{i})(\underline{K} + \underline{i})^{-1}(\vec{\lambda}^{(g)} + i\vec{\lambda}^{(f)})] \end{aligned} \quad (3.17)$$

where $\underline{B} = \text{diag}[(\tan \beta)_c, (\underline{i})_o]$ and \underline{K} is the reaction matrix in homogeneous solution $\underline{M}(r)$ in Eq.2.23.

Integration of free-free transition

For the radial integral of a free-free transition $I = \int_{R_0}^{\infty} dr \psi_a(r) G(r) \psi_b(r)$ to converge, the scattering states $\psi_a(r)$ and $\psi_b(r)$, which are solutions of $-\psi_i''(r)/2 = (E_i - V_i(r))\psi_i(r)$, need to satisfy: $E_a \neq E_b$ with $|E_a - E_b| = \omega$. When ω is large enough, the radial integral I can be evaluated by the asymptotic expansion method [54], otherwise, it can be evaluated by the complex coordinate rotation[55].

The asymptotic expansion is based on the iteration relationship of the operator $\bar{\omega} = E_a - E_b - V_a + V_b$:

$$\begin{aligned} \bar{\omega} \psi_a \psi_b &= -\frac{1}{2} (W[\psi_a, \psi_b])' \\ \bar{\omega} W[\psi_a, \psi_b] &= \frac{1}{2} (\psi_a \psi_b)''' + 2[(E_a + E_b - V_a - V_b) \psi_a \psi_b]' + (V_a + V_b)' \psi_a \psi_b \end{aligned} \quad (3.18)$$

$W[\psi_a, \psi_b] = \psi_a' \psi_b - \psi_a \psi_b'$ is the Wronskian. By writing $I = -\frac{1}{2} \int_{R_0}^{\infty} dr \frac{G(r)}{\bar{\omega}} (W[\psi_a, \psi_b])'$, one can drop the surface terms that are negligibly small at $r \rightarrow \infty$ (which requires $|l_a(l_a + 1) - l_b(l_b + 1)| \ll 2\omega R_0^2$ and $2\omega^2 R_0^3 \gg 1$). Since we have $R_0 \geq 15 \text{ a.u.}$ and $\omega > 0.67 \text{ a.u.}$, the radial integral I can be evaluated by:

$$\begin{aligned} I &= \frac{R_0}{2\bar{\omega}} W[\psi_a, \psi_b]_{R_0} - \frac{1}{2\bar{\omega}^2} [\psi_a' \psi_b' + \psi_a \psi_b (E_a + E_b - V_a - V_b)]_{R_0} \\ &+ \left(\frac{V_a + V_b}{4\bar{\omega}^3} \right)'_{R_0} W[\psi_a, \psi_b]_{R_0} + O\left(\frac{1}{\bar{\omega}^4}\right) \end{aligned} \quad (3.19)$$

The method of complex coordinate rotation transforms the coordinates into a complex contour $\rho(r)$, that $I = \int_{R_0}^{\infty} d\rho(r) \psi_a(\rho(r)) G(\rho(r)) \psi_b(\rho(r))$:

$$\rho(r) = \begin{cases} r & r < R_0 \\ R_0 + (r - R_0)e^{i\phi} & r \geq R_0 \end{cases} \quad (3.20)$$

Under this rotation, the outgoing wave $f(r) + ig(r) \approx e^{ikr} \rightarrow e^{ik\rho}$ decays exponentially with $kr \sin \phi$, so we can expand ψ_a into (f, g) basis, and evaluate $f_a(\rho)$ component by (assuming $\psi_b(r)$ is a real function),

$$\int_{R_0}^{\infty} d\rho f_a(\rho)G(\rho)\psi_b(\rho) = \text{Re}[e^{i\phi} \int_{R_0}^{\infty} dr [f_a(\rho(r)) + ig_a(\rho(r))]G(\rho(r))\psi_b(\rho(r))] \quad (3.21)$$

Similarly, the $g_a(\rho)$ component is the imaginary part of the same integral. This integral converges for arbitrary small ω given $E_a > E_b$, and similar argument can be drawn for $E_a < E_b$.

3.2.2 Gailitis-Damburg treatment of electric dipole moment

The MQDT treatment (Sec.2.2) approximates the potential experienced by the outer electron by the overall Coulomb interaction with the screened ion, which neglects the electron correlations outside the reaction zone $\frac{1}{|\vec{r}_1 - \vec{r}_2|} \approx \frac{1}{r_2}$. This approximation is accurate for most doubly excited alkaline earth atoms, but not enough for the lower-lying autoionizing states of helium, whose electron correlation is most prominent. To address its electron correlation at long range outside the R-matrix box, the coupling between the outer electron and the permanent electric dipole moment of the degenerate excited He^+ core is also important: $\frac{1}{|\vec{r}_1 - \vec{r}_2|} \approx \frac{1}{r_2} + \frac{\vec{r}_1 \cdot \vec{r}_2}{r_2^2}$. Owing to the degeneracy of the excited hydrogenic thresholds (neglecting fine structure and the Lamb shift), this dipole term can be merged with the outer electron angular momentum term $\frac{\vec{l}_2^2}{2r_2^2}$. We denote the composite of the dipole and the orbital (centripetal) term as the Gailitis-Damburg operator[56], whose matrix elements under the channel functions $\Phi_i(\vec{r}_1, \Omega_2) = \phi_i(r_1)Y_{l_1^i, l_2^i, L}(\Omega_1, \Omega_2)$ can be written as

$$\begin{aligned} A_{ij} &= \langle \phi_i(r_1)Y_{l_1^i, l_2^i, L} | \frac{\vec{l}_2^2}{2r_2^2} + 2r_1 \cos \theta_{12} | \phi_j(r_1)Y_{l_1^j, l_2^j, L} \rangle \\ &= l_2(l_2 + 1)\delta_{l_2^i, l_2^j} \delta_{l_1^i, l_1^j} + 2\langle \phi_i | r_1 | \phi_j \rangle \langle (l_1^i, l_2^i)L | \cos \theta_{12} | (l_1^j, l_2^j)L \rangle. \end{aligned} \quad (3.22)$$

This matrix can be represented in terms of eigenvectors and eigenvalues as $A_{ij} = \sum_{\gamma} X_{i,\gamma} \alpha_{\gamma} X_{\gamma,j}^T$, which allows us to perform a generalized MQDT calculation in the dipole representation with the new channel index γ . The channel correspondence between the independent electron ba-

sis $\{i\} = (n_1, l_1; l_2)$ and the Gailitis-Damburg basis $\{\gamma\}$ is controlled by $X_{i,\gamma}$ [57]. The radial Schrodinger equation for the outer electron in the channel γ is,

$$\left(-\frac{1}{2} \frac{d^2}{dr_2^2} - \frac{1}{r_2} + \frac{\alpha_\gamma}{2r_2^2}\right) \mathcal{F}_f^\gamma(r_2) = \varepsilon_\gamma \mathcal{F}_f^\gamma(r_2) \quad (3.23)$$

We can define a real or complex angular momentum \tilde{l}_γ by rewriting the γ -th eigenvalue of A as $\alpha_\gamma \equiv \tilde{l}_\gamma(\tilde{l}_\gamma + 1)$. For the repulsive dipole case where $\alpha_\gamma > -1/4$, \tilde{l}_γ is real, while for the attractive dipole case \tilde{l}_γ is complex [24, 25, 26]. The details for the new reference wavefunction $\mathcal{F}_f^\gamma(r_2)$ and its corresponding long-range QDT parameters have been introduced in Subsec. 2.2.1.

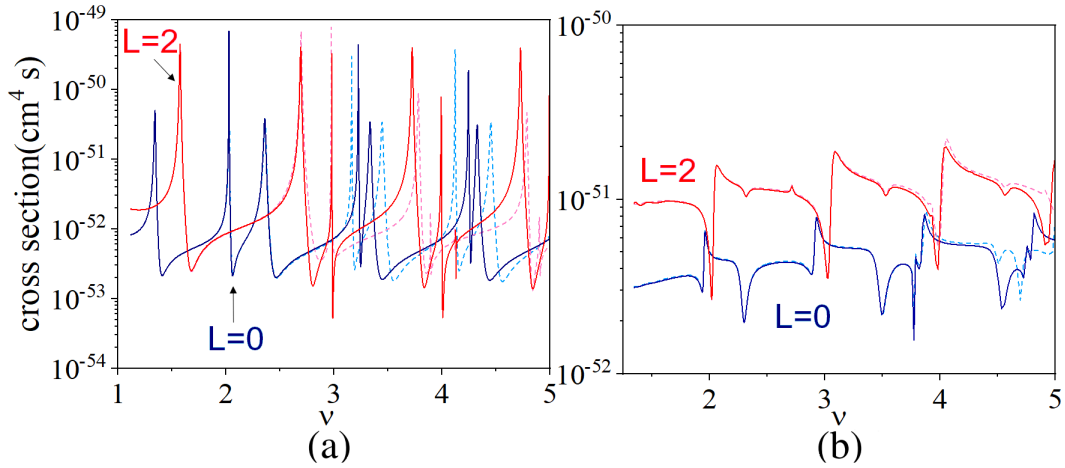


Figure 3.3. The comparison of calculations with (solid curve) and without (dashed curve) the Gailitis-Damburg dipole term for two-photon ionization cross section up to the $N = 2$ (a) and $N = 3$ (b) threshold. With the Gailitis-Damburg dipole term, the lineshapes change dramatically once the outer electron is outside the box.

The influences of the permanent dipole moment on the calculated spectra can be visualized from the two-photon cross-sections plotted up to the He^+ $N = 2$ and $N = 3$ thresholds in Fig.3.3. The horizontal axes are shown on an effective quantum number scale $\nu = 1/\sqrt{2(E_N - E_f)}$. At small ν , there are no differences since both electrons are in a resonance that is deeply bound, their motions are almost restricted to the interior of the R -matrix box [at $R_0 = 15(34)a.u.$ for $N = 2(3)$] which have been fully described by the R -matrix calculations. The differences appear only when ν is high enough that the outer

electron is active outside the box. In this regime, the Gailitis-Damburg-type treatment shifts the positions of resonances by approximately $\Delta\nu \approx 0.1$.

Besides improving the accuracy of calculations, the Gailitis-Damburg treatment also introduces a coupled channel representation $\{\gamma\}$ which is inherently different from the independent electron channel $\{i\}$. It connects to the $SO(4)$ group description of doubly excited states, which will be discussed in the next chapter.

3.2.3 Spectrum for two-photon ionization

This subsection studies two-photon ionization of ground-state helium ($1s^2$, singlet), under the linearly polarized field ($\omega_j = \omega, \hat{\epsilon}_j = \epsilon_0^{(1)}$) and trefoil field ($\omega_1 = 2\omega_2, \hat{\epsilon}_{1,2} = \epsilon_{\pm 1}^{(1)}$), whose energy diagrams and quantum numbers $^{2S+1}L^\pi$ have been given and discussed in Fig.3.1 and Fig.3.2. In this subsection, we only present the calculation results of generalized cross sections and angular distributions. The content in this subsection have been published in Ref. [58].

Two-photon Linear-polarized ionization

Our first calculation is for ionization with two linearly polarized photons along a common z -axis, where the final state energies considered are in the range from -0.9 to -0.223 a.u. The generalized cross sections for reaching the $^1S^e$ and $^1D^e$ symmetries and the asymmetry parameters β_2, β_4 are shown in Fig. 3.4, and the full set of Rydberg states converging to the $N = 2, 3$ thresholds are shown in detail in the lower two panels, displayed versus the effective quantum number $\nu = 1/\sqrt{2(E_N - E_f)}$ of the outer electron. The resonances below and above the $N = 2$ threshold have opposite Fano lineshape asymmetries: The cross-sections display Fano lineshapes with negative shape (q) parameters in the middle graph while positive q values occur in the right graph. Interestingly, it can be seen that the minimum of the cross-sections near the first few resonances fail to go to zero, as a feature of the above-threshold ionization. When resonances in that region are reached via single-photon ionization, they are guaranteed to have an exact zero in an LS -coupling calculation because they decay into only one channel and at one energy there will be perfect destructive interference.

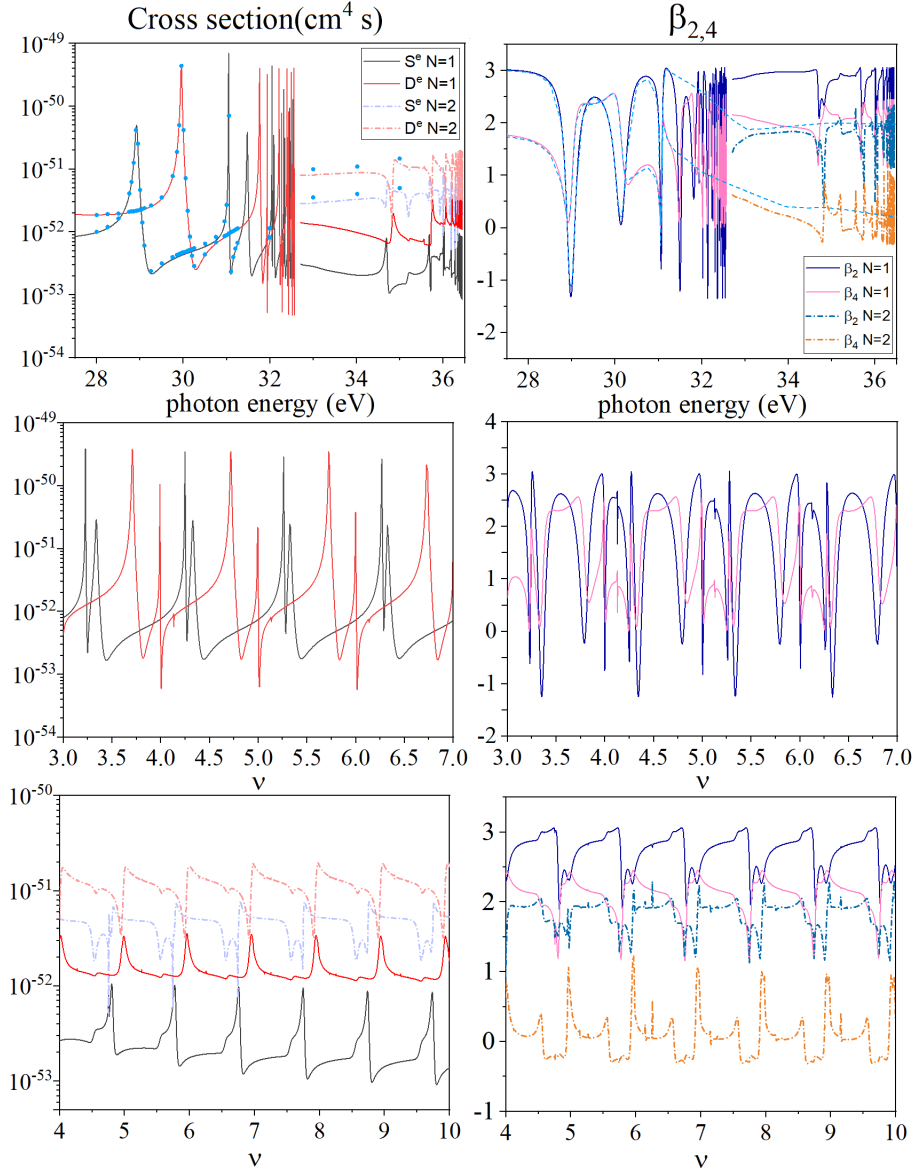


Figure 3.4. Partial cross sections (left) and $\beta_{2,4}$ parameters (right), as given in the label. The energy scale in the two highest panel is shown in terms of single photon energy. The blue points are taken from Boll *et al.* [59], as are the blue dashed curves for $\beta_{2,4}$. Their calculation is based on a $2 fs$ pulse duration so the narrow resonances are not resolved. The middle and lowest panels show an expanded version of the partial cross sections and $\beta_{2,4}$ parameters near $N = 2$ and $N = 3$ threshold, respectively, and are given on an effective quantum number scale for the outer electron, $\nu = 1/\sqrt{2(E_{N=2} - E_f)}$ and $\nu = 1/\sqrt{2(E_{N=3} - E_f)}$. This figure is taken from Ref.[58].

In addition, our results (solid lines) are compared with the Boll *et al.*[59] calculation that is based on a fully correlated time-dependent solution (the blue points and dashed lines) using a 2 fs laser pulse. When above the He⁺ $N = 2$ threshold, their calculation gives the total cross sections and asymmetry parameters while our calculation separates them into a fast($N = 1$) and slow($N = 2$) channel. The agreement is quite good at those energy points irrespective of the narrow resonance structures which are not resolved in their system. Our calculations are for monochromatic photons and include more energy mesh points, and hence are not limited in their energy bandwidth. The details of resonance structures near the $N = 2$ and $N = 3$ threshold are given in Fig.4.5 and 4.8 in the next Chapter.

Table 3.1. The energies(E) and decay widths(Γ) for the first three doubly-excited levels lying just below the $N = 2$ threshold (upper) and $N = 3$ threshold (lower), determined by previous works(given by the superscripts) and our calculations. (-x) indicates 10^{-x} . All the unit is in atomic unit(a.u.)

Levels	$N(K, T)_n$	This work: $E(\Gamma)$	Previous works: $E(\Gamma)$
$^1S^e(1)$	${}_2(1, 0)_2$	-0.7780(4.70(-3))	-0.7779(4.54(-3)) [5]
$^1D^e(1)$	${}_2(1, 0)_2$	-0.7018(2.37(-3))	-0.7004(2.59(-3)) [60]
$^1S^e(2)$	${}_2(-1, 0)_2$	-0.6222(2.36(-4))	-0.6219(2.16(-4)) [5]
$^1S^e(3)$	${}_2(1, 0)_3$	-0.5902(1.42(-3))	-0.5899(1.35(-3)) [5]
$^1D^e(2)$	${}_2(1, 0)_3$	-0.5691(5.77(-4))	-0.5687(6.17(-4)) [60]
$^1D^e(3)$	${}_2(0, 1)_3$	-0.5563(3.17(-5))	-0.5563(2.12(-5)) [60]
$^1S^e(1)$	${}_3(2, 0)_3$	-0.3534(3.00(-3))	-0.3535(3.01(-3)) [61]
$^1D^e(1)$	${}_3(2, 0)_3$	-0.3430(4.74(-3))	-0.34314(5.25(-3)) [62]
$^1S^e(2)$	${}_3(0, 0)_3$	-0.3174(6.32(-3))	-0.31745(6.66(-3)) [61]
$^1D^e(2)$	${}_3(0, 2)_3$	-0.3154(4.07(-3))	-0.3157(4.30(-3)) [62]
$^1D^e(3)$	${}_3(0, 0)_3$	-0.2900(1.41(-3))	-0.2900(1.20(-3)) [62]
$^1S^e(3)$	${}_3(2, 0)_4$	-0.2809(1.65(-3))	-0.2811(1.502(-3)) [61]

The resonance peaks in the calculation are associated with quasi-bound autoionizing final state levels. Our results for the first few autoionizing states are based on an R-matrix calculation that includes all the electron correlations, and their results are given in Table.3.1, which are compared with some previous results in the literature [5, 60, 61, 62], and show good general agreement.

Two-photon Trefoil field ionization

The total electric field of two separate lasers $\omega_1 = 2\omega_2$, $\hat{\epsilon}_{1,2} = \epsilon_{\pm 1}^{(1)}$ traces a trefoil figure (Fig. 3.5). When the laser intensity lies in the tunneling region, it can guide the liberated electrons away from the parent ion and back again, ensuring that head-on collisions occur from all sides during the laser cycle, therefore be widely used to generate high-harmonic laser sources with arbitrary polarization [63]. Its cross-section for multi-photon ionization is,

$$\sigma_{tot} = 8\pi^3 \alpha^2 \omega_1 \omega_2 \sum_f |T_{f,i}|^2$$

$$T_{f,i} = \sum_{\epsilon} dE_{\epsilon} \left(\frac{\langle f|D_2|\epsilon\rangle \langle \epsilon|D_1|i\rangle}{E_i + \omega_1 - E_{\epsilon}} + \frac{\langle f|D_1|\epsilon\rangle \langle \epsilon|D_2|i\rangle}{E_i + \omega_2 - E_{\epsilon}} \right). \quad (3.24)$$

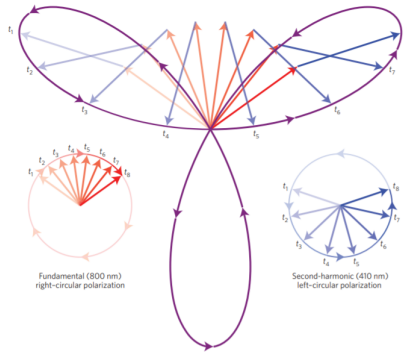


Figure 3.5. Combining a right-circularly polarized infrared driver (red arrows) with its left-circularly polarized second harmonic (blue arrows) at equal intensities yields a trefoil-shaped electric field (purple curve), which can guide electrons back to their parent ion to generate high harmonics with controllable polarization. Reprint from [63].

The relative phase and strength of the two laser fields are irrelevant. The results for the partial cross-sections and asymmetry parameters are shown in Fig. 3.6. Two intermediate state resonances are presented in the figures at -0.57 and -0.36 a.u., corresponding to the $1s2p$ and $1s3p \ ^1P^o$ intermediate excited states. At these energies, all the final state partial-waves experience that intermediate state resonance. The other resonances are from either $^1S^e$ or $^1D^e$ final states, and they are in the same position as in Fig. 3.4, giving the energy levels for doubly excited states. The parity-unfavored $^1P^e$ state in the continuum emerges only when

the energy reaches the $N = 2$ threshold at -0.5 a.u. since its lowest open channel is $2p\epsilon p$ feature, so below the $N = 2$ threshold, there are no scattering solutions for this symmetry, although there are metastable bound states that are perfectly stable and would show up as Dirac δ functions if we were to include them. The metastable ${}^1P^e$ states below the $N = 2$ threshold have not been included here although they could be observed experimentally.

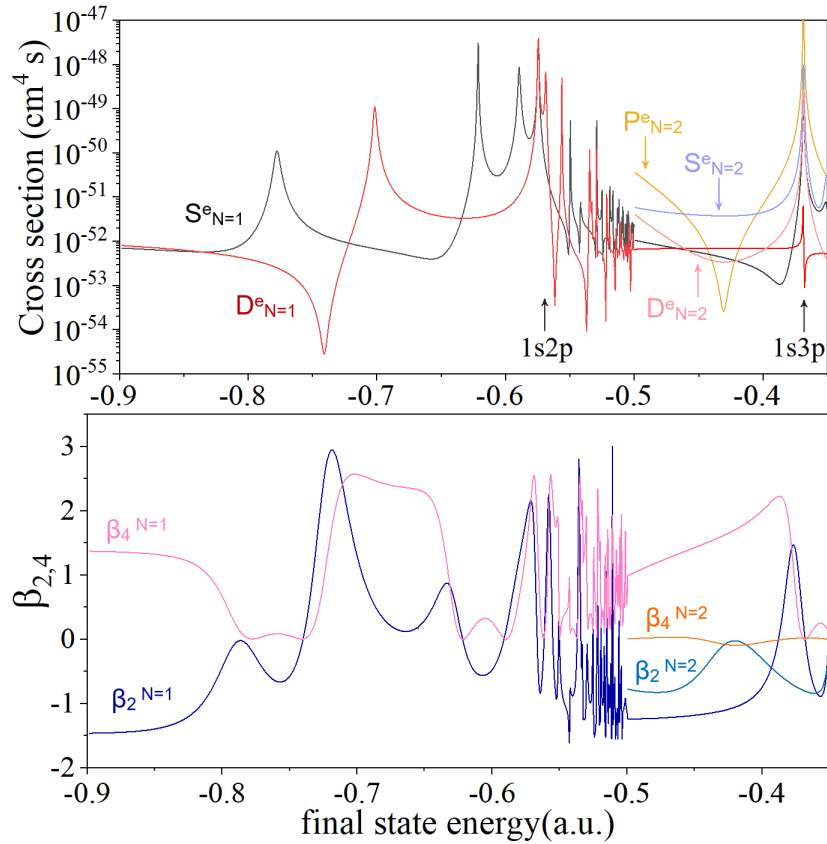


Figure 3.6. Partial wave cross sections (upper) and $\beta_{1,2,3,4}$ parameters (lower) for trefoil field ionization around $N = 2$ threshold. The parity unfavored state occurs when the energy is above $N = 2$ threshold at -0.5 a.u. The two identified peaks are from the $1s2p$, $1s3p$ intermediate resonance. This figure is taken from Ref.[58].

3.2.4 Spectrum for three-photon ionization

In this section, we briefly discuss the ionizations with three identical linearly polarized photons, the spectra we calculated are between the $N = 2$ and $N = 1$ thresholds and above

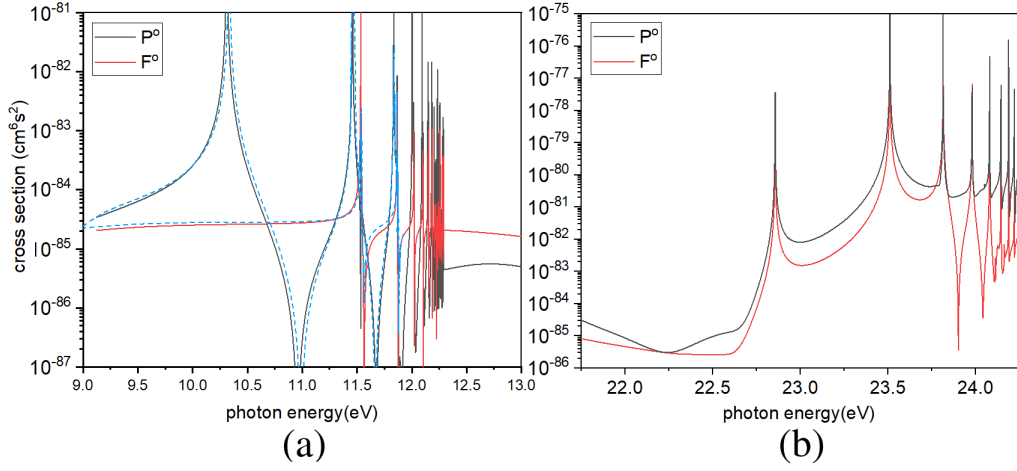


Figure 3.7. Three-photon-ionization cross section of helium with identical linearly polarized photons for (a) final state between $N = 2$ and $N = 1$ thresholds, our calculation (solid lines) are compared with Ref. [51] (dashed lines); and (b) final state above $N = 2$ threshold.

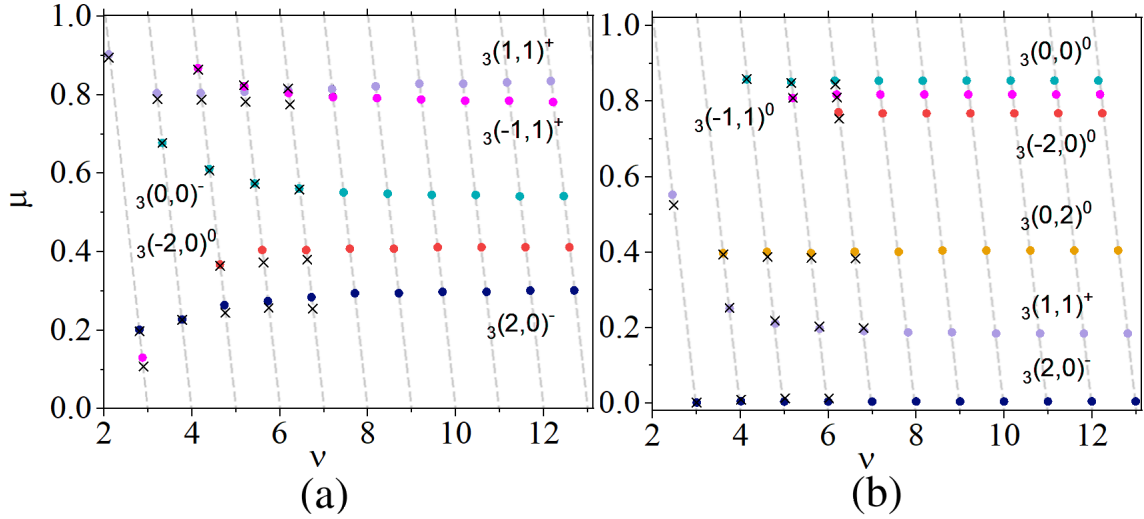


Figure 3.8. The quantum defect μ below $N = 3$ threshold is plotted versus the effective quantum number ν for $1P^0$ (left) and $1F^0$ (right) wave bound states. The black crosses are the truncated diagonalization calculation from [52]. The grey dashed curve has slope -1 since $\sin \pi(\mu + \nu) = 0$. The resonances are given in terms of ${}_N(K, T)^A$ quantum numbers

the $N = 2$ threshold. The final states are in ${}^1P^o$ and ${}^1F^o$ symmetry according to the angular selection rules. Our results in Fig.3.7 (a) have been confirmed by the spectrum calculated by Saenz et al. [51], as given in the dashed line. All the resonances presented come from the second intermediate states (which is ${}^1S^e$ and ${}^1D^e$ symmetry for ${}^1P^o$ state, and ${}^1D^e$ symmetry for ${}^1F^o$ state), especially, the $1sns$ and $1snd$ series. The final states lie in a flat continuum and do not contribute any resonance feature.

In Fig.3.7 (b) we show the spectrum between $N = 3$ and $N = 2$ thresholds, where a same series of resonances can be observed for both ${}^1P^o$ and ${}^1F^o$ symmetry. They come from the first intermediate ${}^1P^o$ states, $1snp$ series starts with $n = 3$. To demonstrate the doubly-excited autoionizing levels lying just below $N = 3$ threshold, we plot the quantum defect versus the effective quantum number $\nu = 1/\sqrt{2(E_{N=3} - E_f)}$ in Fig.3.8 from $\nu = 2 - 13$. For ${}^1P^o$ and ${}^1F^o$ symmetry there are total 5 and 6 open channels respectively. Those channels are labeled in ${}_N(K, T)^A$ quantum numbers, which will be discussed in the next chapter. The black crosses are the calculated results from Ref. [52], Table VII, which is based on the truncated diagonalization method. Although their method is not the most accurate one for autoionizing states, they could at least confirm the validity of our calculations.

3.3 Multi-photon ionization of barium

The spectrum of barium has been studied by a series of theoretical and experimental works[37, 38, 39, 40, 43, 44, 48], and our goal is to explore the coherent control property and to explain Yamazaki et al. experiment[37, 38], as we will introduce in detail in Chap. 7. In this section, we give the results for cross-section and beta parameters, and most importantly, derive the transition amplitudes $T_{f,i}$ under the influence of hyperfine depolarization, which lays the foundation of the coherent-control-discussion in Chapter 7.

Fig. 3.9 (a) gives the relevant energy levels the two- and three-photon ionization of barium. The ionization steps are as following: We firstly use a pump laser (ω_p) to excite the ground state atom i to the $e_1 = 6s6p$ (1P_1) state. Next, by the concurrent one- and two-photon ionization, the atom of the initially excited state reaches the shaded energy region, which can decay into either the continua associated with the $6s_{1/2}$ or the $5d_{3/2}$ ionic state.

An important consequence of the first step sequential excitation is, the atom will stay on the $6s6p(^1P_1)$ state (whose lifetime is around 8.4×10^{-9} sec) for a considerable time, which is sufficient for the nuclear and electron spin precessing with each other, causing a “hyperfine depolarization effect”, It some times can have a strong impact on ionization spectra and will be the main topic of this section.

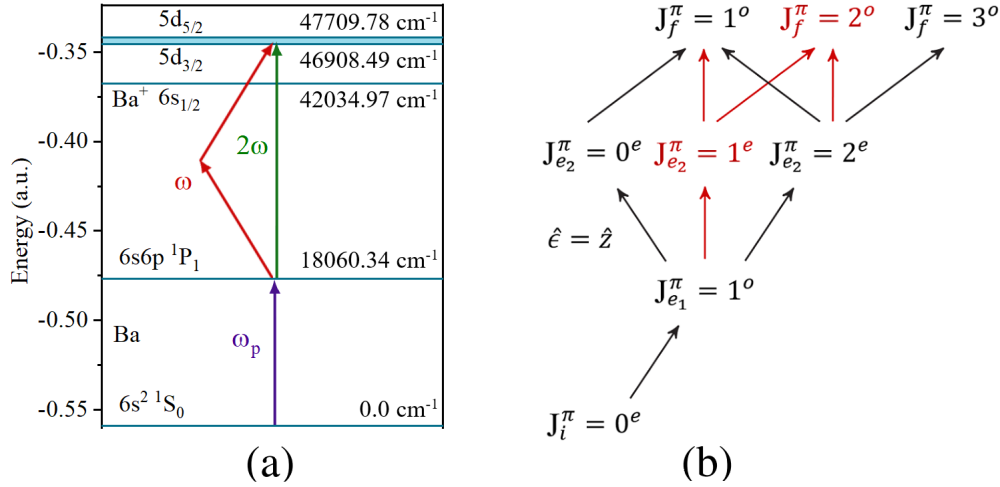


Figure 3.9. (a) The energy level diagram for the barium for $\omega-2\omega$ interference scheme. The ground state barium is firstly excited by a linearly-polarized pump laser (ω_p) to $e_1 = 6s6p\ (^1P_1)$ state, then by the concurrent one- and two-photon ionization, the atom reaches the shaded energy region, which can decay into either the continua associated with the $6s_{1/2}$ or the $5d_{3/2}$ ionic state. (b) The angular momenta J and parity π allowed by the electron-dipole selection rule (For the single photon $q = 1$ pathway, replace J_{e_2} by J_f). When the pump and ionization photons are both polarized along z-axis, the red paths are allowed only when the effect from hyperfine depolarization is included in the initially excited e_1 state. This figure is taken from Ref.[64].

All the photons in the ionization scheme are linearly polarized ($\hat{e} = \hat{z}$). The quantum numbers J^π permitted by the selection rule in each step of excitation are given in Fig. 3.9 (b). In the case that no hyperfine depolarization is involved, only the black paths are allowed. However, with nuclear spin \vec{I} and electronic angular momentum \vec{J} precessing along with each other on the $6s6p(^1P_1)$ state, $M_{J_{e_1}}$ is no longer a good quantum number of the system, that parity unfavored states are introduced into the excitation scheme (the red paths).

3.3.1 Hyperfine depolarization effects

The hyperfine structure is important in atomic barium because it breaks ordinary electronic selection rules. Natural barium consists of two isotopes with different nuclear spins: The $I = 0$ isotopes constitute 82% while the remaining 18% are $I = \frac{3}{2}$ isotopes [65]. The latter experience hyperfine splittings, and hence one can visualize semiclassically that the nuclear spin \vec{I} and electronic angular momentum \vec{J} precess about the total angular momentum \vec{F} . Differences between the hyperfine levels E_F usually are in the range of hundreds of MHz to a few GHz . A crucial point is that in the first step of the experiment, where a high-frequency pump laser ω_p is used to excite ground state barium to $e_1 = 6s6p$ (1P_1), the resolution of the pump laser is around 1 cm^{-1} which cannot resolve the hyperfine levels. Moreover, the excitation step can be viewed as *sudden* in comparison with the time scale of hyperfine-induced precession of \vec{J} . Hence “quantum beats” between different (F, M_F) are expected, with the transition amplitude $T_{f,i}$ now written as a coherent sum over the indistinguishable pathways: [66].

$$\begin{aligned}
T_{f,i}^{(q,I=0)} &= T_{f,e_1}^{(q)} \langle J_{e_1} M_{J_{e_1}} | \hat{\epsilon}_p \cdot \vec{r}_p | J_i M_{J_i} \rangle \\
T_{f,i}^{(q,hfp)} &= T_{f,e_1}^{(q)} \sum_{FM_F M_{F_i}} \frac{e^{i\omega_{FF_i} t}}{2I + 1} \langle J_{e_1} M_{J_{e_1}}, IM'_I | F, M_F \rangle \langle (J_{e_1}, I) F, M_F | \hat{\epsilon}_p \cdot \vec{r}_p | (J_i, I) F_i, M_{F_i} \rangle \\
&\quad \langle F_i, M_{F_i} | J_i M_{J_i}, IM_I \rangle
\end{aligned} \tag{3.25}$$

Where $T_{f,i}^{(q,I=0)}$ is the transition amplitude assuming no hyperfine structures, and $T_{f,i}^{(q,hfp)}$ includes the hyperfine structures and quantum beats from the laser-pump step, it depend on the orientation of \vec{I} . After averaging (summing) over initial states I, M_I (final states I, M'_I) in Eq. 7.1, the whole process is azimuthal symmetric. Here we separate the pump step $i \rightarrow e_1$ and the ionization steps $e_1 \rightarrow f$, and we neglect the precession effects during the very short time of the ionization processes $e_1 \rightarrow f$. The amplitudes for the individual ionization steps are,

$$T_{f,e_1}^{(q)} = \begin{cases} \langle [j_1, (l_2, s_2)j_2] J_f M_f | \hat{e}_1 \cdot \vec{r}_1 | J_{e_1} M_{e_1} \rangle & q = 1 \\ \sum_{e_2} \frac{1}{E_{e_2} - E_{e_1} - \omega} \langle [j_1, (l_2, s_2)j_2] J_f M_f | \hat{e}_2 \cdot \vec{r}_2 | e_2 \rangle \langle e_2 | \hat{e}_1 \cdot \vec{r}_1 | J_{e_1} M_{e_1} \rangle & q = 2 \end{cases}$$

The next step is to calculate the differential ionization rate $\frac{dW}{d\Omega}$ in Eq. 7.1 and the ionization cross-sections with $T_{f,i}^{(q,hfp)}$. The total cross-section including both the pump step and the q -photon ionization step just follow Eq.3.2:

$$\sigma_{i \rightarrow f}^{(q)} = 2\pi(2\pi\alpha)^{q+1} \omega^q \omega_p \left| T_{f,i}^{(q)} \right|^2 \quad (3.26)$$

The effect of hyperfine depolarization to cross-sections can be parameterized by a factor $g^{(k)}(t)$, as stated in Ref. [46, 66] for the pump plus one-photon ionization. We generalized it into a pump plus two-photon ionization case [67, 68]. The formula for $\sigma_{i \rightarrow f}^{(q=1,2,hfp)}$ can be expressed in terms of Wigner $6J$, $9J$ operators, polarization tensors $[\hat{e} \hat{e}^*]_{\mu}^{(k)}$ (which is $E_{\mu}^k(\hat{e}, \hat{e}^*)$ in Ref. [66]) and reduced matrix elements as following ($[k] \equiv \sqrt{2k+1}$):

$$\begin{aligned} \sigma_{i \rightarrow f}^{(1,hfp)} &= 2\pi(2\pi\alpha)^2 \omega \omega_p \left| \langle f || r_1^{(1)} || e_1 \rangle \langle e_1 || r_p^{(1)} || i \rangle \right|^2 \times \sum_k \sum_{\mu} (-1)^{\mu} [\hat{e}_p \hat{e}_p^*]_{\mu}^{(k)} [\hat{e}_1 \hat{e}_1^*]_{-\mu}^{(k)} g^{(k)}(t) \\ &\times (-1)^k \begin{Bmatrix} J_{e_1} & J_{e_1} & k \\ 1 & 1 & J_i \end{Bmatrix} \begin{Bmatrix} J_{e_1} & J_{e_1} & k \\ 1 & 1 & J_f \end{Bmatrix} \end{aligned} \quad (3.27)$$

$$\begin{aligned} \sigma_{i \rightarrow f}^{(2,hfp)} &= 2\pi(2\pi\alpha)^3 \omega^2 \omega_p \sum_{J_{e_2}, J'_{e_2}} \left| \langle f || r_2^{(1)} || e_2 \rangle \langle e_2 || r_1^{(1)} || e_1 \rangle \langle e_1 || r_p^{(1)} || i \rangle \right|^2 \times \sum_{k,k',k''} \sum_{\mu} (-1)^{\mu} \\ &\times [\hat{e}_p \hat{e}_p^*]_{\mu}^{(k)} \left\{ [\hat{e}_1 \hat{e}_1^*]^{(k')} [\hat{e}_2 \hat{e}_2^*]^{(k'')} \right\}_{-\mu}^{(k)} g^{(k)}(t) (-1)^{k+k'+J_i+J_{e_1}+J_{e_2}+J_f} [k'] [k''] \\ &\times \begin{Bmatrix} J_{e_1} & J_{e_1} & k \\ 1 & 1 & J_i \end{Bmatrix} \begin{Bmatrix} J_{e_2} & J'_{e_2} & k'' \\ 1 & 1 & J_f \end{Bmatrix} \begin{Bmatrix} J_{e_2} & 1 & J_{e_1} \\ J'_{e_2} & 1 & J_{e_1} \\ k'' & k' & k \end{Bmatrix} \end{aligned} \quad (3.28)$$

where k is the rank of tensor ($k = 0, 1, 2$), and $g^{(k)}(t)$ is,

$$g^{(k)}(t) = \sum_{F,F'} \frac{(2F+1)(2F'+1)}{2I+1} \cos(\omega_{FF'}t) \begin{Bmatrix} J_{e_1} & J_{e_1} & k \\ F & F' & I \end{Bmatrix}^2$$

$g^{(0)}(t) = 1$, when $I = 0$, $g^{(k)}(t) = 1$. Similarly, in the limit $t \rightarrow 0$ when there is no time for spin procession, $g^{(k)}(0) = 1$, and $\sigma_{i \rightarrow f}^{(q,hfp)} = \sigma_{i \rightarrow f}^{(q,I=0)}$. In the limit of complete depolarization $t \rightarrow \infty$, which is close to the case we studied, the terms with $F \neq F'$ average to 0.

Now we consider the situation where the pump and ionization lasers are linearly polarized and aligned with \hat{z} (the Yamazaki et al. experiment). The cross-section calculations for one- and two-photon ionization ($e_1 \rightarrow f$) starts from $e_1 = 6s6p (^1P_1)$; fundamentally, hyperfine depolarization simply mixes different $M_{J_{e_1}}$ sublevels. To an excellent approximation, only $M_{J_{e_1}} = 0$ is initially excited since all laser linear polarization axes are parallel to the z -axis. Then when \vec{J} precesses about \vec{F} , other $M_{J_{e_1}}$ states get populated as time evolves. The ionization cross-section is determined by,

$$\begin{aligned} \sigma_{e_1 \rightarrow f}^{(q,hfp)} &= \sum_{M_{J_{e_1}}} \sigma_{e_1 \rightarrow f}^{(q,I=0)} \left[\frac{1}{3} + \left(\frac{2}{3} - |M_{J_{e_1}}| \right) g_{ave}^{(2)} \right] \\ \sigma_{e_1 \rightarrow f}^{(q,I=0)} &= 2\pi(2\pi\alpha\omega)^q |T_{f,e_1}^{(q)}|^2, \quad M_{J_{e_1}} = 0, \pm 1 \end{aligned} \quad (3.29)$$

where $g_{ave}^{(2)} = 0.8644$, which is obtained by averaging over the isotope nuclear spins and in the long time limit. Here θ_p is the polarization angle between the linear-polarized pump and the ionization laser polarizations[66], taken to be 0 in our calculations.

3.3.2 Spectrum for multiphoton ionization

With formulas introduced in the last subsection, some calculation results are given in this subsection to illustrate the spectrum of barium atoms. An example demonstrating how hyperfine depolarization can lead to resonance states that do not exist for $I = 0$ isotope is given in Fig.3.10, where a $J^\pi = 1^e$ intermediate resonance has dramatically altered the spectrum, which already has been observed in experiments[39]. Our calculated cross-section

agrees with the earlier theoretical ones by an overall factor [39], with the solid and dashed curves are the results with and without the hyperfine depolarization. As we can see, the strong signature can not be obtained in our calculations if the hyperfine depolarizations are neglected. Although the hyperfine depolarization inherently changed the analysis of the ionization process, it doesn't influence the results distinctively when the energy being considered is far away from those resonance energies.

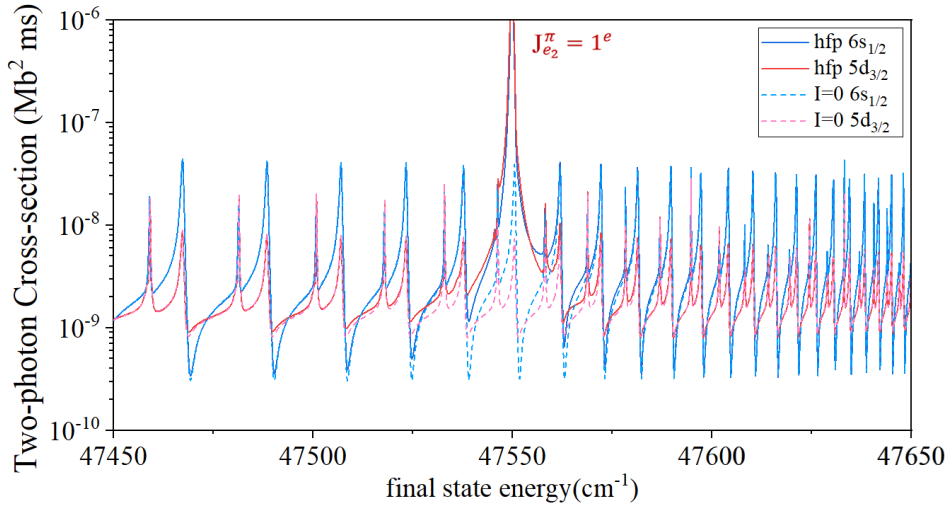


Figure 3.10. Two-photon generalized cross sections for $6s_{1/2}$ (blue) and $5d_{3/2}$ (red). The strong peak around 47549.5 cm^{-1} in the spectrum is due to the existence of an intermediate state resonance $5d7s \text{ } ^3D_1$ state, which has total angular-momentum $J = 1$ and therefore exists only when there is depolarization[39].

Besides the cross-section, the asymmetric parameters $\beta_k^{(6s^{1/2}, 5d^{3/2})}$ for separate $q = 1, 2$ are calculated and shown in Fig. 3.11, and are compared with experimental results [37]. The solid and dashed curves are the results with and without the hyperfine depolarization. As we can see, by including the hyperfine depolarization, the difference between calculated and experimental β_k (points) becomes smaller. Although the calculations give different amplitudes to the experiment, similarities can still be found in their lineshapes. Noted that β_6 for a one-photon pathway should be 0 from theoretical considerations, but the experimental fitting gave a nonzero value. It is interesting to note that the phase lag calculation (see Fig.7.3), which is derived from the $\beta_{k=odd,even}$ and will be introduced in Chap.7, is much

more satisfactory with experiment than Fig. 3.11, suggesting the phase lag could be more robust against small errors.

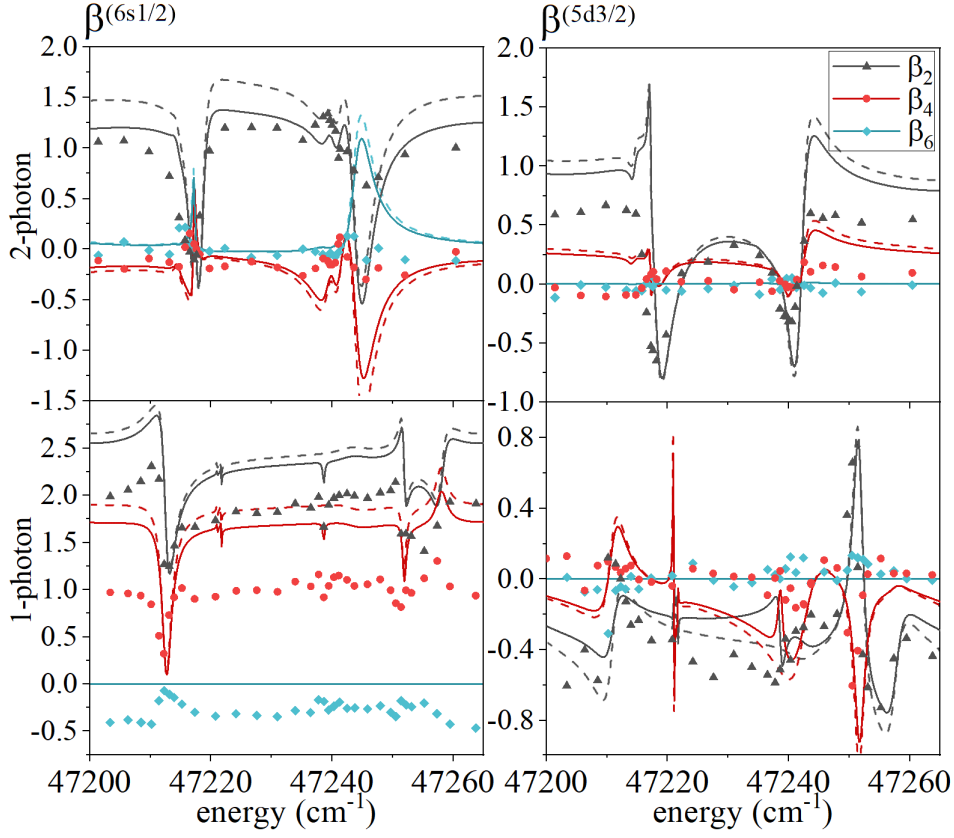


Figure 3.11. The photoelectron angular distribution parameters β_k for ionization process with $q = 1, 2$. Our calculations (solid curves) are compared to the experimental results (points) from Ref. [37] Fig. 6 and 7. Calculations assuming $I = 0$ is given in dashed lines for reference. The left and right panels gives β parameters for channel $6s^{1/2}$ and $5d^{3/2}$. This figure is taken from Ref.[64].

To conclude, we provide a systematic analysis of the role of hyperfine depolarization on barium multiphoton ionization, and develop formulas for differential cross-sections and three-photon ionization cross-sections, which have not been included by previous work; these discussions will be essential for the coherent control and phase lag studies of barium in Chap. 7.

4. THE CORRELATION EFFECTS OF ATOMIC HELIUM

In this chapter a new way of characterizing electron correlations in doubly excited states, the ${}_N(K, T)_n^A {}^{2S+1}L^\pi$ classification scheme, will be introduced, following the discussion of Herrick, Sinanoglu and Lin[4, 69, 70]. It has the physical origin from $SO(4)$ group and is closely associated with the hyperspherical coordinate and Gailitis-Damburg eigenchannels. Based on the $SO(4)$ correlated classification scheme, we will classify the resonances near the $N = 3$ threshold and test the propensity rules that have been confirmed to operate in the ${}^1P^o$ states reached by the single-photon ionization but have never been discussed in the multi-photon region. Some of the discussions has been published in Ref.[58], coauthored with Chris H. Greene.

4.1 Classification scheme

4.1.1 Group description of electrons in Coulomb potential

The goal of this subsection is to introduce the $(K, T)^A$ classification scheme which origins from the group description of one and two electrons in a Coulomb potential. As is known, a single electron bounded in Coulomb potential $V(r) = -Z/r$ exhibits an $SO(4)$ symmetry, which is generated by its angular momentum \vec{l} and the Runge-Lenz vector \vec{a} , whose classical interpretation is that it points in the direction of the major axis of the elliptical Kepler orbit with magnitude equals to the orbit's eccentricity. The quantum analog of the Runge-Lenz vector is:

$$\vec{a} = \frac{1}{(-2H)^{1/2}} \left[\frac{1}{2}(\vec{p} \times \vec{l} - \vec{l} \times \vec{p}) - Z\hat{r} \right] \quad (4.1)$$

\vec{l} and \vec{a} generates an $SO(4)$ algebra, with Casimir invariants, $C_1 = \vec{l}^2 + \vec{a}^2 = \frac{Z^2}{(-2H)^{1/2}} - 1 = n^2 - 1$ and $C_2 = \vec{l} \cdot \vec{a} = 0$. It is the largest invariant group of a hydrogenic Hamiltonian. However, there is actually a larger group that can generate all the bounded eigenstates of the

system (therefore not commutative with the Hamiltonian), which is the $SO(4, 2)$ group, whose communication relation can be expressed by such anti-symmetric matrix[71]:

$$L_{ab} = -L_{ab} \leftrightarrow \begin{bmatrix} 0 & l_3 & -l_2 & \tilde{a}_1 & b_1 & \Gamma_1 \\ \dots & 0 & l_1 & \tilde{a}_2 & b_2 & \Gamma_2 \\ & \dots & 0 & \tilde{a}_3 & b_3 & \Gamma_3 \\ & & \dots & 0 & T_2 & T_1 \\ & & & \dots & 0 & T_3 \\ & & & & \dots & 0 \end{bmatrix} \quad (4.2)$$

where \vec{a} is the rescaled Runge-Lenz vector: $\vec{a} = \frac{1}{2}\vec{r}\vec{p}^2 - \vec{p}(\vec{r} \cdot \vec{p}) - \frac{1}{2}\vec{r}$, $\vec{b} = \vec{a} + \vec{r}$, $\vec{\Gamma} = r\vec{p}$, $T_1 = \frac{1}{2}(rp^2 - r)$, $T_2 = \vec{r} \cdot \vec{p} - i$, $T_3 = \frac{1}{2}(rp^2 + r)$. The complete set of communication relation can be expressed as,

$$[L_{ab}, L_{cd}] = -i(g_{ac}L_{bd} + g_{bd}L_{ac} - g_{bc}L_{ad} - g_{ad}L_{bc}) \quad (4.3)$$

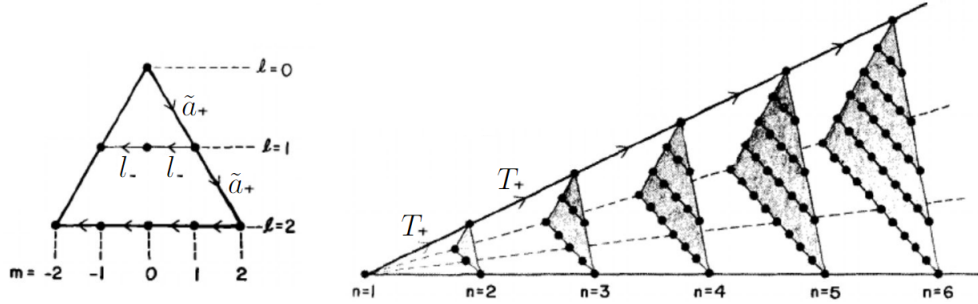


Figure 4.1. Subtower and complete tower of $SO(4, 2)$ of scaled hydrogenic state. Reprint from Ref. [71], Fig.1.

where $g_{ab} = 0$ when $a \neq b$, $g_{aa} = -1$ when $a = 1 - 4$, $g_{aa} = 1$ when $a = 5, 6$. All the bounded states $|n, l, m\rangle$ can be obtained by applying $SO(4, 2)$ raising/lowering operators to the ground state,

$$|n, l, m\rangle = \frac{(-1)^l}{2^l l! (n-1)!} \left(\frac{(2l+1)(n-l-1)!(l+m)!}{(n+l)!(l-m)!} \right)^{\frac{1}{2}} (l_-)^{l-m} (\tilde{a}_+)^l (T_+)^{n-1} |1, 0, 0\rangle \quad (4.4)$$

Which is illustrated in Fig. 4.1.

Now we consider the group description for doubly excited states in atoms such as H^- and He [69]. With two-electron moving in a Coulomb field, the electric correlation $1/r_{12}$ makes the Hamiltonian non-separable. Since not a simple group representation has been found, people have to turn to the approximate description of such a system. One way to approach the approximate description is to find a $SO(4)$ subgroup of the non-correlated two-electron system $SO(4)_1 \times SO(4)_2$, which can diagonalize $1/r_{12}$ to the largest extent. It turns out the best choice is the $SO(4)$ group generate by $\vec{L} = \vec{l}_1 + \vec{l}_2$ and $\vec{B} = \vec{a}_1 - \vec{a}_2$ [72]. Given each \vec{a}_i pointing to the major axis of the elliptical orbital of electron i , \vec{B} can be regarded as a measure of the inter-electron distance. \vec{L} is the total angular momentum. The Casimir invariants of the $SO(4)$ group can be written as:

$$\vec{B}^2 = [(n + K)^2 + T^2 - 1 - L(L + 1)]^2 \quad \vec{B} \cdot \vec{L} = T^2(K + n)^2 \quad (4.5)$$

We could therefore determine new quantum numbers from this group, to replace the non-correlated basis set $\{N, l_1, n, l_2\}$ ($N = n_1, n = n_2$). The new quantum numbers K and T for given N and L can be,

$$\begin{aligned} T &= 0, 1, 2, \dots, \min(L, N - 1) \\ K &= N - 1 - T, N - 3 - T, \dots, -(N - 1 - T) \end{aligned} \quad (4.6)$$

$(K, T) 2^{S+1}L^\pi$ give the so called ‘‘doubly-excited symmetry basis’’[73]. Although they cannot describe accurately the intershell Coulomb mixings, they preserve at least the dipole interaction in the asymptotic limit ($n \rightarrow \infty$)[4],

$$\begin{aligned} 2r_1 \cos \theta_{12} &= \frac{3N}{n} \vec{a}_1 \cdot \vec{a}_2 = -3NK + \frac{3N}{2n} [N^2 - 1 - T^2 - 2 - K^2 + L(L + 1) - 2 - \hat{l}_1^2 - \hat{l}_2^2] \\ &\xrightarrow{n \rightarrow \infty} -3NK \end{aligned} \quad (4.7)$$

According to Eq.4.5 and 4.7, T has been identified with the pseudoscalar operator $(\vec{L} \cdot \vec{r}_{12})$, when $T = 0$, the states have one-electron structure. K measures the number of nodes in

the body frame associated with θ_{12} , and the maximal positive K corresponds to the most centripetal term that decreases the long-range potential.

The radial correlation is parameterized by the quantum number A , which is determined by the following relations,

$$A = \begin{cases} \pi(-1)^{S+T} = \pi(-1)^{S+N-K+1} & K > L - N \\ 0 & K \leq L - N \end{cases} \quad (4.8)$$

$A = +1(-1)$ indicates an approximate antinodal (nodal) structure at or near the line $r_1 = r_2$, and $A = 0$ indicates neither of them [10]. In the rest part of this chapter, we will classify the autoionizing resonances based on the ${}_N(K, T)_n^A 2^{S+1} L^\pi$ quantum numbers. Our calculations on the helium linearly polarized ionization in the last chapter, which includes the electron correlation up to the dipole term, will be discussed. The propensity rules, which can be regarded as a generalization of the angular momentum selection rule, will be explored in the multi-photon ionization and autoionizing decaying processes.

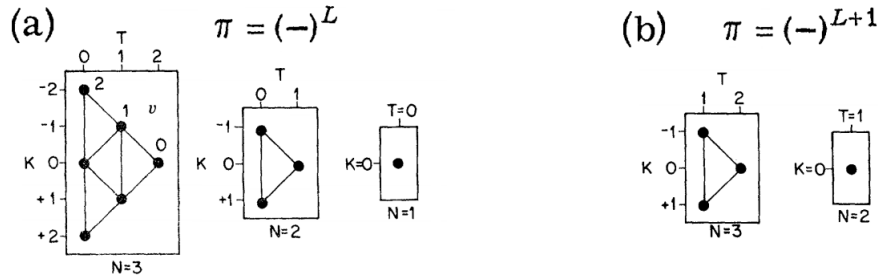


Figure 4.2. Possible values of K and T labeling resonance channels of H -like systems for (a) parity favored $\pi = (-1)^L$ and (b) parity unfavored $\pi = (-1)^{L+1}$ states. The lines connecting the points represent channels coupling between l_2^{-2} . Reprint from Ref. [4], Fig.1, 2.

4.1.2 Hyperspherical description of electronic correlations

Another way of revealing the physical significance of the electronic correlation is to use the hyperspherical coordinates [9]. Apart from the three translational-invariant coordinates, the internal coordinates for two-electron in a nucleus field are given below:

$$R = (r_1^2 + r_2^2)^{1/2} \quad \alpha = \tan^{-1}(r_2/r_1) \quad \theta_{12} = \cos^{-1}(\hat{r}_1 \cdot \hat{r}_2) \quad (4.9)$$

Where R specifies the overall size of the atom, and the electron correlations is encoded by the angles, $\Omega = (\alpha, \theta_{12})$, with α specify the radial correlation and θ_{12} specify the angular correlation [10, 70]. In hyperspherical coordinates, the adiabatic approximation [10, 70, 74] of doubly excited state is given by,

$$\Psi = R^{-5/2} (\sin \alpha \cos \alpha)^{-1} \sum_{\mu} \Phi_{\mu}(R, \Omega) \mathcal{F}_{\mu}(R) \quad (4.10)$$

By treating the hyperspherical radius R parametrically, the channel functions $\Phi_{\mu}(R, \Omega)$ are obtained by solving the equation below, whose eigenvalues $U_{\mu}(R)$ give the diabatic channel potentials (to preserve the correlation pattern for each channel, diabatic states are preferred in regions of avoided crossings):

$$\left(-\frac{1}{R^2} \frac{d^2}{d\alpha^2} + \frac{\vec{l}_1^2}{R^2 \cos^2 \alpha} + \frac{\vec{l}_2^2}{R^2 \sin^2 \alpha} + \frac{2C}{R} \right) \Phi_{\mu}(R, \Omega) = U_{\mu}(R) \Phi_{\mu}(R, \Omega) \quad (4.11)$$

$$C = -\frac{Z}{\cos \alpha} - \frac{Z}{\sin \alpha} + \frac{1}{\sqrt{1 - \sin 2\alpha \cos \theta_{12}}}$$

The channel index μ can be labeled by quantum number ${}_N(K, T)_n^A 2^{S+1} L^{\pi}$ [70]. The channel potentials $U_{\mu}(R)$ have visualize different ${}_N(K, T)_n^A 2^{S+1} L^{\pi}$ states, as shown in Fig.4.3, which gives the some hyperspherical potentials converging to the He^+ $N=3$ threshold.

These potential curves confirm the following features for ${}_N(K, T)_n^A$ [70]: 1. $A = +$ curves have smaller centrifugal potential at small R , therefore are more likely to penetrate into a small R region and are lower in energy. Therefore, the electrons in these channels spend considerable time near the nucleus where they interact strongly with each other, making their

autoionization states unstable and decay relatively rapidly; the corresponding resonances are relatively broader than states in the other nearby channels. 2. at large R , there is no definite ordering between + and - curves, but $A = 0$ curves correspond to the higher ones. In addition, in the asymptotic limit, a larger K value corresponds to a lower potential curve, and for fixed K , a larger T corresponds to a lower curve, as the long-range potentials are controlled by the dipole interaction. 3. channels with identical $(K, T)^A$ have similar shapes of potentials, and those curves belonging to higher L lie slightly higher, which come from contributions of rotational energy. A supermultiplet structure can be observed in the lowest eigenvalues of each group of $(K, T)^A$ ($A \neq 0$) curves according to Ref. [70].

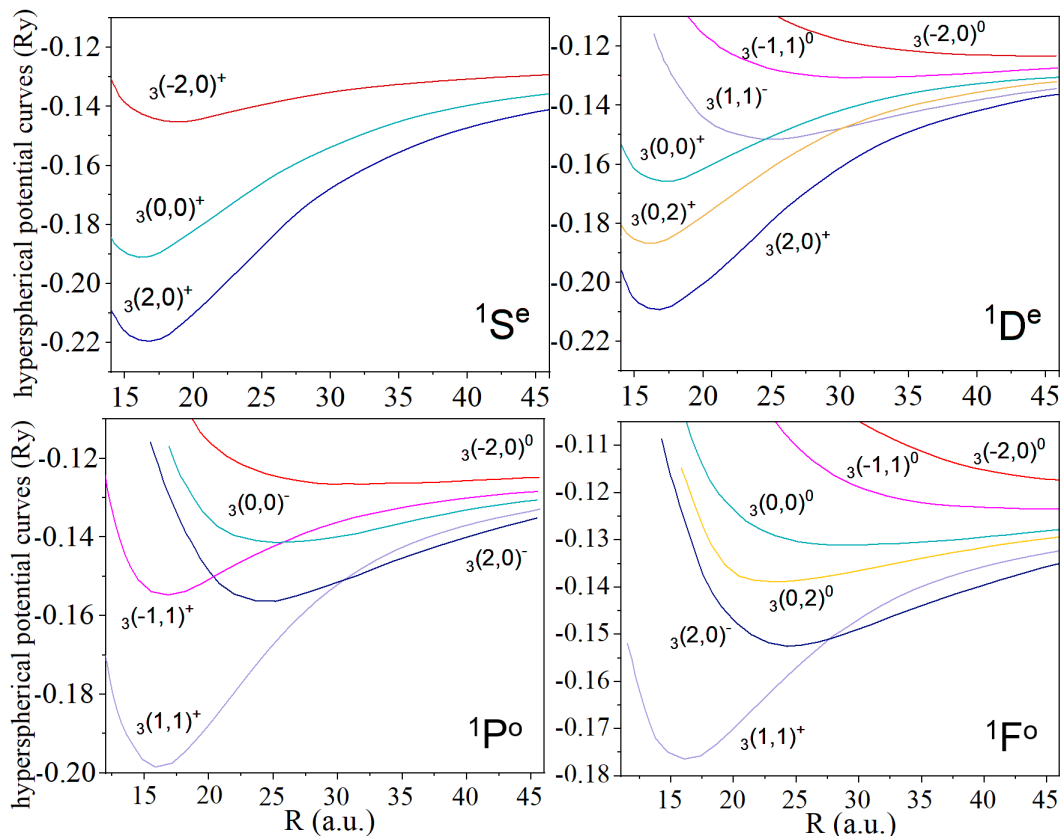


Figure 4.3. Hyperspherical potential curves for $1S^e$, $1P^o$, $1D^e$, and $1F^o$ for the helium atom that converge to the He^+ $N=3$ threshold. Reduced units with $Z = 1$ are used, as defined by Lin, namely the horizontal axis has units of Bohr radius divided by $Z = 2$ while the vertical (energy) axis has units of Hartree multiplied by Z^2 . Reprinted from Fig.1. of Lin.[70].

With the aid of Fig.4.3, one can ascertain the connection between the ${}_N(K, T)^A$ channels and the Gailitis-Damburg channels γ outside our R-matrix box radius at $R_0 = 34$, where there are no more crossings among the hyperspherical curves. The correspondence between the ${}_N(K, T)^A$ and γ can be deduced by matching the most centrifugal channel a_γ (Eq.3.23) to $(K, T) = (-2, 0)^+$ for ${}^1S^e$ symmetric or to $(K, T) = (-2, 0)^0$ for ${}^1P^o$, ${}^1D^e$, and ${}^1F^o$ symmetric and so on, as explained by point 2 above. This analysis allows us to classify the resonances in the ${}_N(K, T)^A$ scheme of approximately good quantum numbers and to discuss the validity of propensity rules for photoexcitation and decay in the next section.

4.2 The study of propensity rules

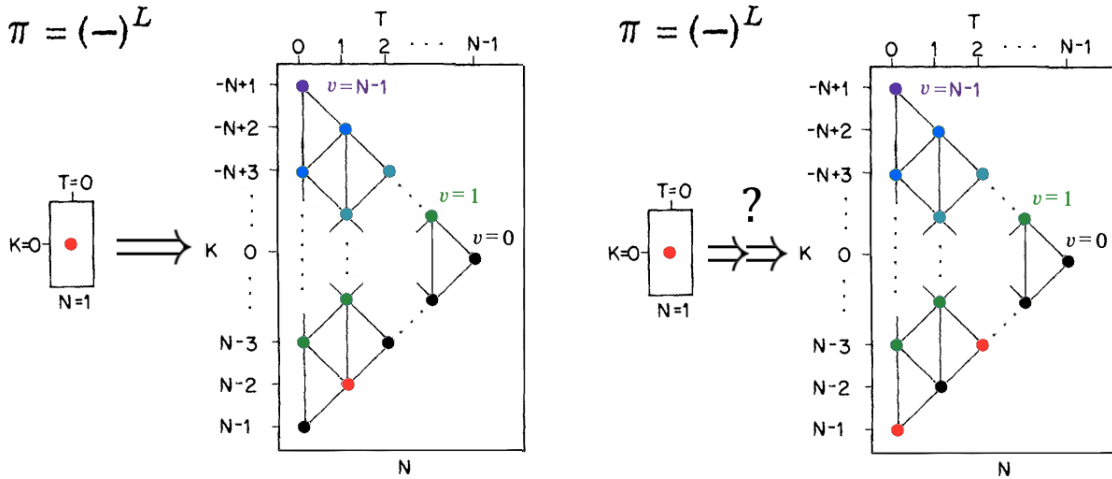


Figure 4.4. A demonstration on photoionization propensity rule for $\Delta T = 1$ and $K = K_{max}$ for $\pi = (-1)^L$ states, the desirable transition from ground state ${}_1(0, 0)^+$ are colored in red. Other colors of the lattice indicate different values for $v = \frac{1}{2}(N - 1 - K - T)$.

In an earlier study[75], single-photon-absorption processes up to the He^+ $N = 7$ threshold were measured. A “propensity rule” was observed, indicating that the dominant channel in the linearly polarized photoexcitation process should satisfy $\Delta A = 0$, $\Delta T = 1$ and $K = K_{max}$ [10, 75]. For example, in the ground state helium ${}_1(0, 0)^+$ single photoabsorption process, the ${}_N(N - 2, 1)^+$ channels play a major role. Another propensity rule that has been widely discussed describes the predominant decay channel of resonances. Usually, the vibra-

tional quantum number $v = \frac{1}{2}(N - 1 - K - T)$ is used when discussing the decaying processes, $v = 0$ indicates the electrons have only a zero-point motion in the bending coordinate θ_{12} . The propensity rule for the dominant decay channel of a resonance is: $\Delta N = -1, \Delta A = 0, \Delta v = 0$ [57, 76]; this rule is has been tested for the lowest ($v = 0$) and second lowest ($v = 1$) channel resonances for helium atoms[74]. Those phenomenological rules indicate that the radial correlation will not be changed by the photoionization or decaying process, but the angular distribution (K, T) would change in the photoionization or decaying process. Most of the discussions in this section are adapted from Ref.[58].

This section discusses the propensity rules for multi-photon excitation of helium and autoionizing decay. If the propensity rule still holds for two-photon ionization, we would expect partial cross sections in ${}_N(K_{max}, 0)^+$ and ${}_N(K_{max}, 2)^+$ channels dominant over the other channels (actually the only dominant channel should be ${}_N(K_{max}, 0)^+$ since $T = 2$ has not been included). Our analysis considers ionization by identical photons that reach final states above the $N = 2$ threshold, since it is the lowest energy range that allows the electrons to escape into different channels. To get the maximum resolution of some very narrow resonances, the energy range analyzed here includes just one cycle of the Rydberg series converging to the $N = 3$ threshold, in the range of effective quantum number, $\nu = 12 - 13$.

The time-delay matrix is used to analysis the decay processes and the life time: $\underline{Q}^{phys} = -i\underline{S}^{phys\dagger} \frac{d\underline{S}^{phys}}{dE}$, where \underline{S}^{phys} is the physical scattering matrix and id/dE is the quantum time operator. The largest eigenvalue q_{max} of the Hermitian \underline{Q}^{phys} gives the longest scattering delay in general and peaks whenever there is a resonance with a peak value related to the resonance decay lifetime. The dominant decay channel of that resonance is given by the eigenvector corresponding to that q_{max} .

The two-photon ionization partial cross-sections are shown in Fig. 4.5. The three open channels in ${}^1S^e$ symmetry are shown Fig. 4.5.(a). We can see the $N = 2$ channels play a more important role than the $N = 1$ channel, which agrees with the propensity rule that the channel with $N = N_{max}$ dominant. The selection rules $\Delta A = 0, \Delta T = 1$ are observed here to hold, but the $K = K_{max}$ rule is not satisfied. It is hard to call the ${}_2(1, 0)^+$ channel a “dominant channel” since it is almost the same order of amplitude compared to ${}_2(-1, 0)^+$ channel and even smaller at some energies. The four open ${}^1D^e$ channels are shown

in Fig. 4.5 (b). Since the ${}_2(1,0)^+$ channel is dominant, the propensity rule that for each absorption process $\Delta A = 0$, $\Delta T = 1$ and $K = K_{max}$ are all satisfied. Moreover, the partial cross-section decreases with the K quantum number for $N = 2$ channels. This is expected since the largest K channel has the deepest potential at a small hyperradius R (shown in Fig. 4.3), so both the electrons have the largest overlap with the nucleus and therefore be the most probable channel to decaying.

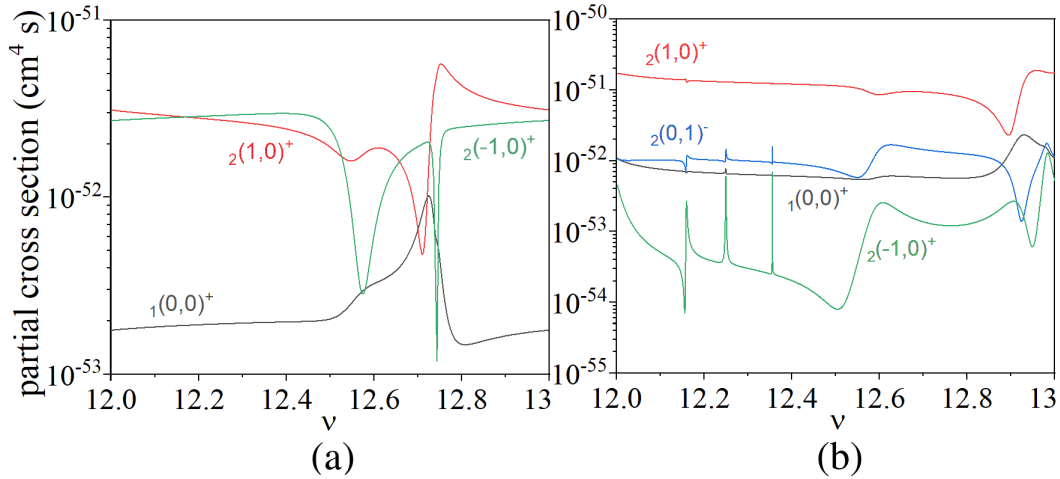


Figure 4.5. The two-photon ionization partial cross sections for (a) ${}^1S^e$ symmetry and (b) ${}^1D^e$ symmetry are shown for each open channel. The effective quantum number ν is relative to $N = 3$ He^+ threshold. The ${}^1S^e$ excited state resonances do obey the same photoabsorption propensity rule that was previously found to hold rather accurately for one-photon absorption processes. This figure is taken from Ref.[58].

An interesting feature in both ${}^1S^e$ and ${}^1D^e$ lineshapes is the overlap of two different resonances, i.e. the ${}_3(2,0)^+$ and ${}_3(-2,0)^+$ resonances for ${}^1S^e$ and ${}_3(2,0)^+$ and ${}_3(0,0)^+$ resonances for ${}^1D^e$. As from $\nu > 4$ the two resonances are already very close, and at some point they overlap, as is shown in Fig.4.9.

The two-photon analysis above indicates that the one-photon propensity rules are roughly satisfied except for $K = K_{max}$. However, the dominant channels from three-photon ionization become even more deviated from the predictions based on the one-photon processes. Fig. 4.6 gives the partial cross-sections for three-photon ionization, which demonstrates that for both ${}^1P^o$ and ${}^1F^o$ symmetry, it is the lowest open channel ${}_1(0,0)^-$ that dominates, and this violates

$\Delta A = 0$ and $\Delta T = 1$. The second prominent channel for ${}^1P^o$ symmetry is ${}_2(0,1)^+$, which echoes with the one-photon propensity rules that have been tested for the ${}^1P^o$ symmetry. However, the second prominent channel for ${}^1F^o$ symmetry is ${}_2(1,0)^-$, which again doesn't obey $\Delta A = 0$ and $\Delta T = 1$. Therefore, the propensity rules for multi-photon ionization are far much weaker than the one-photon situations.

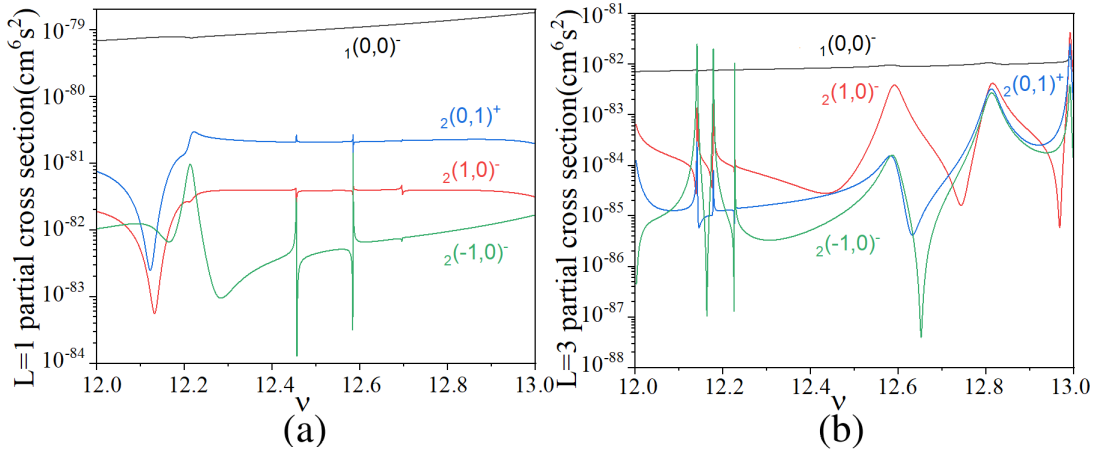


Figure 4.6. The three-photon ionization partial cross sections for (a) ${}^1P^o$ symmetry and (b) ${}^1F^o$ symmetry are shown for each open channel. The effective quantum number ν is relative to $N = 3$ He^+ threshold. The photoabsorption propensity rules for one-photon absorption processes can not be applied to those results. This figure is taken from Ref. [58].

Next, consider the decay process for the autoionization states based on the time-delay matrix analysis. Only two-photon ionization processes are discussed for the decay rules. For ${}^1S^e$ symmetry, three closed channels contribute three resonances in each cycle of ν . The resonance channel correspondences are shown in Fig. 4.7(a). All three resonances are broad ones since they all have $A = +1$. Fig. 4.7(a) plots eigenvalues q of the time-delay matrix which conveys the positions and the decay lifetimes, and (b) plots the decay probability into each open channel. Three open channels can serve as decay routes, namely ${}_1(0,0)^+$, ${}_2(1,0)^+$ and ${}_2(-1,0)^+$, where the vibrational quantum number v is used to delineate those channels. The first thing to note is that the decay probability into the $N = 1$ channel is almost negligible, obeying the propensity rule that $\Delta N = -1$. For ${}_N\{v\}^A = {}_3\{0\}^+$ and

$3\{1\}^+$ resonances, the propensity rule $\Delta A = 0$, $\Delta v = 0$ is satisfied. For the $3\{2\}^+$ resonance, there is no $\Delta v = 0$ continuum, so it decays to the $2\{1\}^+$ channel that has the minimum $|\Delta v|$.

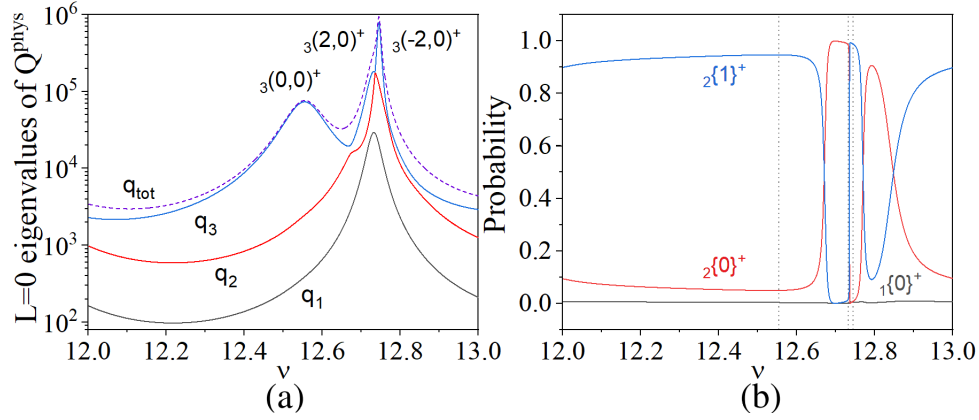


Figure 4.7. Time delay analysis for $1S^e$. The left figure shows the eigenvalues of the time-delay matrix and the right figure shows partial decay probabilities. The dashed lines give the position for the peaks of q_{tot} , which correspond to resonances $N\{v\}^A$ from left to right, $3\{1\}^+$, $3\{0\}^+$, and $3\{2\}^+$. This figure is taken from Ref.[58].

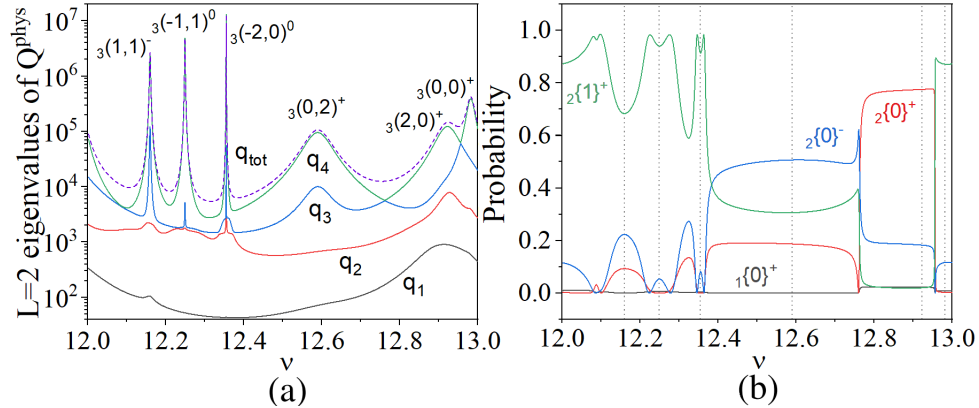


Figure 4.8. Time delay analysis for $1D^e$, as in Fig. 4.7. The $N\{v\}^A$ quantum numbers of the resonances are from left to right, $3\{0\}^-$, $3\{1\}^0$, $3\{2\}^0$, $3\{0\}^+$, $3\{0\}^+$ and $3\{1\}^+$. This figure is taken from Ref.[58].

For $1D^e$ symmetry, there are six closed channels in the range below the $N = 3$ threshold, which gives six resonances in each cycle of ν . Their resonance channel correspondence is given in Fig. 4.8(a) The resonances with $A = +$ are broad ones and the others are narrow, as expected from their potential curves. Their decay probabilities into four open channels

${}_1(0,0)^+, {}_2(1,0)^+, {}_2(0,1)^-$ and ${}_2(-1,0)^+$ are shown in Fig. 4.8(b). The probability of decaying into the $N = 1$ channel is again negligible. However, the other propensity rules are not that obviously satisfied. The propensity rule is observed here to hold only for the most prominent resonance ${}_3(2,0)^+({}_3\{0\}^+)$ and the third prominent resonance ${}_3(0,0)^+$. For the second prominent resonance ${}_3(0,2)^+({}_3\{0\}^+)$, its decay probabilities are 0.51 to ${}_2\{0\}^-$, 0.31 to ${}_2\{1\}^+$ and 0.18 to ${}_2\{0\}^+$, not consistent with the expected propensity rule. It is noted that in this situation both ${}_3(2,0)^+$ and ${}_3(0,2)^+$ have been denoted as $({}_3\{0\}^+)$ channel. Their difference is their T value, and we note that $T = 2$ resonance decays have apparently not been discussed in earlier work. The prominent channel for all three narrow resonances is ${}_2\{1\}^+$. Those narrow resonances are hardly observed in experiments and are not necessarily expected to be governed by the propensity rule.

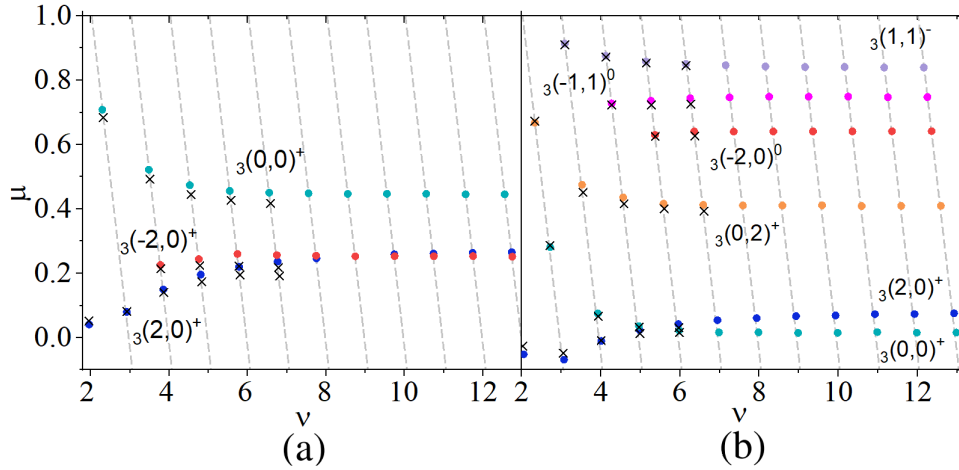


Figure 4.9. The quantum defect μ below $N = 3$ threshold is plotted versus the effective quantum number ν for ${}^1S^e$ (left) and ${}^1D^e$ (right) wave bound states. The black crosses are the truncated diagonalization calculation from [52]. The grey dashed curve has slope -1 and each bound state must lie on one of them because of the QDT condition $\sin \pi(\mu + \nu) = 0$. This figure is taken from Ref.[58].

To test the validity of our calculations, we plot the quantum defect versus the effective quantum number for the ${}^1S^e$ and ${}^1D^e$ symmetry, from the first bound state above $N = 2$ threshold up to $\nu < 13$, as shown in Fig. 4.9. The black crosses are the calculation results from [52], Table VII, based on the truncated diagonalization method. Some calculations from more recent papers[61, 62] are given and compared in Table 3.1 (which is in Chap.3).

For the ${}^1D^e$ wave, the differences in ν are around 0.01 and the agreement is quite good, but for the ${}^1S^e$ wave, the differences are slightly larger, especially as ν increases. The grey dashed lines have slope -1 and connect all the bound states within each ν circle since the bound state energies satisfy $\sin \pi(\mu + \nu) = 0$. Evidently, the ${}^1S^e$ symmetry has all the resonances series present above $\nu \geq 3$, and the ${}^1D^e$ wave from $\nu \geq 5$, since the hyperspherical potentials for some of the channels are rather high lying and repulsive at small hyperradii. In addition, there is a cross-over in the ${}^1S^e$ wave ${}_3(2,0)^+$ and ${}_3(-2,0)^+$ and the ${}^1D^e$ wave ${}_3(2,0)^+$ and ${}_3(0,0)^+$ series, indicating that those resonances are very close to each other and even overlap when those curves across.

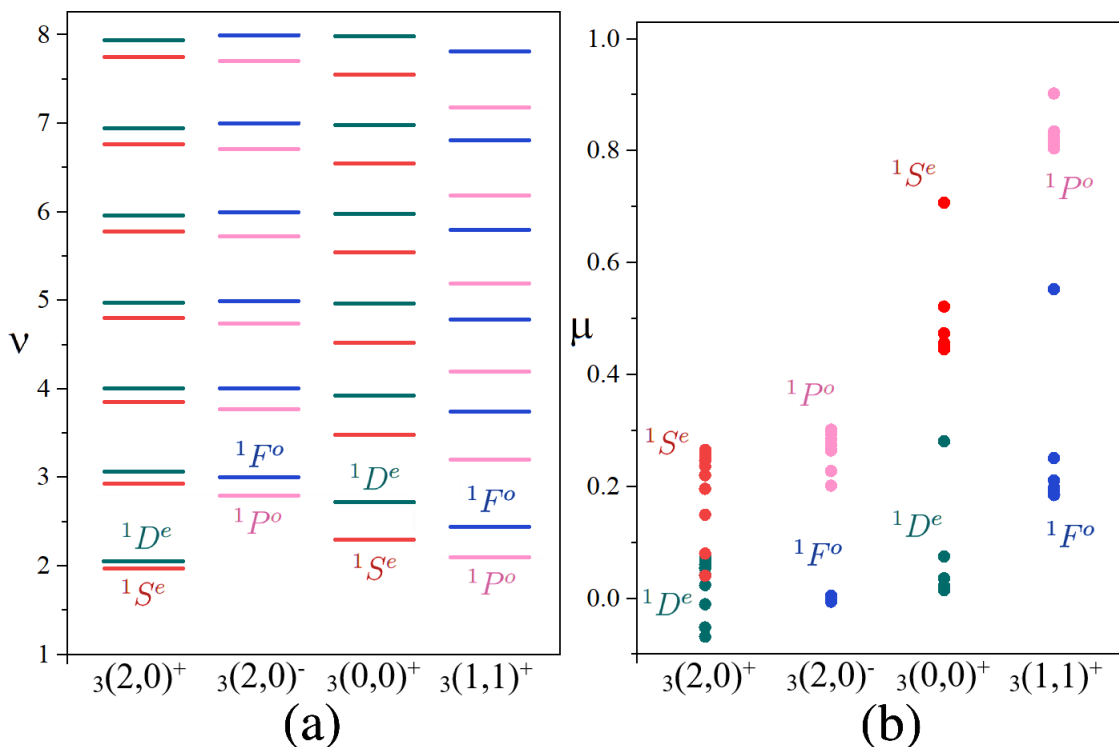


Figure 4.10. The (a) effective quantum numbers and (b) quantum defects for the doubly-excited levels with same ${}_N(K, T)^A$ but different ${}^{2S+1}L^\pi$. In each series of ${}_N(K, T)^A$ states ($A \neq 0$). For each rotor series, the levels with higher L lie slightly higher.

A similar calculation for ${}^1P^o$ and ${}^1F^o$ symmetry at the same range of ν can be found in Fig.3.8. By grouping the energy levels for each ${}_N(K, T)^A$ ($A \neq 0$) with different ${}^{2S+1}L^\pi$, whose diabatic hyperspherical potential curves are quite similar in shape but different by

almost an overall rotational energy, a schematic plot of the rotor series is given in Fig.4.10, as discussed by Ref.[70].

In summary, we explored the photoabsorption processes near the He^+ $N = 3$ threshold. For two-photon processes, one still observes propensity $\Delta A = 0$, $\Delta T = 1$ for each step of excitation, but the rule $K = K_{max}$ is not always satisfied. However, the excitation rules $\Delta A = 0$ and $\Delta T = 1$ are not satisfied for three-photon ionization processes. For autoionization decay, the propensity rule $\Delta N = -1$, $\Delta A = 0$, $\Delta v = 0$ is satisfied only for the most prominent resonances, and for the second prominent resonances in $^1D^e$ wave. When $T = 2$, no clearly dominant decay channel exists.

5. THE ENTANGLED-PHOTON IONIZATION OF ATOMIC HELIUM

In this chapter, we will explore the helium atoms/ions as novel resources of generating entangled photons. Quantum entanglement is a fascinating quantum phenomenon that has no classical analog, which is at the heart of quantum information science, quantum sensing, quantum enhanced imaging and spectroscopy and other emerging quantum technologies. Entanglement of photons has particularly played an important role in many areas of basic and applied research that leverage the quantum advantage[77]. For example, entangled photons have been used in virtual state spectroscopy[78, 79, 80] which goes beyond the time-frequency uncertainty limit[81, 82]; Moreover, a linear (rather than quadratic) scaling of two-photon absorption rate versus intensity is observed with entangled photons[77, 79, 83, 84], which enhances the process at low intensities; Entangled photons as a light source can collectively excite uncoupled atoms [85, 86], and lead to entanglement-induced two-photon transparency [84], which cannot be obtained by a classical laser source.

Typical sources of entangled photons use the process of spontaneous parametric down-conversion (SPDC) in nonlinear crystals in the visible and infra-red region of the spectrum. These sources generate energy-time entangled photons with correlation times on the femtosecond time scale which has been only recently directly measured [87]. SPDC has also been demonstrated in the hard X-ray regime where the correlation times are expected to be attoseconds or smaller [88]. Since SPDC is a non-resonant process, the rate of photon pair creation is low. Some specific technique, such as four-wave mixing techniques involving specific resonances, can generate entangled photons with a high photon count rate, but these photons have specific energies with narrow bandwidth.

Here we propose a method to generate entangled photon pairs in the extreme-ultraviolet (XUV) regime with energy bandwidth large enough to allow correlation times on the attosecond scale, which is based on the spontaneous two-photon emission of the $1s2s\ ^1S_0$ metastable state of helium atom, or its isoelectronic ions and the $2s\ ^2S_{1/2}$ metastable state of helium ion[89, 90, 91, 92, 93]. According to the selection rule, those states can only decays by a two-photon emission process. The emitted photons are energy-time entangled with a cor-

relation time related to the energy spacing between the 2s and 1s levels which is 20.62 eV and 40.81 eV for the helium atom and ion respectively. This large energy bandwidth of the emitted entangled photons corresponds to correlation times in the attosecond domain thus opening up the possibility of attosecond time scale pump-probe experiments using these photons. The main part of this chapter has been included in a paper in preparation, which is in collaboration with Siddhant Pandey, Niranjana Shivaram and Chris H. Greene.

5.1 Gedanken experiment inside a spheroid cavity

In this section, we consider a gedanken experimental set-up in which we have an spheroid cavity, with two helium atoms placed at its two foci. One of the atoms is in $1s2s$ ($^1S^e$) excited state, which is used as an emitter (atom 1), another atom is in $1s^2$ ground state, which is used as an absorber (atom 2), as shown in Fig. 5.1. Atom 1 can only decay into the $1s^2$ state by a simultaneous emission of two-photon, according to the selection rule. Since the long-lived meta-stable $1s2s$ ($^1S^e$) state has a lifetime as long as $\tau = 0.0197$ sec [94], and the energy gap between $1s2s$ ($^1S^e$) and $1s^2$ state are as large as 20.62 eV, the two emitted photons have both a good correlation in frequency, and a narrow window in emission time difference, according to the energy-time uncertainty, therefore are good sources of entanglement (Fig. 5.2). The bi-photons should also be correlated in angular momentum, according to the angular momentum conservation rule. However, we do not address that problem, since inside a spheroid cavity, the entangled photon-pair will be recollected at the absorber with equal-distance optical path, irrespective of their angular distribution or momenta. In treating this process, we assume: 1. The cavity is large enough, that no quantization of photon frequencies or Purcell effect is involved. 2. Both atoms are deeply trapped, that no recoil effects can be observed. 3. The mirror of the cavity is 100% reflective to all the frequencies, that no energy loss occurs during reflection of the photons.

5.1.1 Estimations on correlation time and rate

Inside the cavity, there are three stages of photoelectric processes: the population inversion of atom 1, the spontaneous emission of atom 1, and the photoabsorption of atom 2.

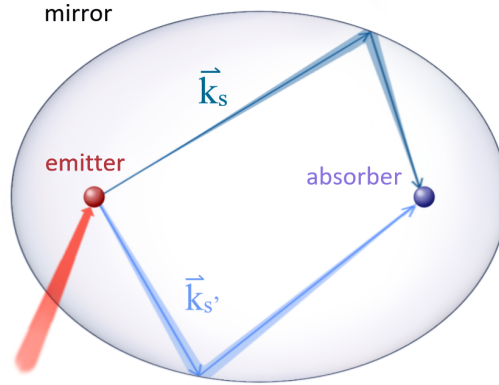


Figure 5.1. A schematic diagram of entangled-photon generation and absorption in a spheroid cavity. The emission and absorption atoms are placed in the two foci of the spheroid, the photons are reflected by the boundary of the cavity, and propagate through equal pathway to reach the absorber. The shape of the cavity will influence the rate of this process, by a geometry factor as discussed in Eq.5.12.

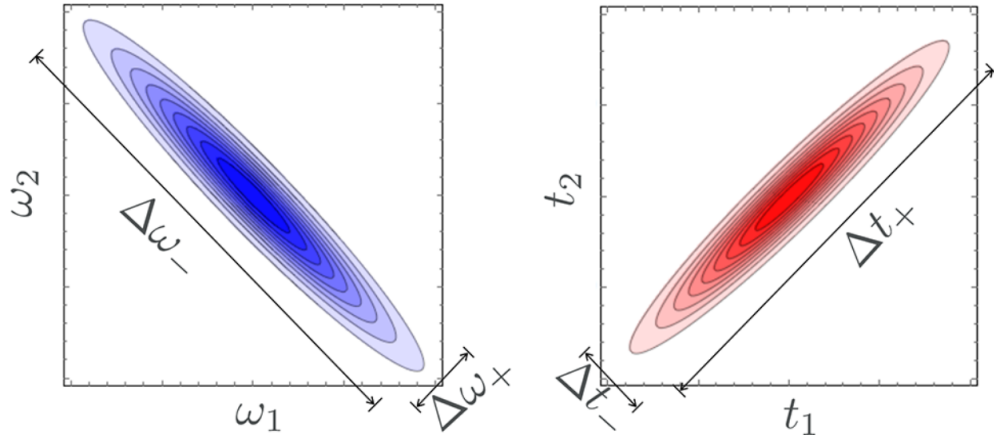


Figure 5.2. Schematic sketch of the absolute value of a typical two-photon wave function in frequency domain and time domain. Recopied from Ref. [79].

In the first stage, we prepare the singlet $1s2s$ state using four photons with each energy is $\hbar\omega_0 = 5.155$ eV . With a monochromatic incident electric field $\mathcal{E}_0 \hat{\epsilon}_0 \cos(\omega_0 t)$, the 4-photon excitation amplitude is,

$$C_{exc}(t) = \left(\frac{e\mathcal{E}_0}{2\hbar}\right)^4 \frac{e^{i(\Delta_{eg}-4\omega_0)t} - 1}{\Delta_{eg} - 4\omega_0} D_{eg}^{(4)} \quad (5.1)$$

$$D_{eg}^{(4)} = \sum_{j_1, j_2, j_3} \frac{\langle e | \hat{\epsilon}_0 \cdot \vec{r} | j_3 \rangle \langle j_3 | \hat{\epsilon}_0 \cdot \vec{r} | j_2 \rangle \langle j_2 | \hat{\epsilon}_0 \cdot \vec{r} | j_1 \rangle \langle j_1 | \hat{\epsilon}_0 \cdot \vec{r} | g \rangle}{(\Delta_{j_3g} - 3\omega_0)(\Delta_{j_2g} - 2\omega_0)(\Delta_{j_1g} - \omega_0)}$$

where $|g\rangle$ is the $1s^2$ ground and the initial state, $|e\rangle$ is the $1s2s$ excited and the final state, $|j_{1,2,3}\rangle$ are the intermediate states. Since

$$\lim_{t \rightarrow \infty} \frac{e^{i(\Delta_{eg}-4\omega_0)t} - 1}{\Delta_{eg} - 4\omega_0} = -\mathcal{P}\left(\frac{1}{\Delta_{eg} - 4\omega_0}\right) + i\pi\delta(\Delta_{eg} - 4\omega_0)$$

The resulting unnormalized state following the excitation, which is also the initial state for the emission process, is: $|\gamma\rangle = i\pi\delta(\Delta_{eg} - 4\omega_0) \left(\frac{e\mathcal{E}_0}{2\hbar}\right)^4 D_{eg}^{(4)} |e\rangle$.

The photon-atom interaction for the second and third stage is:

$$V^{int}(t) = e\vec{r} \cdot \vec{\mathcal{E}}(t) = e\vec{r} \cdot \sum_s i\hat{\epsilon}_s \left(\frac{2\pi\hbar\omega_s}{V}\right)^{\frac{1}{2}} (a_s e^{i(\vec{k}_s \cdot \vec{r} - \omega_s t)} - a_s^\dagger e^{-i(\vec{k}_s \cdot \vec{r} - \omega_s t)}) \quad (5.2)$$

Where \vec{r} is the space vector of the electron, $\vec{\mathcal{E}}$ is the electric field, and V is the quantization volume, the electric field generated by a single photon is proportional to $1/\sqrt{V}$. The photon modes s include the frequency ω_s , propagate direction \hat{k}_s and polarized direction $\hat{\epsilon}_s$. From a second-order perturbation analysis, the amplitude of the emission of two photons ($|\gamma\rangle \otimes |vac\rangle \rightarrow |g\rangle \otimes |1_s, 1_{s'}\rangle$) is,

$$C_{emi}^{(s,s')}(t) = -\frac{2\pi e^2}{V} \sqrt{\omega_s \omega_{s'}} \frac{e^{i(\omega_s + \omega_{s'} - \Delta_{eg})t} - 1}{\omega_s + \omega_{s'} - \Delta_{eg}} \sum_j \frac{\langle g | \hat{\epsilon}_{s'} \cdot \vec{r} | j \rangle \langle j | \hat{\epsilon}_s \cdot \vec{r} | \gamma \rangle}{\hbar(\omega_s - \Delta_{ej})} \quad (5.3a)$$

$$C_{emi}^{(s,s')}(t) = -\frac{2\pi e^2}{V} \sqrt{\omega_s \omega_{s'}} \frac{e^{i(\omega_s + \omega_{s'} - \Delta_{eg})t} - 1}{\omega_s + \omega_{s'} - \Delta_{eg}} \eta(\omega_{s'} - \omega_s) \times \sum_j \langle g | \hat{\epsilon}_{s'} \cdot \vec{r} | j \rangle \langle j | \hat{\epsilon}_s \cdot \vec{r} | \gamma \rangle \left[\frac{1}{\hbar(\omega_s - \Delta_{ej})} + \frac{1}{\hbar(\omega_{s'} - \Delta_{ej})} \right] \quad (5.3b)$$

$|j\rangle$ denotes the intermediate states for the emission process. $\Delta_{ej}(\Delta_{eg})$ is the energy difference between the initial and intermediate (final) atomic state. Eq.5.3a indicates that the photon in mode s is firstly emitted, then photon s' is emitted immediately afterwards. An equivalent expression with the heavy side function $\eta(x) = 1_{x>0}$ is given in Eq.5.3b, which indicates that either photons can be emitted first, but with $\omega_{s'} > \omega_s$. From Eq.5.3b the lifetime of He $1s2s$ (1S_0) can be obtained by,

$$\tau_{1s2s} = \left(\lim_{t \rightarrow \infty} \sum_{s,s'} \frac{d}{dt} |C_{emi}^{(s,s')}(t)|^2 \right)^{-1} \quad (5.4)$$

which gives $\tau_{1s2s} = 0.0197$ sec, and agrees with the experimental value [94].

Since no singlet energy level exists between E_i and $E_i + \Delta_{eg}$ for atom 2, the absorption process can only start after both photons have been emitted, with $\omega_s + \omega_{s'} = \Delta_{eg}$. The modes of the photons are not detectable inside the cavity, therefore the “entangled photon state” can be obtained by summing over all the modes (s, s') [95]:

$$|2ph\rangle = \sum_{s,s'} C_{emi}^{(s,s')}(t \rightarrow \infty) |1_s, 1_{s'}\rangle \quad (5.5)$$

Based on a second-order perturbation calculation, The entangled-photon absorption amplitude can be written as,

$$C_{abs}(t) = -\frac{e^2}{\hbar^2} \int_0^t dt_2 \int_{-\infty}^{t_2} dt_1 \sum_m e^{i(\Delta_{mi}t_1 + \Delta_{fm}t_2)} \times (\langle f| \otimes \langle vac|) \vec{r} \cdot \vec{\mathcal{E}}(t_2) |m\rangle \langle m| \vec{r} \cdot \vec{\mathcal{E}}(t_1) (|i\rangle \otimes |2ph\rangle) \quad (5.6)$$

$|i\rangle$, $|m\rangle$ and $|f\rangle$ denotes the initial, intermediate, and final states for atom 2. $\vec{\mathcal{E}}(t_{1,2})$ are the electric fields of the photons that are bounced back by the cavity (whose frequencies stay the same but propagation and polarization directions have changed), being absorbed at time t_1 and t_2 . The evaluation of Eq. 5.6 depends on the shape of the cavity, and it turns out that

the absorption process can be described by a rank-0 tensor, which is discussed in the next subsection.

$$\begin{aligned}
C_{abs}(t) &= -\frac{e^2}{\hbar^2} \int_0^t dt_2 \int_{-\infty}^{t_2} dt_1 \langle vac | \vec{\mathcal{E}}(t_2) \cdot \vec{\mathcal{E}}(t_1) | 2ph \rangle \frac{1}{3} \sum_m \langle f|r|m \rangle \langle m|r|i \rangle e^{i(\Delta_{mi}t_1 + \Delta_{fm}t_2)} \\
&= \frac{\Theta e^8 \mathcal{E}_0^4}{256 \hbar^4 c^6} D_{eg}^{(4)} \delta(\Delta_{eg} - 4\omega_0) \frac{e^{i(\Delta_{fi} - \Delta_{eg})t} - 1}{\Delta_{fi} - \Delta_{eg}} \int_0^{\Delta_{eg}} d\omega_s [\omega_s (\Delta_{eg} - \omega_s)]^3 \sum_m \frac{\langle f|r|m \rangle \langle m|r|i \rangle}{\hbar(\omega_s - \Delta_{mi})} \\
&\quad \times \sum_j \left(\frac{\langle g|r|j \rangle \langle j|r|e \rangle}{\hbar(\omega_s - \Delta_{ej})} + \frac{\langle g|r|j \rangle \langle j|r|e \rangle}{\hbar(\Delta_{jg} - \omega_s)} \right)
\end{aligned} \tag{5.7}$$

Θ is a geometry factor which is introduced in Eq. 5.12, whose values are shown in Figure 5.4. Especially, for a spherical cavity, $\Theta = \frac{64\pi^2}{27}$.

According to the time-energy uncertainty, the emission-time difference of the photon pair could be estimated by $2\pi/\Delta_{eg} \sim 8.34 \text{ a.u.}$ which is $2.02 \times 10^{-16} \text{ sec.}$ The time correlation of the entangled photon pair can be found from $\langle vac | \mathcal{E}(t_2) \mathcal{E}(t_1) | 2ph \rangle$, which is proportional to the fourier transformation of the spectrum [83, 84, 96], as

$$\begin{aligned}
\langle vac | \mathcal{E}(t_2) \mathcal{E}(t_1) | 2ph \rangle &\propto e^{-i\Delta_{eg}t_2} \int_0^{\Delta_{eg}} d\omega_1 e^{i\omega_1(t_2-t_1)} [\omega_1 (\Delta_{eg} - \omega_1)]^3 \\
&\quad \times \sum_j \left[\frac{\langle g|r|j \rangle \langle j|r|e \rangle}{\hbar(\omega_1 - \Delta_{ej})} + \frac{\langle g|r|j \rangle \langle j|r|e \rangle}{\hbar(\Delta_{jg} - \omega_1)} \right]
\end{aligned} \tag{5.8}$$

The first and second term in the square bracket corresponds to the firstly emitted photon being absorbed at time t_1 and t_2 , respectively. The right hand side of Eq. 5.8 is plotted in Fig. 5.3(a), versus the time difference between two absorption events of the two photons. The time scale between the two absorption events is around $\pm 4 \text{ a.u.}$ which gives a correlation time[81] around $1.93 \times 10^{-16} \text{ sec.}$

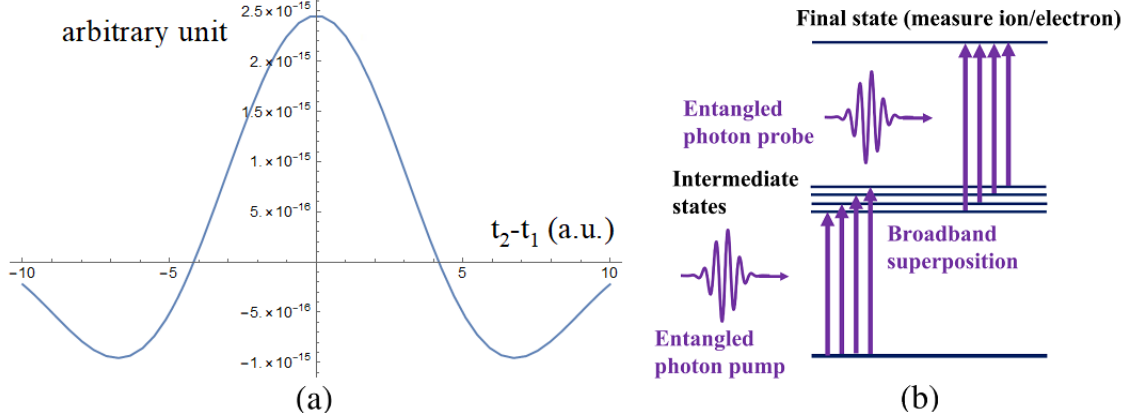


Figure 5.3. (a) The photon correlation function $\langle vac|E(t_2)E(t_1)|2ph\rangle$ (up to a constant factor) as a function of time difference ($t_2 - t_1$), which indicates the correlation time is around 1.93×10^{-16} sec. (b) An attosecond pump-probe photoionization scheme using entangled bi-photons.

Finally, according to Eq.5.1, 5.3 and 5.6, the rate for the excitation, emission and absorption where an entangled photon-pair is transferred coherently, is:

$$\begin{aligned}
 R_{trans} &= 2\pi\delta(\Delta_{fi} - \Delta_{eg}) \left| \frac{\Theta e^8 \mathcal{E}_0^4}{256 \hbar^6 c^6} D_{eg}^{(4)} \delta(\Delta_{eg} - 4\omega_0) \int d\omega_s [\omega_s (\Delta_{eg} - \omega_s)]^3 \sum_m \frac{\langle f|r|m\rangle \langle m|r|i\rangle}{\omega_s - \Delta_{mi}} \right. \\
 &\times \left. \sum_j \left(\frac{\langle g|r|j\rangle \langle j|r|e\rangle}{\omega_s - \Delta_{ej}} + \frac{\langle g|r|j\rangle \langle j|r|e\rangle}{\Delta_{jg} - \omega_s} \right) \right|^2
 \end{aligned} \tag{5.9}$$

For a spherical cavity, $R_{trans} = 1.91 \times 10^{-25} \mathcal{E}_0^8$ a.u.. The input beam flux is $J = \frac{c\mathcal{E}_0^2}{8\pi\hbar\omega_0}$. It turns out the transition rate is proportional to J^4 . The entangled-photon absorption rate is known to be proportional to the beam intensity (when the beam intensity is not very strong) [77, 78, 84], and our result can be regarded as a generalization of this linearity. Since our excitation process is a four-photon process, we can consider the four-photon flux as a whole, which is the input of the system, $J^{(4)} = J^4$. Therefore it is an expected outcome that $R_{trans} \propto J^{(4)}$.

In Sec.5.2 we will follow the estimation here and discuss the experimental applicability of this spontaneously emitted entangled-photon scheme, and propose experimental setups that can be achieved by our collaborators.

5.1.2 Geometry of the cavity

In this subsection, we will discuss the influence of the cavity geometry on the photoabsorption process, and evaluate the geometry factor Θ introduced in Eq. 5.9. We start with summing over all the optical modes, to obtain an entangled-photon state:

$$\sum_{s,s'} = \frac{V^2}{(2\pi c)^6} \int \omega_s^2 \omega_{s'}^2 d\omega_s d\omega_{s'} d\Omega_{k_s} d\Omega_{k_{s'}} \sum_{\hat{e}_{s,s'}(\perp \hat{k}_{s,s'})} \quad (5.10)$$

where $\int d\Omega_{k_s} = \int \sin \theta_s d\theta_s d\phi_s$ integrates over the emission angle, and $\sum_{\hat{e}_{s,s'}(\perp \hat{k}_{s,s'})}$ sums the polarization vector basis. In a spherical cavity, the photon propagation vector is usually chosen to be (the mode index s and s' for the two photons are neglected when we discuss only a single photon),

$$\hat{k} = (\sin \theta \cos \phi, \sin \theta \sin \phi, \cos \theta)$$

When the photon is bounced back, its propagation vector becomes $\hat{k}' = -\hat{k}$. The polarization vectors which are perpendicular to \vec{k} can be expanded into two basis,

$$\begin{cases} \hat{e}^{(1)} = (-\sin \phi, \cos \phi, 0) \\ \hat{e}^{(2)} = (-\cos \theta \cos \phi, -\cos \theta \sin \phi, \sin \theta) \end{cases}$$

However, in a spheroid cavity we need to reparametrize everything above. We assume the spheroid cavity has one major axis length $2a$ and two minor axes length $2b$ ($a \geq b$), the two foci are aligned along the major axis of the spheroid (which is the \hat{z} axis), and the distance between them is $2l$ ($l = \sqrt{a^2 - b^2}$). The photon is emitted from one focus, and no

matter what direction it propagates, it bounces back and passes through the other focus. The propagation vector before and after the reflection can be parameterized as:

$$\begin{aligned}\hat{k} &= \frac{1}{L_+}(b \sin \tilde{\theta} \cos \tilde{\phi}, b \sin \tilde{\theta} \sin \tilde{\phi}, l + a \cos \tilde{\theta}) \\ \hat{k}' &= \frac{1}{L_-}(-b \sin \tilde{\theta} \cos \tilde{\phi}, -b \sin \tilde{\theta} \sin \tilde{\phi}, -l + a \cos \tilde{\theta})\end{aligned}$$

where $L_{\pm} = \sqrt{b^2 \sin^2 \tilde{\theta} + (l \pm a \cos \tilde{\theta})^2}$. The polarization basis for \vec{k} and \vec{k}' are,

$$\begin{cases} \hat{\epsilon}^{(1)} = (-\sin \tilde{\phi}, \cos \tilde{\phi}, 0) \\ \hat{\epsilon}^{(2)} = \frac{-1}{L_+}[(l + a \cos \tilde{\theta}) \cos \tilde{\phi}, (l + a \cos \tilde{\theta}) \sin \tilde{\phi}, -b \sin \tilde{\theta}] \end{cases}$$

$$\begin{cases} \hat{\epsilon}^{(1)'} = (-\sin \tilde{\phi}, \cos \tilde{\phi}, 0) \\ \hat{\epsilon}^{(2)'} = \frac{1}{L_-}[(-l + a \cos \tilde{\theta}) \cos \tilde{\phi}, (-l + a \cos \tilde{\theta}) \sin \tilde{\phi}, -b \sin \tilde{\theta}] \end{cases}$$

$\hat{\epsilon}^{(1)}$ is perpendicular to the incident plane and doesn't change upon reflection, but $\hat{\epsilon}^{(2)}$ does: $\hat{\epsilon}^{(2)(\prime)} = \hat{k}^{(\prime)} \times \hat{\epsilon}^{(1)(\prime)}$. The angular integral is,

$$\begin{aligned}\int d\Omega_k &= \int \sin \theta d\theta d\phi \\ &= \int \left[\frac{a}{L_+} - \frac{l(l + a \cos \tilde{\theta})(a + l \cos \tilde{\theta})}{L_+^3} \right] \sin \tilde{\theta} d\tilde{\theta} d\tilde{\phi}\end{aligned}\tag{5.11}$$

We now consider the photon pair in modes s and s' , their propagation directions are random and independent with each other. However, constraints are set on their polarization directions. In the spontaneous decay from $e = 1s2s$ ($^1S^e$) to $g = 1s^2$ state, only the isotropic part of the dipole operator can survive:

$$\langle g | \hat{\epsilon}_{s'} \cdot \vec{r} | j \rangle \langle j | \hat{\epsilon}_s \cdot \vec{r} | e \rangle = \frac{\hat{\epsilon}_s \cdot \hat{\epsilon}_{s'}}{3} \langle g | r | j \rangle \langle j | r | e \rangle$$

In the absorption process, since the photons are not detectable inside the cavity, all the angular directions are integrated coherently:

$$\begin{aligned}
& \sum_{i,j=1,2} \int d\Omega_{k_s} d\Omega_{k_{s'}} \frac{\hat{\epsilon}_s^{(i)} \cdot \hat{\epsilon}_{s'}^{(j)}}{3} (\hat{\epsilon}_s^{(i)'} \cdot \vec{r}_1) (\hat{\epsilon}_{s'}^{(j)'} \cdot \vec{r}_2) \\
&= \sum_{i,j=1,2} \sum_{k\mu} \frac{(-1)^{1+k+\mu}}{\sqrt{3}} [\vec{r}_1 \vec{r}_2]_{-\mu}^{(k)} \\
&\times \int d\Omega_{k_s} d\Omega_{k_{s'}} [\hat{\epsilon}_s^{(i)'} \hat{\epsilon}_{s'}^{(j)'}]_{\mu}^{(k)} [\hat{\epsilon}_s^{(i)} \hat{\epsilon}_{s'}^{(j)}]_0^{(0)} \\
&= \sum_{i,j=1,2} \int d\Omega_{k_s} d\Omega_{k_{s'}} \frac{1}{9} (\hat{\epsilon}_s^{(i)} \cdot \hat{\epsilon}_{s'}^{(j)}) (\hat{\epsilon}_s^{(i)'} \cdot \hat{\epsilon}_{s'}^{(j)'}) (\vec{r}_1 \cdot \vec{r}_2) \\
&= \Theta \vec{r}_1 \cdot \vec{r}_2
\end{aligned} \tag{5.12}$$

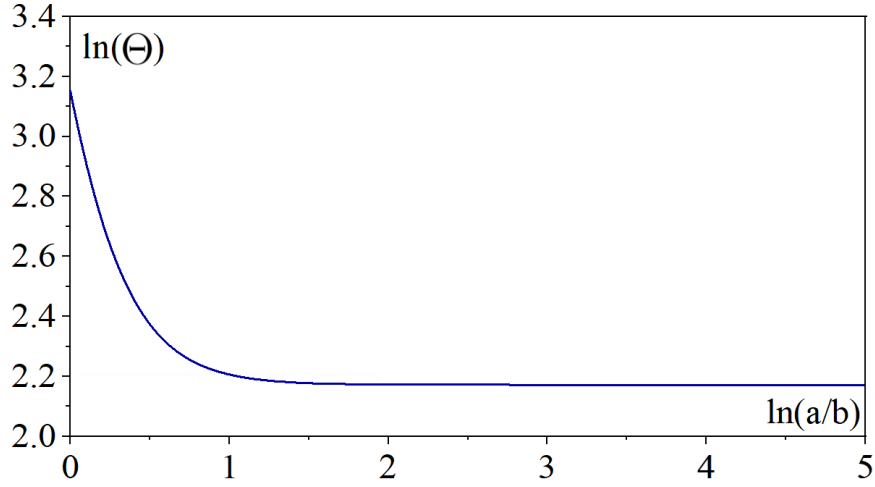


Figure 5.4. A plot of geometry parameter Θ versus the aspect ratio a/b in an log-log scale. When $a = b$, the cavity is a sphere and the geometry parameter obtained its maximum $\Theta = \frac{64\pi^2}{27}$.

Where $[\dots]_{\mu}^{(k)}$ is an rank- k spherical tensor with component μ ($|\mu| \leq k$), as a result of the tensor product of two vectors[46]. Given the emitted-photon tensor have only rank-0 component, from the orthogonality of spherical tensors, we have $k = 0, \mu = 0$. So only rank-0 transition is allowed in the absorption process. This conclusion will no longer hold once the directions of the photons can be detected, i.e., by a recoil effect of the atoms. The geometry factor Θ is introduced to denote the polarization part of the integration. When

the cavity is a perfect sphere, Eq.5.12 gives $\Theta = \frac{64\pi^2}{27}$. The change of Θ versus the aspect ratio of the cavity can be found in Figure 5.4, from the range of $a = b$ to $a = 148b$. As the cavity becomes prolate spheroid shaped, Θ decrease with the aspect ratio a/b , and become stable at around $\Theta = \frac{8\pi^2}{9}$.

5.2 Experimental set-up and outlooks

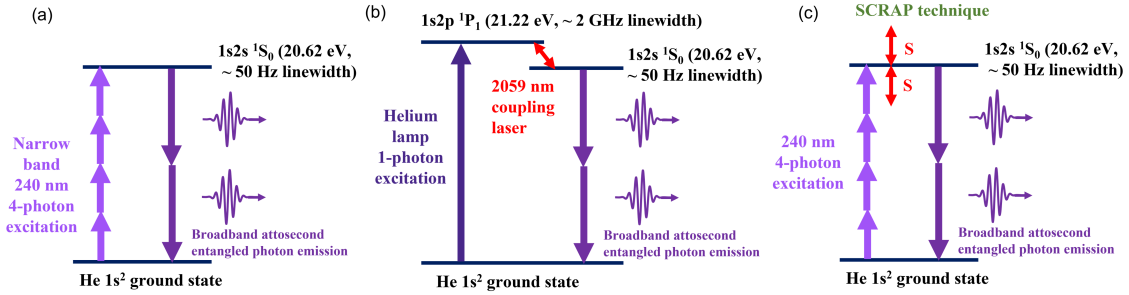


Figure 5.5. Generation of entangled bi-photons in the XUV via two-photon decay of the $1s2s \ ^1S_0$ state excited by: (a) 4-photon excitation using a narrow band 240 nm laser. (b) Two-step sequential excitation via the $1s2p$ state using a high photon flux helium lamp and a 2059 nm coupling laser. (c) The SCRAP technique using a multiphoton pump pulse and a Stark shifting pulse which enable rapid adiabatic passage.

After an estimation of the excitation rate for the Gedanken experiment, in this section, we turn to consider its applicable and possible experimental set-up. The calculations in the last section assumes a direct multi-photon excitation from ground state $1s^2$ to singlet state $1s2s$. Since the $1s2s$ metastable state has a narrow linewidth of ~ 50 Hz, a multi-photon excitation to this state requires intense lasers with a linewidth smaller than 50 Hz at a wavelength of ~ 240 nm. While excitations of multiphoton metastable states with narrow linewidth lasers have been previously demonstrated [97], achieving a significant fraction of metastable atoms with a 240 nm laser is currently challenging. An alternative scheme using a lambda-type transition between $1s^2$, $1s2p$, and $1s2s$ states could be used to achieve significant excitation. The energy levels of the latter two are 21.22 eV and 20.62 eV above the ground state, respectively. Ideally, by Stimulated Raman Adiabatic Passage (STIRAP) [98] one could achieve nearly 100% population inversion onto the $1s2s$ state. In this system,

we consider using the Stokes pulse to dress the single-photon transition between $1s2p$ and $1s2s$, while the pump pulse excites the atom from $1s^2$ to $1s2p$ state. Since the $1s2s$ and $1s2p$ states are quite close to the $N = 2$ continuum threshold (24.59 eV above the ground state), to prevent ionization leakage which will deteriorate the STIRAP process, the pumping process from $1s^2$ to $1s2p$ should be at least a seven-photon excitation, making this STIRAP scheme not very efficient and applicable [99, 100].

Accordingly, a two-step sequential excitation appears more promising, to first excite $1s^2 \rightarrow 1s2p$ and then $1s2p \rightarrow 1s2s$. The oscillator strengths for one-photon excitation processes are $f_{a \rightarrow b} = 2\Delta_{ba} |\langle b | \hat{\epsilon}_0 \cdot \vec{r} | a \rangle|^2$, which gives $f_{1s^2 \rightarrow 1s2p} = 0.2826$ and $f_{1s2p \rightarrow 1s2s} = -0.3633$ for the two steps. The first step can also be achieved by a 5-photon nonsequential excitation, with each photon 4.24 eV, the generalized cross-section gives,

$$\sigma_{1s^2 \rightarrow 1s2p} = 2\pi(2\pi\omega\alpha)^5 |D^{(5)}|^2 = 5.8519 \times 10^{-4} a.u.$$

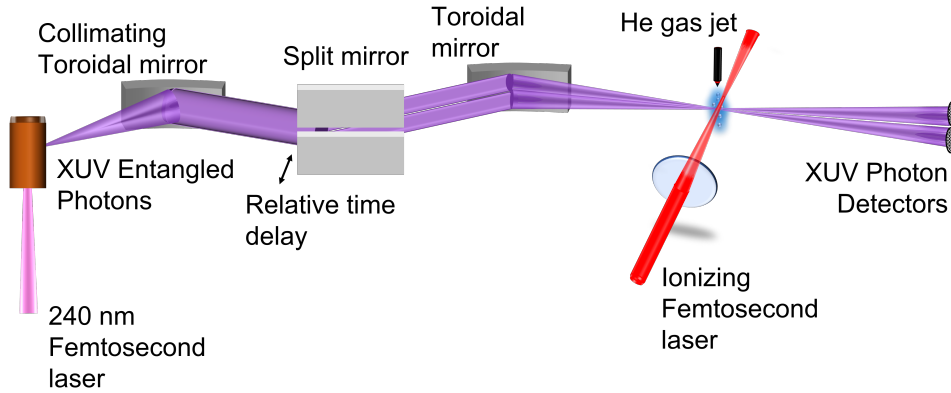


Figure 5.6. Proposed experimental scheme to generate XUV entangled photons as described in 5.5 and measure their correlation time. The emitted entangled bi-photons are collected within a large solid angle in a direction orthogonal to the excitation laser propagation direction. The bi-photons are collimated by a toroidal mirror and then split into two independently time delayed paths before being focused by a second toroidal mirror at a target gas jet in a vacuum chamber. Entangled two-photon absorption in helium can be measured as a function of time delay using photon detectors or by collecting helium ions after ionization by a high repetition rate femtosecond laser.

To achieve the described two-step sequential excitation above, a high photon flux helium lamp source can be used in the first step to excite $1s2p$ and a 2059 nm laser can transfer population to the $1s2s$ state. The ~ 1 GHz linewidth of the $1s2p$ state eliminates the need for a narrow linewidth laser.

Another alternative approach to achieve significant population of the $1s2s$ singlet metastable state is to use Stark-chirped rapid adiabatic passage (SCRAP) previously proposed to excite the $2s$ metastable state in a hydrogen atom [101]. In this technique, a pump pulse excites the metastable state via a multiphoton transition in the presence of a Stark pulse that Stark shifts the $1s2s$ state (see figure 5.5 (c)). The combined effect of the two pulses results in a Landau-Zener-type adiabatic passage that can significantly populate the $1s2s$ state. The SCRAP technique can also suppress ionization leakage by laser-induced continuum structure [102].

The bi-photons from the decay of the $1s2s$ state are emitted in all directions with an approximate distribution given by $(1 + \cos^2 \theta)$ [93], where θ is the relative angle between the entangled photons. The photons that are emitted in a direction orthogonal to the excitation laser propagation direction can be collected within a large solid angle and sent along independent time-delayed paths towards a pump-probe target. Figure 5.6 shows a schematic of a proposed experimental setup for generation of these entangled photons and their utilization in an attosecond pump-probe experiment. In this scheme, a grazing incidence toroidal mirror collimates the emitted photons which are then split into two halves using a grazing incidence split mirror that can introduce a controllable time-delay between the two halves of the beam. The split beams are then focused using a second toroidal mirror onto the target gas jet. A pump-probe experiment with attosecond time resolution can be performed by measuring a photo-ion or photo-electron signal arising from the absorption of entangled bi-photons by an atom or molecule. Recent work on entangled two-photon absorption sets upper bounds on the enhancements in two-photon absorption cross section with entangled photons when no intermediate resonances are involved [103, 104]. When intermediate resonances are involved, the two-photon absorption rate is significantly enhanced. Further, measuring a pump-probe photoionization signal as opposed to an absorption signal as in previous two-photon absorption experiments allows detection of low absorption rates. Such

entangled photon pump-probe experiments will extend the capabilities of attosecond science where attosecond pulses are currently used from high-order harmonic generation [105] or free electron laser [106] sources.

The entangled photon generation scheme discussed here can be extended to the soft X-ray (SXR) regime using helium-like ions. Two-photon decay in helium-like ions has been well studied [89, 91, 93]. Similar to the $1s2s\ ^1S_0$ state of neutral helium atoms, the $1s2s\ ^1S_0$ states of helium-like ions such as N^{5+} , O^{6+} and Ne^{8+} , predominantly decay by two-photon emission with a rate proportional to Z^6 , where Z is the atomic number. The large energy difference between such excited states and the ground state of the ions, which can be in the range of several hundred to thousands of electron-volts, results in entangled photon correlation times of few attoseconds to zeptoseconds. For example, the $1s2s\ ^1S$ state of Ne^{8+} is located ~ 915 eV above the Ne^{8+} ground state and this corresponds to an entangled photon correlation time of ~ 5 attoseconds. The two-photon decay rate in this case is $\sim 1 \times 10^7\ s^{-1}$ which is significantly larger than the corresponding rate for neutral helium atoms of $\sim 5 \times 10^1\ s^{-1}$. Ne^{8+} has been previously generated using strong femtosecond laser fields [] as well as using strong femtosecond X-ray pulses from free electron lasers [107] both of which can potentially also create Ne^{8+} in the $1s2s\ ^1S_0$ excited state. We note here that it has been previously experimentally demonstrated that the bandwidth required to generate few-attosecond pulses can be obtained from HHG using mid-infrared pulses [108]. Further, it has been theoretically shown that zeptosecond pulses can be generated from HHG when suitable filters are used [109]. However, the shortest measured attosecond pulse is currently 43 attoseconds [105]. Our approach of using entangled photons from two-photon decay of helium-like ions offers an alternative path for carrying out ultrafast measurements in these extreme regimes of a few-attoseconds or zeptoseconds.

In conclusion, an unconventional approach is presented here for generating attosecond entangled bi-photons in the XUV and SXR regimes using two-photon decay in helium atoms and helium-like ions. Multiple alternative schemes can be used to excite the $1s2s\ ^1S_0$ metastable state in helium and experimental scheme is suggested to collect and use the emitted XUV bi-photons in an attosecond pump-probe experiment. Potential extension of such metastable excitations to helium-like ions is additionally proposed, whereby SXR bi-

photons can be generated with entanglement times in the few-attosecond range with the possibility of reaching the zeptosecond regime. This approach can open doors to using XUV/SXR entangled photons in quantum imaging and attosecond quantum spectroscopy of atomic, molecular and solid-state systems.

6. SINGLE-CHANNEL COHERENT CONTROL OF ATOMIC HELIUM

Coherent control scenarios have generated extensive attention in condensed matter systems and atomic and molecular physics. The basic idea is to introduce a difference in two alternative electric dipole transition amplitudes to manipulate the interference between them and thereby control an observable outcome. In particular, phase-sensitive coherently controlled quantum interference enables the observation of novel physics. For example, the two-color phase-sensitive coherent control can be applied to various scenarios in physical chemistry and molecular physics in order to control the branching ratio among different reaction products [110, 111, 112], to rotate the molecular polarization, and to selectively ionize oriented molecules [113]. In condensed matter physics it is primarily of interest to control the current flow direction in a semiconductor [114, 115], and in quantum computation to depress the linkage error of qubits [116]. This technique is also used in femtosecond and attosecond experiments [117] and in the strong field regime [118], and to achieve quantum path control between short and long electron trajectories [119].

Compared with the extensive experimental literature, there are comparatively few theoretical calculations that provide a full treatment of such coherently controlled systems [45]. Several calculations have been carried out for photoionization of Ne [120, 121], H₂ [122], and dc-field dressed hydrogen and alkali-metal atoms in a limited energy range [123, 124].

In this and the following chapter, we will study the coherent control of helium and barium ionization, respectively (Those studies have been published in Ref.[125] and [64]). The energy level diagrams are given in Fig.6.1 and 7.1, the former one is an example of single-channel coherent control, while the latter one is for multi-channel coherent control. In both cases, the photoelectron angular distribution (PAD) is computed to analyze the phase dependence of the directional right-left (or upper-lower) asymmetry parameter, especially as influenced by Fano-Feshbach resonances, and the role of autoionizing states in affecting the interference between one- and two-photon ionization pathways. Especially, for the single-channel coherent control discussed in this chapter, we optimized both the relative phase and amplitudes of laser fields and proposed a new frequency-sensitive controlling scheme, by

which a small energy change near resonances can flip the direction of scattering electrons with high efficiency. An example of the frequency-sensitive coherent control where 90% of the photoelectrons flip their emission direction is presented. The main part of this chapter has been included in Ref.[125], which is coauthored with Chris H. Greene.

6.1 Theoretical description of single channel coherent control

The present study treats the $\omega - 2\omega$ coherent control of helium ionization, an atom for which the electron correlations have been extensively calculated and interpreted [5, 62, 75, 126, 127, 128]. In contrast to the studies of the coherent control of photoelectron branching ratios into multiple open channels [37, 39, 129, 130] (which will be discussed in the next chapter), the present treatment considers ionization into a single open channel that possesses, however, three contributing partial waves. The bichromatic laser electric field considered in our treatment is given by $\vec{\mathcal{E}}(t)$:

$$\vec{\mathcal{E}}(t) = \hat{\epsilon} \left(\mathcal{E}_{2\omega} e^{-i(2\omega t + \Phi_{2\omega})} + \mathcal{E}_{\omega} e^{-i(\omega t + \Phi_{\omega})} + c.c. \right). \quad (6.1)$$

Here $\mathcal{E}_{\omega, 2\omega}$ are the electric field amplitudes for the fundamental and second harmonic. The two fields have a variable but well-defined phase relation, denoted by $\Phi_{\omega, 2\omega}$, and both of the fields are chosen here to be linear-polarized along a common z -axis *i.e.*, $\hat{\epsilon} = \hat{z}$. The frequency range considered is $\omega = 1.0 - 1.2$ *a.u.*. The schematic diagram of the ionization process is shown in Fig. 6.1. A ground state He atom at $E_g = -2.90$ *a.u.* absorbs either one photon with energy 2ω or two photons with each energy ω , reaching a final state f with energy from -0.9 to -0.5 *a.u.* (indicated by the upper shaded region of Fig. 6.1). The two-photon pathway is an above threshold ionization (ATI), with intermediate energies given by the lower shaded region of Fig.6.1. The resonances converging to the $N = 2$ threshold are of particular interest. The atomic orbital angular momentum is initially $L_i = 0$, and it changes after absorption of one electric dipole photon to $L_f = 1$, or after two-photon absorption to $L_f = 0, 2$. The parity π flips between even and odd for each photon absorption step, and the atomic spin S remains in the singlet state since spin-spin and spin-orbit interactions are neglected in this study.

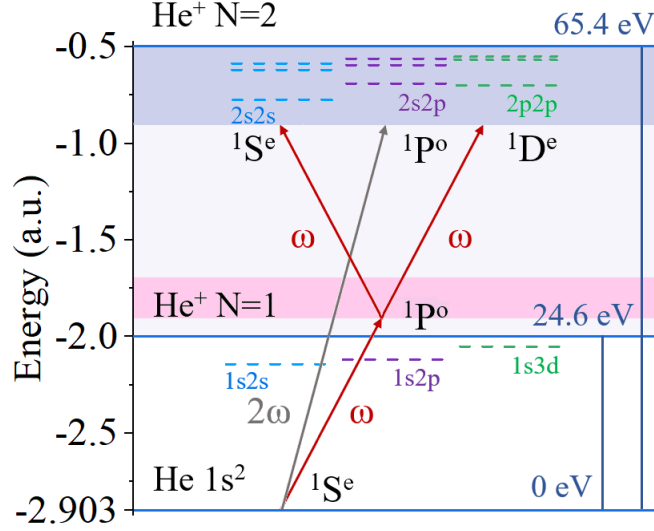


Figure 6.1. Schematic energy level diagram of helium for the relevant transitions. The He ground state is ionized, with the one and two-photoionization pathways indicated by arrows. The shaded regions show the energy ranges considered for the final and intermediate states, both of which are between the $N = 1$ and $N = 2$ thresholds. The dashed lines give the lowest few bound and autoionizing energy levels[5] below the $N = 1$ and $N = 2$ thresholds, respectively, with $^{2S+1}L^\pi$ spectroscopic labels from left to right as $^1S^e$, $^1P^o$ and $^1D^e$. The autoionization levels that are relevant to our calculations are those above the $N = 1$ thresholds. There are no intermediate-state resonances involved in the frequency range considered, only an open ionization continuum. This figure is taken from Ref.[125].

It is well known that the $\omega - 2\omega$ scheme displays no interference effects that can influence the total yield [131]. This is because the even- and odd-parity final states are in principle distinguishable, which implies that no interference occurs in any observable that commutes with the parity operator such as the integrated absorption rate. However, the $\omega - 2\omega$ scheme influences the angular emission of the photoelectron, since an angular observable represents an operator that does not commute with parity. This interference has been confirmed by experiments [37, 38, 39, 131], which show that tuning the phase difference $\Delta\Phi = 2\Phi_\omega - \Phi_{2\omega}$ causes a sinusoidal modulation that can be observed in the integrated lower- or upper- (negative or positive z) dominance in the photoejection directions. The remainder of this article shows the sinusoidal modulation in the computed photoelectron angular distribution $\frac{dW(\theta)}{d\Omega}$.

$$\frac{dW(\theta)}{d\Omega} = \left| c_0 Y_{00}(\theta) e^{i\phi_0} + c_1 Y_{10}(\theta) e^{i(\phi_1 + \Delta\Phi)} + c_2 Y_{20}(\theta) e^{i\phi_2} \right|^2 = \frac{W_{\text{tot}}}{4\pi} \sum_{j=0}^4 \beta_j P_j(\cos\theta) \quad (6.2)$$

Here θ is the polar angle between the ejected electron and the polarization axis; there is no ϕ dependence owing to the azimuthal symmetry. W_{tot} is the angle-integrated transition rate and $\beta_0 \equiv 1$. In the first line of Eq. 6.2, the differential transition rate $\frac{dW(\theta)}{d\Omega}$ is given by a coherent sum of the different angular components, with complex transition amplitude $c_l e^{i\phi_l}$ for partial wave l , where c_l is real and positive. Since a photoelectron in our calculation can escape only with He⁺ in the 1s state, its angular momentum takes the values $l = L_f = 0, 1, 2$. The experimentally-controllable optical phase is $\Delta\Phi = 2\Phi_\omega - \Phi_{2\omega}$, which is distinct from the intrinsic phases in the amplitudes ϕ_l that reflect the atomic physics. Note that the latter are strongly energy dependent near resonances and thresholds: they include contributions from the long-range Coulomb potential, the electron correlations, and the intermediate scattering states.

The second line of Eq. 6.2 rearranges the summed products of spherical harmonics $Y_{l0}(\theta)$ into Legendre polynomials $P_j(\cos\theta)$ with real coefficients β_j . The even (odd) order $P_j(\cos\theta)$ gives the symmetric (anti-symmetric) photoelectron distribution along $\theta = \pi/2$ which produce differences between the lower- and upper halves of the emission sphere, i.e., the negative and positive z regions, respectively. In the absence of interference, the odd orders of $P_j(\cos\theta)$ would vanish and no asymmetry would be observed between the two hemispheres. With some specific values of β_j , it is possible to guide most electrons to one side, as we will demonstrate in the latter discussion. A directional asymmetry parameter $\alpha_L = W_L/(W_L + W_U)$ has been measured in some experiments[37, 38, 39, 131], so we use it to quantify the ratio between the lower-directed electron current and the total:

$$\begin{aligned} W_L &= 2\pi \int_{\frac{\pi}{2}}^{\pi} \frac{dW(\theta)}{d\Omega} \sin\theta d\theta = \frac{W_{\text{tot}}}{2} \left(1 - \frac{1}{2}\beta_1 + \frac{1}{8}\beta_3 \right) \\ W_U &= 2\pi \int_0^{\frac{\pi}{2}} \frac{dW(\theta)}{d\Omega} \sin\theta d\theta = \frac{W_{\text{tot}}}{2} \left(1 + \frac{1}{2}\beta_1 - \frac{1}{8}\beta_3 \right) \end{aligned} \quad (6.3)$$

For $\alpha_L = 1$ (or 0), all the photoelectrons go to the lower (upper) side, while at $\alpha_L = 0.5$, there is no preference over either direction; this usually happens at resonances when one of the definite parity pathways is dominant. β_j and the total rate W_{tot} in terms of the transition amplitudes $c_l e^{i\phi_l}$ are given here:

$$\begin{aligned}
W_{\text{tot}} &= c_0^2 + c_1^2 + c_2^2 \\
W_{\text{tot}}\beta_1 &= 2\sqrt{3}c_0c_1 \cos[\Delta\Phi - (\phi_0 - \phi_1)] + 4\sqrt{\frac{3}{5}}c_1c_2 \cos[\Delta\Phi - (\phi_2 - \phi_1)] \\
W_{\text{tot}}\beta_2 &= 2c_1^2 + \frac{10}{7}c_2^2 + 2\sqrt{5}c_0c_2 \cos(\phi_2 - \phi_0) \\
W_{\text{tot}}\beta_3 &= 6\sqrt{\frac{3}{5}}c_1c_2 \cos[\Delta\Phi - (\phi_2 - \phi_1)] \\
W_{\text{tot}}\beta_4 &= \frac{18}{7}c_2^2
\end{aligned} \tag{6.4}$$

Therefore the directional asymmetry parameter α_L is:

$$\begin{aligned}
\alpha_L &= \frac{1}{2} - \frac{\sqrt{3}/2}{c_0^2 + c_1^2 + c_2^2} \left\{ c_0c_1 \cos[\Delta\Phi - (\phi_0 - \phi_1)] + \frac{\sqrt{5}}{4}c_1c_2 \cos[\Delta\Phi - (\phi_2 - \phi_1)] \right\} \\
&\equiv \frac{1}{2} + A(\chi, \varepsilon) \cos[\Delta\Phi - \varphi(\varepsilon)]
\end{aligned} \tag{6.5}$$

The second equality of Eq. 6.5 recasts the directional asymmetry parameter α_L in terms of an amplitude $A(\chi, \varepsilon)$ and a phase $\varphi(\varepsilon)$, both of which are energy sensitive ($\varepsilon = E_g + 2\omega$ is the final state energy). The amplitude A also depends on the electric fields $\mathcal{E}_{\omega, 2\omega}$, as a function of $\chi = \mathcal{E}_{\omega}^2/\mathcal{E}_{2\omega}$, while φ is independent of the field strengths. $0 \leq A \leq \frac{1}{2}$ and $0 \leq \varphi \leq 2\pi$. In order to maximize α_L , φ should equal the optical phase difference. As we will show, φ is encoded with electron-correlation information as are the phases ϕ_i . The influence of the optical interference phase $\Delta\Phi$, the reduced electric field strength χ , and the final state energy ε to α_L will be the topic of next subsection.

Before the end of this subsection, here we give the formula for the transition amplitudes $c_l e^{i\phi_l}$ under perturbation theory [46, 58]:

$$\begin{aligned}
c_0 e^{i\phi_0} &= \frac{\sqrt{2\pi}}{3} \mathcal{E}_\omega^2 \langle f_0 | \mathcal{G}(\omega, \vec{r}', \vec{r}) \vec{r}' \cdot \vec{r} | i \rangle \\
c_1 e^{i\phi_1} &= \sqrt{2\pi} \mathcal{E}_{2\omega} \langle f_1 | r_z | i \rangle \\
c_2 e^{i\phi_2} &= \frac{\sqrt{2\pi}}{3} \mathcal{E}_\omega^2 \langle f_2 | \mathcal{G}(\omega, \vec{r}', \vec{r}) (3r'_z r_z - \vec{r}' \cdot \vec{r}) | i \rangle
\end{aligned} \tag{6.6}$$

Here $|i\rangle$ and $|f_l\rangle$ are the energy eigenstates for the unperturbed helium atom. In the formula above, we rearrange the dipole operators: usually for one- and two-photon transitions we have $D^{(1)} = \vec{r} \cdot \hat{\varepsilon}$ and $D^{(2)} = (\vec{r}' \cdot \hat{\varepsilon})(\vec{r} \cdot \hat{\varepsilon})$ (where vector operator $\vec{r} = \vec{r}_1 + \vec{r}_2$). In Eq. 6.6 the single-photon and two-photon electric dipole transition operators are written as rank-0,-1 and -2 tensors for different l . For the two-photon amplitudes, the Green's function is introduced for the intermediate ATI transition and can be written formally as, $\mathcal{G}(\omega, \vec{r}', \vec{r}) = \mathcal{F}_m \frac{\langle \vec{r}' | m \rangle \langle m | \vec{r} \rangle}{\omega + E_g - E_m}$, Which have been introduced and discussed in Chap.3, Sec.3.2, Subsec.3.2.1. The intermediate energies E_m include all the eigenvalues of the unperturbed helium Hamiltonian that obey the parity and angular momentum selection rules and $|m\rangle$ includes both bound and continuum states with different normalizations.

6.2 Results

6.2.1 Phase- and amplitude- sensitive control

In this section, the optical control of α_L will be discussed in terms of three parameters: the relative laser phase $\Delta\Phi$, the reduced field strength $\chi = \mathcal{E}_\omega^2 / \mathcal{E}_{2\omega}$, and the final state energy ε that plays a major role owing to the existence of resonances. The computation of $A(\chi, \varepsilon)$ and $\varphi(\varepsilon)$ versus energy is the main feature of our work, plus the identification of regions where very high control is readily achievable. With the knowledge of α_L , the redirection of photoelectron emission can be discussed in a more complete manner, as control can be optimized by choosing energies that maximize the directional asymmetry. In addition, photocurrents can be redirected not only through phase control, but also by tuning the photon frequency with fixed phases and field strengths.

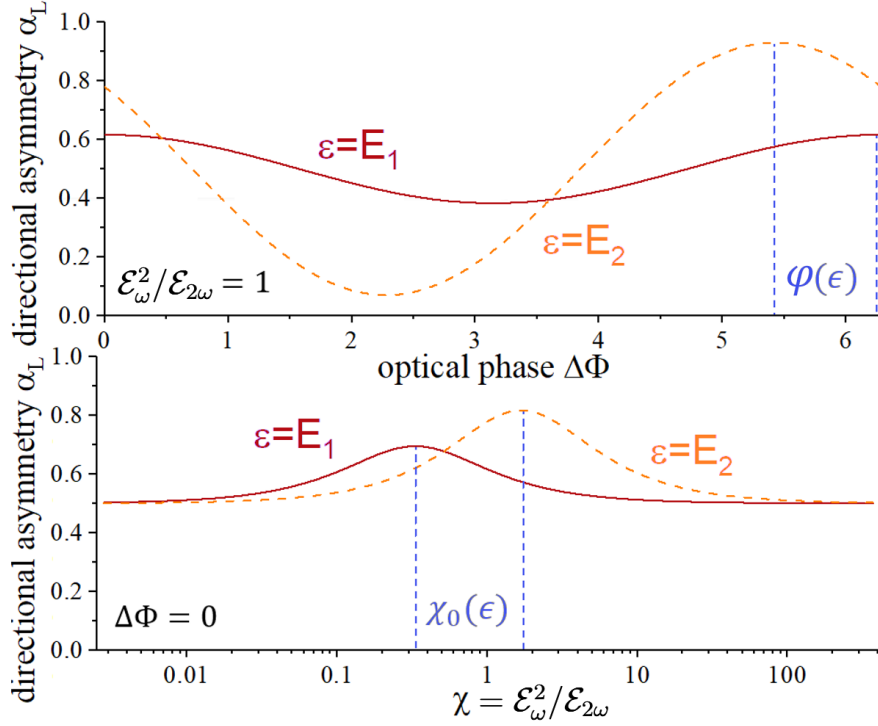


Figure 6.2. The directional asymmetry α_L versus relative phase $\Delta\Phi$ and the reduced field strength $\chi = \mathcal{E}_\omega^2/\mathcal{E}_{2\omega}$ at an arbitrary single energy. The former shows a sinusoidal modulation, while the latter has a single extremum at χ_0 .

First, consider our results for α_L^{max} when the reduced field strength χ and optical phase difference $\Delta\Phi$ are optimized at each energy. To maximize α_L the choice of optical phase is $\Delta\Phi = \varphi(\varepsilon)$, (Fig. 6.3 (b)). The choice of χ is determined by writing the amplitude A in the form $A(\chi, \varepsilon) \propto \chi/(a(\varepsilon) + b(\varepsilon)\chi^2)$, with $a(\varepsilon)$ and $b(\varepsilon)$ being determined from Eq. 6.6. A single peak of $A(\chi, \varepsilon)$ exists at $\chi_0(\varepsilon)$. Note that whatever is the value of χ , there is no influence on the value of φ , and therefore the two parameters can be tuned separately and independently. By selecting a proper χ , we can largely improve the efficiency of coherent phase control of the directional electron photoemission.

Our calculated $\alpha_L^{max} = 1/2 + A(\chi_0(\varepsilon), \varepsilon)$ is plotted in Fig. 6.3 (a), as the solid curve. Observe that α_L^{max} ranges between 0.65 – 1.0 and indicates a quite high-efficiency level of control. However, at energies near the resonances, which are the regions of our greatest interest, α_L^{max} drops down. This is expected since the symmetry of any specific resonance has a single transition amplitude there that overwhelms the amplitude from other channels,

to redirect the photocurrent, as is discussed below. The changes of $\varphi(\varepsilon)$ show a behavior similar to that of the dipole transition phases ϕ_l (the dashed curves), which are properties of the final and intermediate scattering states. The wave function of a detected photoelectron satisfies the incoming wave boundary condition [27]: It approaches the outgoing wave portions of a plane wave pointing towards the detector at infinity, implying that the scattering wave function can be parameterized as, $\psi_f(r) \rightarrow \frac{1}{\sqrt{2\pi k}} \left(e^{ikr} r^{i/k} - e^{-2i\delta_l} e^{-ikr} r^{-i/k} \right)$, where $\delta_l = \eta_l + \pi\tau_l$, with η_l the Coulomb phase parameters: $\eta_l = \frac{\ln(2k)}{k} + \arg[\Gamma(l+1 - \frac{i}{k})] - \frac{l\pi}{2}$, and τ_l incorporate both the quantum defects and the influences from all the closed channels[28]. For the single-photon transition we have $\phi_1 = \delta_1$. For a two-photon ATI process, there is an extra phase that comes from $\mathcal{G}(\omega, \vec{r}', \vec{r})$. Since the undetected intermediate scattering wave can be treated as purely outgoing at large distance [54], $\mathcal{G}(\omega, \vec{r}', \vec{r})$ can be written into a principal value part and an ‘‘on shell’’ part as [24]:

$$\mathcal{G}(\omega, \vec{r}', \vec{r}) = \mathcal{G}^{(P)}(\omega, \vec{r}', \vec{r}) - i\pi \langle \vec{r}' | m^{(sh)} \rangle \langle m^{(sh)} | \vec{r} \rangle \quad (6.7)$$

where $\mathcal{G}^{(P)}(\omega, \vec{r}', \vec{r})$ is the principal value Green’s function, and the on-shell state $\langle \vec{r}' | m^{(sh)} \rangle$ is $\langle \vec{r}' | m \rangle$ at energy $E_m = E_g + \omega$. The complex-valued on-shell contribution introduces an intermediate phase, which is partly responsible for the nonzero value of the minimum total cross section for the two-photon ATI process in the Fano lineshape [58]. In contrast, the minimum total cross-section is normally expected to be zero for an autoionizing state that can decay into only one continuum.

6.2.2 Frequency-sensitive control

Based on the discussions of $A(\chi, \varepsilon)$ and $\varphi(\varepsilon)$, we now explore the possibility of redirecting the photocurrent through frequency control. As demonstrated in Fig. 6.3, the asymmetric phase φ changes rapidly with energy when across the resonance, therefore with a fixed optical phase $\Delta\Phi$, a small change of ε can flip the escape direction of the photoelectrons between upper and lower halves of emission sphere. Now we consider the difference of α_L at two

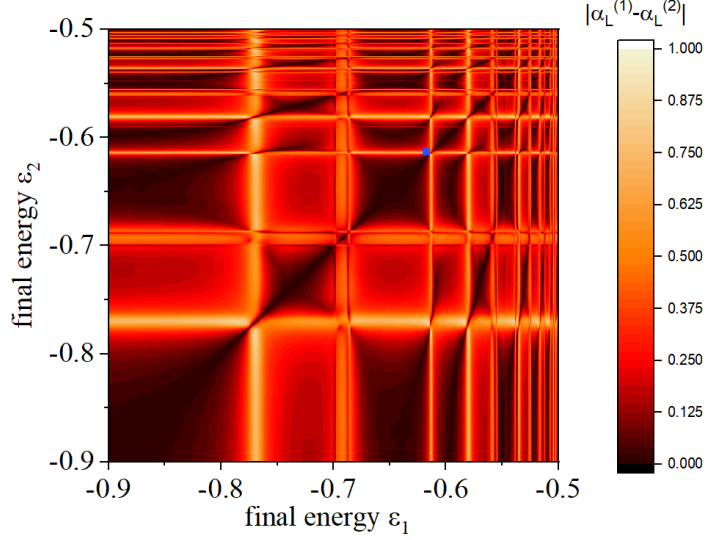


Figure 6.4. The differences in photoelectron directional asymmetry $|\alpha_L^{(1)} - \alpha_L^{(2)}|$ are shown for all possible $(\varepsilon_1, \varepsilon_2)$ from -0.5 *a.u.* to -0.9 *a.u.*. $\Delta\Phi$ and χ are chosen to optimize the difference $|\alpha_L^{(1)} - \alpha_L^{(2)}|$ at each value of the two energies on the plane. The bright grids indicate places where the energy pairs have a large angular asymmetry, and they show a close overlap with the “resonance mesh” of horizontal and vertical stripes. The blue point near the S-wave $2p^2$ resonance indicates the energies considered in Fig. 6.5. This figure is taken from Ref.[125].

energies ε_1 and ε_2 , using the same optical quantities $(\Delta\Phi, \chi)$. This gives an expression for $(\alpha_L^{(1)} - \alpha_L^{(2)})$, namely

$$\begin{aligned} \alpha_L^{(1)} - \alpha_L^{(2)} &= A_1 \cos(\Delta\Phi - \varphi_1) - A_2 \cos(\Delta\Phi - \varphi_2) \\ &= \text{Re} \left[e^{i\Delta\Phi} (A_1 e^{-i\varphi_1} - A_2 e^{-i\varphi_2}) \right] \end{aligned} \quad (6.8)$$

For this exploration $\Delta\Phi = -\text{arg}(A_1 e^{-i\varphi_1} - A_2 e^{-i\varphi_2})$, and χ is chosen to maximize $|A_1 e^{-i\varphi_1} - A_2 e^{-i\varphi_2}|$ at each pair of energies. Next we scanned through all the $(\varepsilon_1, \varepsilon_2)$ from -0.5 *a.u.* to -0.9 *a.u.* to search for candidates that have a large orientation difference. The maximum $|\alpha_L^{(1)} - \alpha_L^{(2)}|$ for all the energy points are shown in Fig. 6.4 .

The bright grids represent regions where the angular asymmetry difference $|\alpha_L^{(1)} - \alpha_L^{(2)}|$ is large, which generally tends to happen when at least one energy is close to a resonance. When both $\varepsilon_1, \varepsilon_2$ are far from resonances $|\alpha_L^{(1)} - \alpha_L^{(2)}|$ is small, which is expected since according to

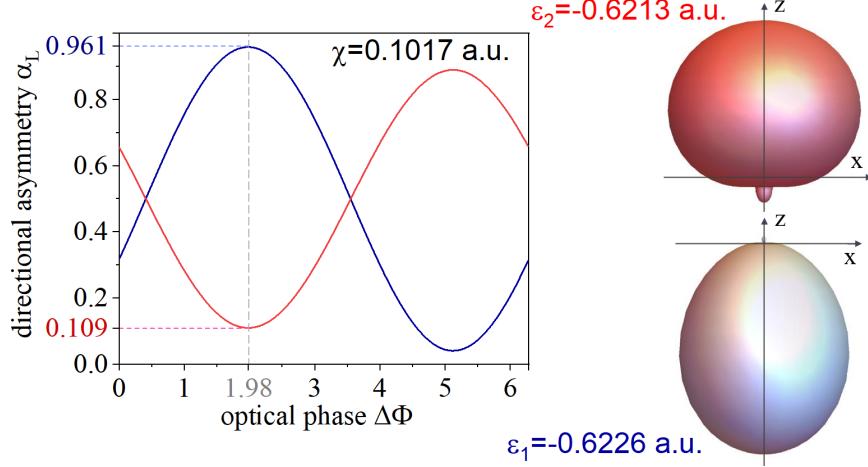


Figure 6.5. An example demonstrating how frequency-sensitive control can almost completely redirect the photoelectrons. The parameters are given in the figure. At $\Delta\Phi = 0.63\pi$ (dashed vertical line) $\alpha_L^{(1)} - \alpha_L^{(2)}$ is maximized, with the values marked on the ticks. A polar plot of $\frac{dW(\theta)}{d\Omega}$ using the parameters indicated by the dashed lines is given in the right panel. With two very close frequencies, one that drives most photoelectrons along the polarization axis $+\hat{z}$, while the other opposite to that direction. This figure is taken from Ref.[125].

Fig. 6.3 in those regions $\varphi_{1,2}$ show little difference from each other. The points of greatest interest are near the intersections of the grids, where $|\alpha_L^{(1)} - \alpha_L^{(2)}|$ rapidly changes, i.e. in those regions where both energies are on or near resonance. A specific example point has been selected near the S -wave $2p^2$ resonance, shown in Fig. 6.4 as a blue point, for the following analysis.

The blue point is at $\varepsilon_1 = -0.6226 \text{ a.u.}$ and $\varepsilon_2 = -0.6213 \text{ a.u.}$, which go across the S -wave $2p^2$ resonance at -0.6219 a.u. with width $\Gamma = 2.36 \times 10^{-4} \text{ a.u.}$. The corresponding values of the other key parameters are $\chi = 0.1017$, $\Delta\Phi = 0.63\pi$. Their directional asymmetry parameters $\alpha_L^{(1),(2)}$ versus $\Delta\Phi$ are presented in Fig. 6.5, and they are entirely out of phase from each other; when $\Delta\Phi = 0.63\pi$, both of the asymmetry parameters reach their corresponding extrema with values 0.961 and 0.109. The choice of χ maximizes this disparity, and it enables the one-photon transition(p -wave) to be strong enough to interfere with the strong on-resonance two-photon transition(s -wave). To examine the physics at those extremum points, the PAD $dW(\theta)/d\Omega$ is calculated with the parameters cited above, shown in Fig. 6.5 right

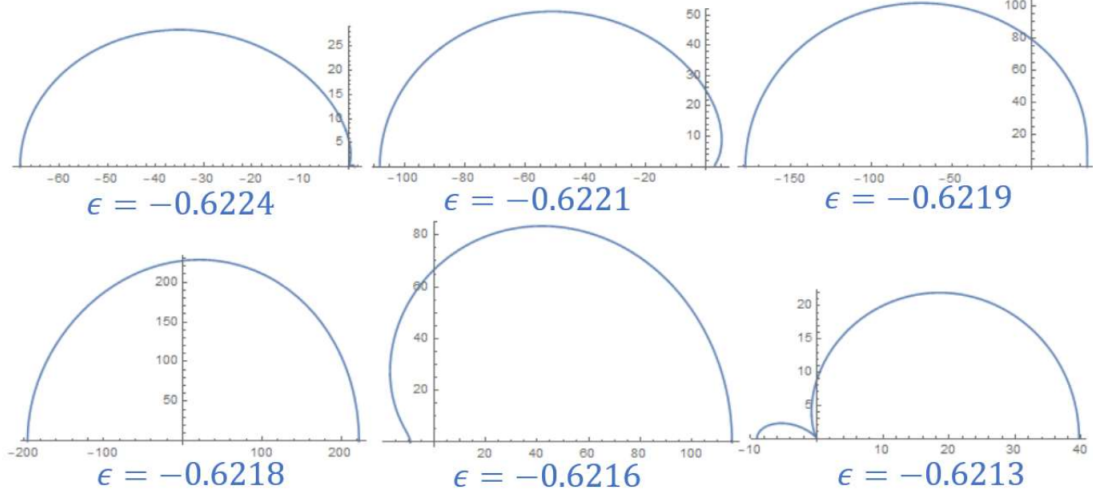


Figure 6.6. $\frac{dW}{d\Omega}$ for six energy points between -0.6224 and -0.6213 *a.u.*, which demonstrates how the PAD changes across the S-wave $2p^2$ resonance at -0.6219 *a.u.*. When the energy is closest to the resonance energy, its PAD is almost symmetric in both directions.

panel. This demonstrates how different the photoejection directions can be at $\varepsilon_1 = -0.6226$ *a.u.* ($\omega = 31.032$ eV) and $\varepsilon_2 = -0.6213$ *a.u.* ($\omega = 31.049$ eV). The central energies $\varepsilon_1, \varepsilon_2$ have been convolved over a resolution of $\pm 3.5 \times 10^{-4}$ *a.u.* (0.01 eV), in order to simulate a realistic experiment with finite resolution.

One realization of the reduced field at $\chi = \mathcal{E}_\omega^2 / \mathcal{E}_{2\omega} = 0.1017$ *a.u.* is to use lasers with intensities $I_\omega = 2.0 \times 10^{13}$ W cm $^{-2}$ (fundamental) and $I_{2\omega} = 1.10 \times 10^{12}$ W cm $^{-2}$ (second harmonic), where $\mathcal{E}_\nu = \sqrt{2I_\nu / \varepsilon_0 c}$ a.u. / 5.1422×10^9 V cm $^{-1}$. Based on these laser intensities, we analyze here the reasonableness of a possible implementation of this frequency-sensitive control scheme. The total rates for asymmetric photoejection in Fig. 6.5 are, $W_{\text{tot}}(\varepsilon_1) = 2.54 \times 10^{-5}$ *a.u.* and $W_{\text{tot}}(\varepsilon_2) = 3.08 \times 10^{-5}$ *a.u.*, but these only include photoelectrons that escaped after absorbing 2ω of energy. There are extra photoelectrons that escape from the two-photon pathway intermediate process, i.e. from absorbing a single photon of frequency ω , which have not been discussed, because they are not being controlled by the optical interference effect. The ionization rate for the “intermediate state leaked” ω -absorption process is much stronger, usually by a factor of 100, than the 2ω -absorption process. At energies ε_1 and ε_2 , their corresponding intermediate ionization rates are around 1.99×10^{-3}

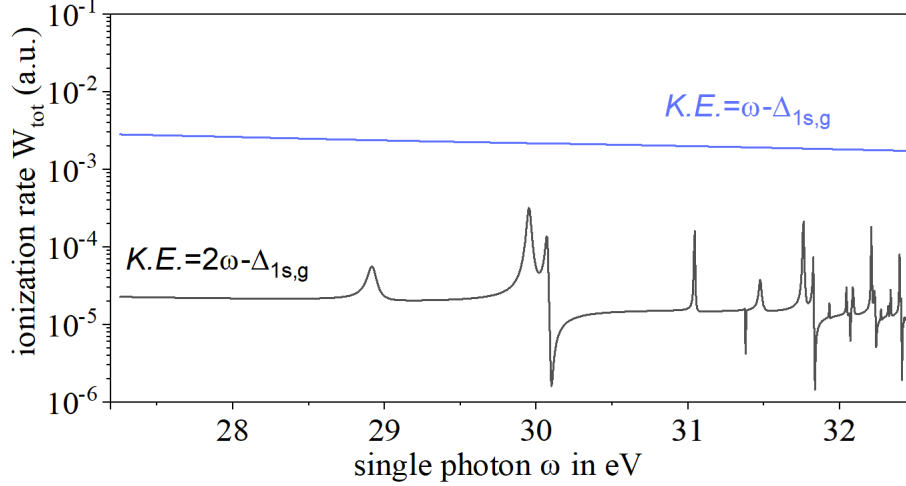


Figure 6.7. The ionization rate of photoelectron escaping with different kinetic energies ($K.E.$), with laser intensities $I_\omega = 2.0 \times 10^{13} \text{ W cm}^{-2}$ and $I_{2\omega} = 1.10 \times 10^{12} \text{ W cm}^{-2}$. $\Delta_{1s,g} = E_{1s} - E_g = 24.58 \text{ eV}$ is the energy difference from the $1s$ threshold and the ground state. The ionization rate at $\omega - \Delta_{1s,g}$ is about 100 times larger than the rate for $2\omega - \Delta_{1s,g}$, which makes it challenging to detect the directional asymmetry properties of the faster electrons, although the two different energies are readily discriminated. This figure is taken from Ref.[125].

a.u.. Thus to observe the experimental interference control predicted in the present study, electron energy discrimination is required. The ionization rates W_{tot} for both the processes covering final state energy ε from -0.9 to -0.5 a.u. are given in Fig. 6.5. The dominance of intermediate ionization is rather typical for most ATI processes, except for a few cases when the intermediate states hit a near-zero ionization minimum, which are found in some alkaline earth atoms such as Ca, Sr, and Ba. Searching for proper ionization processes that can suppress the intermediate leakage can be a goal for our future study. For helium where the intermediate states lie in a flat continuum for the energy range considered in this study, the ratio between for 2ω - and ω -absorption is around $\mathcal{E}_\omega^2 \text{ a.u.}$ —very tiny for electric field below the tunneling region, which implies that the optical control scheme is not highly efficient.

To conclude, the present treatment of energy-dependent coherent control over the directional asymmetry of helium ionization has identified the optical phase difference $\Delta\Phi$ and reduced electric field strength χ that largely enhance the degree of control of the directional photoejection asymmetry. Our study suggests an alternative way of redirecting the photo-

electrons by changing the laser frequency but with a fixed relative phase and field strength ratio, and we presented an example using this frequency-sensitive controlling scheme to redirect photoelectron with final state energies across the S-wave $2p^2$ resonance. However, due to the existence of intermediate-state photoionization, the coherent control can only influence a small fraction of the total electron current which makes any experimental test of our predictions demanding. Future studies of the alkaline earth atoms that have a continuum ionization minimum of either the Fano- or Cooper-type might circumvent this issue.

7. MULTI-CHANNEL COHERENT CONTROL AND PHASE LAG OF ATOMIC BARIUM

In the last chapter, we discussed the $\omega - 2\omega$ coherent control of a single channel in atomic helium. With a controllable optical phase difference $\Delta\varphi$ between the two laser electric fields, the outcome under control shows a sinusoidal modulation of $\Delta\varphi$. i.e. for an observable p , $p = p_0 + p_1 \cos(\Delta\varphi - \delta)$. In this chapter we consider an especially interesting situation, when the final state can decay into more than one continuum, and those continua respond differently to the optical phase difference. The phase lag from two continua i, i' is defined by $\Delta\delta = \delta^{(i)} - \delta^{(i')}$, which is non-zero for most atoms and molecule. Most of the discussions in this chapter has been published as Ref.[64], which is coauthored with Chris H. Greene.

The phase lag associated with coherent control by two-pathway excitation has been widely studied in both the experimental [37, 38, 110, 111, 112, 113, 129] and theoretical [122, 129, 130, 132, 133, 134, 135, 136] literature. It has been found by many experiments that the phase lag is almost constant as a function of wavelength for flat continua, but varies rapidly at a resonance [129, 130, 137]. The phase lag behavior in the vicinity of resonances has not only drawn the attention of experimentalists interested in potential applications [110, 111, 112, 113], but it has also triggered a series of theoretical investigations aimed at the extraction of insights into the nature of multichannel systems.

7.1 Background

Previous theoretical efforts to clarify the origin and properties of the phase lag are based on simplified models of a few discrete states embedded in two continua [122, 129, 130, 132, 133, 134, 135, 136]. However, the first quantitative comparison between that type of theoretical model and an experimental observation in the final state resonance energy range, conducted by Yamazaki et. al., was far from satisfactory [37, 38]. This suggests that a toy model with phenomenological parameters is not adequate to predict the phase lag behavior in a multichannel, highly-correlated atom such as barium. In this article, we provide an *ab initio* calculation for the experiment of Yamazaki et. al., based on a multi-channel quantum

defect (MQDT) and R -matrix treatment[1, 7, 24, 25, 26], and obtain quantitative agreement with the experimental observations. The system considered by the experiment and by our calculation is the $\omega - 2\omega$ concurrent ionization of atomic barium, with final state energy above two ionization thresholds, namely $6s_{1/2}$ and $5d_{3/2}$ (Fig. 7.1). The role of resonances in our calculated phase lag has been analyzed from a multichannel coupling point of view.

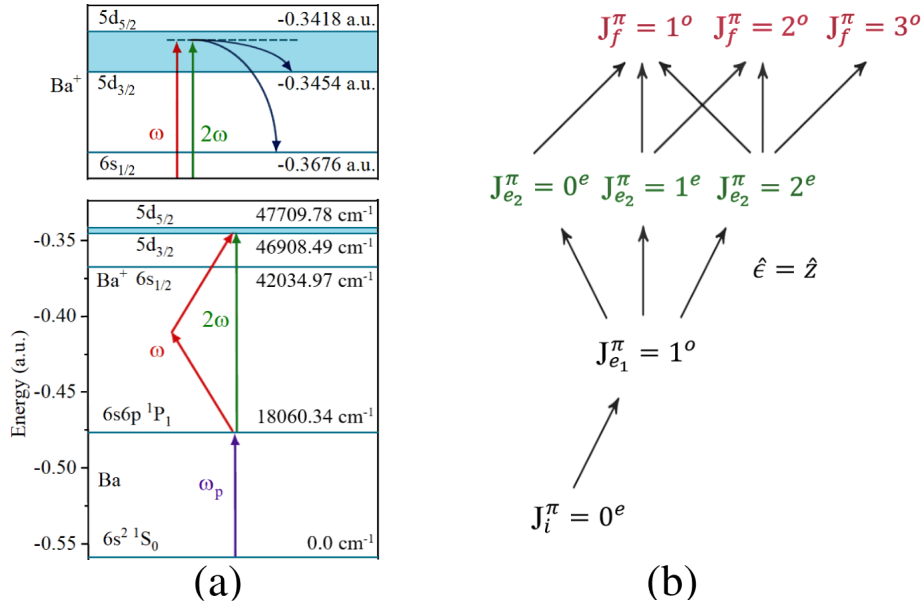


Figure 7.1. (a) Energy level diagram for the barium $\omega - 2\omega$ interference scheme starts from $e_1 = 6s6p$ (1P_1) state (for full ionization steps, see Fig.3.9). The excited atom can decay into either the continua associated with the $6s_{1/2}$ or the $5d_{3/2}$ ionic state. The relevant threshold energy levels are given in the figure in atomic unit and cm^{-1} . (b) The angular momenta J and parity π allowed by the electron-dipole selection rule with all photons polarized along z -axis, as introduced in Fig.3.9. The quantum numbers in green and red give the final states for the one- and two-photon ionizations.

7.1.1 Theoretical description of multi-channel coherent control

In contrast to the previous experiments that focused on controlling chemical products of a photprocess[110, 111, 112, 129], the $\omega - 2\omega$ scheme does not affect the total yield. This is because the absorption of one- or two-photons produces final states with opposite parities $\pi = \{e, o\}$, whereby the interference terms that mix different parities must have odd

parity and cannot be observed by measuring the overall ionization rate.[45, 125, 131] The photoelectron angular distribution (PAD), which can be parameterized by symmetric (S) and anti-symmetric (A) components as $S(\theta, \phi) + A(\theta, \phi) \cos(\Delta\varphi + \delta_0)$ [37], is the observable explored here. The photoelectrons can escape leaving the ion in two different energy eigenstates a and b (referred to loosely in the following as channels), with principal and angular quantum numbers ($n_c L_{cJ_c}$) of the ionic valence electron. For convenience, we consider one of the channels with the channel index being omitted, until later in the article where we explicitly treat the difference between the channels. The differential ionization rate $\frac{dW}{d\Omega}$ can be expressed in terms of spherical harmonics Y_{lm} with complex coefficients $f e^{i\delta}$ as [41]:

$$\frac{dW}{d\Omega} = \mathcal{N}^2 \sum_{\lambda_{in}} \left| \mathcal{E}_\omega^2 \sum_{l=odd} Y_{lm}(\theta, \phi) f_{\gamma,2} e^{i\delta_{\gamma,2}} + \mathcal{E}_{2\omega} e^{i\Delta\varphi} \sum_{l=even} Y_{lm}(\theta, \phi) f_{\gamma,1} e^{i\delta_{\gamma,1}} \right|^2 \quad (7.1)$$

$$f_{\gamma,q} e^{i\delta_{\gamma,q}} = \sum_{\lambda_{co}} \langle J_{cs} M_{J_{cs}}, lm | J_f, M_{J_f} \rangle \langle [(J_c, s) J_{cs}, l] J_f | [(J_c, (l, s)j) J_f] T_{f,i}^{(q)} \rangle.$$

The description of atomic barium is focused on its two active electrons, with the inner and outer electron quantum numbers denoted by $(L_c, s_c)J_c$ and $(l, s)j$. $\vec{J}_{cs} = \vec{J}_c + \vec{s}$, $\vec{J}_f = \vec{J}_{cs} + \vec{l}$. \mathcal{N}^2 is a normalization constant. The incoherent sum index λ_{in} includes J_{cs} , the nuclear spin I , and all the angular momentum projections M . The coherent sum index in Eq.7.1 represents $\lambda_{co} = \{J_f, j\}$, and another index is defined as $\gamma = \{\lambda_{in}, l\}$. Here $T_{f,i}^{(q)}$ is the q -photon transition amplitude from state i to state f , whose formula is given in the Appendix, Eq. 3.25. Because different pathways $q = 1, 2$ produce opposite parities $(-1)^l$, the index q is omitted below. The two electric field strengths are $\mathcal{E}_{2\omega, \omega}$ for the one- and two-photon processes, with corresponding optical phase difference $\Delta\varphi = 2\varphi_\omega - \varphi_{2\omega}$. Because both the pump and ionization lasers are linearly polarized along \hat{z} , the system has azimuthal symmetry. Eq. 7.1 can therefore be arranged into a sum of Legendre polynomials $P_k(\cos \theta)$ with real coefficients β_k as,

$$\frac{dW}{d\Omega} = \frac{W_{tot}}{4\pi} \sum_{k=0}^6 \beta_k P_k(\cos \theta) \quad (7.2)$$

Since we have three-photon ionization at most from the ground state, $k = 6$ is the maximum order. The even and odd orders of $P_k(\cos \theta)$ give the symmetric and anti-symmetric contributions to the photoelectron angular distributions(PADs).

$$\begin{aligned}
W_{\text{tot}} &= \mathcal{E}_{2\omega}^2 \sum_{\lambda_{in}, l_e} f_{\gamma_e}^2 + \mathcal{E}_{\omega}^4 \sum_{\lambda_{in}, l_o} f_{\gamma_o}^2 \\
W_{\text{tot}}\beta_{k_e} &= \mathcal{E}_{2\omega}^2 \sum_{\lambda_{in}, l_e, l'_e} \Theta(l_e, l'_e, k_e, m) f_{\gamma_e} f_{\gamma'_e} e^{i(\delta_{\gamma_e} - \delta_{\gamma'_e})} + \mathcal{E}_{\omega}^4 \sum_{\lambda_{in}, l_o, l'_o} \Theta(l_o, l'_o, k_e, m) f_{\gamma_o} f_{\gamma'_o} e^{i(\delta_{\gamma_o} - \delta_{\gamma'_o})} \\
W_{\text{tot}}\beta_{k_o} &= \mathcal{E}_{2\omega} \mathcal{E}_{\omega}^2 \sum_{\lambda_{in}, l_o, l_e} \Theta(l_o, l_e, k_o, m) f_{\gamma_o} f_{\gamma_e} \left[e^{i(\delta_{\gamma_o} - \delta_{\gamma_e} - \Delta\varphi)} + e^{-i(\delta_{\gamma_o} - \delta_{\gamma_e} - \Delta\varphi)} \right]
\end{aligned} \tag{7.3}$$

The degree of asymmetry of the PAD along the z-axis is quantified by the directional asymmetry parameter, defined as $\alpha_{asym} = W_{-z}/W_{tot}$, the ratio between the $-z$ directed photoelectron current and the total [37, 38, 125]. It is given by:

$$\begin{aligned}
\alpha_{asym} &= \frac{2\pi}{W_{\text{tot}}} \int_{\frac{\pi}{2}}^{\pi} \frac{dW(\theta)}{d\Omega} \sin \theta d\theta = \frac{1}{2} \left(1 + \sum_k \rho_k \beta_k \right) \\
&\equiv \frac{1}{2} + A \cos(\Delta\varphi - \delta_0)
\end{aligned} \tag{7.4}$$

$\rho_k \equiv \int_{-1}^0 P_k(x) dx$, which is $\{-\frac{1}{2}, \frac{1}{8}, -\frac{1}{16}\}$ for $k = \{1, 3, 5\}$ and is 0 when k is even. The second line of Eq. 7.4 recasts α_{asym} in terms of an amplitude A and phase δ_0 . $0 \leq A \leq \frac{1}{2}$ and $0 \leq \delta_0 \leq 2\pi$. The electric field strengths for the fields with frequencies $\mathcal{E}_{\omega, 2\omega}$ affect the amplitude A only. The phase δ_0 can be expressed in terms of $f e^{i\delta}$ and angular momentum coefficients as:

$$\delta_0 = -arg \left[\sum_{\lambda_{in}, l_o, l_e, k_o} \rho_{k_o} \Theta(l_o, l_e, k_o, m) f_{\gamma_o} f_{\gamma_e} e^{i(\delta_{\gamma_e} - \delta_{\gamma_o})} \right] \tag{7.5}$$

where

$$\Theta(l, l', k, m) = (2k + 1) \int Y_{l,m}(\theta, \phi) P_k(\cos \theta) Y_{l',m}^*(\theta, \phi) d\Omega$$

Note that the subscript $e(o)$ for l and k denotes even(odd) numbers, and $\gamma_{e(o)} = \{\lambda_{in}, l_{e(o)}\}$. δ_0 comes from the interference terms between l_e and l_o . The phase lag is defined as $\Delta\delta \equiv \delta_0^{(a)} - \delta_0^{(b)}$. For the ionization scheme being considered for the Ba atom, the two channels are $a = 6s_{1/2}$ and $b = 5d_{3/2}$. The energetically closed $5d_{5/2}$ channel supports autoionizing states. Angular momenta correspond to those channels are listed in Table.7.1. The energy-dependent calculations carried out here are plotted versus final state energies from 47200 to 47265 cm^{-1} relative to the ground state, which is roughly one cycle of the $5d_{5/2}$ Rydberg series, with the effective principle quantum number of the fragmentation electron being $\nu = 1/[2(E_{5d_{5/2}} - E)]^{\frac{1}{2}} = 14.7 - 15.7$. Barium photoionization spectra in this energy range have been previously measured [37, 38, 138, 139, 140] in the laser wavelength range $\lambda_\omega = 684.82 - 686.35 nm$.

Table 7.1. Channels relevant to evaluating equations 7.1-7.5, represented by total angular momentum and parity J_f^π and jj - coupled basis $n_c L_c J_c(l, j)$ (the subscript c denotes ion core). The row “channel a(b)” lists the angular momenta for the fragmentation electron. The row “resonance” gives the angular momenta of the autoionizing states that converge to the $5d_{5/2}$ threshold.

J_f^π	one-photon paths			two-photon paths		
	0^e	1^e	2^e	1^o	2^o	3^o
$6s_{1/2}\epsilon(l, j)$ (channel a)	(0, 1/2)	(0, 1/2) (2, 3/2)	(2, 3/2) (2, 5/2)	(1, 1/2) (1, 3/2)	(1, 3/2) (3, 5/2)	(3, 5/2) (3, 7/2)
$5d_{3/2}\epsilon(l, j)$ (channel b)	(2, 3/2)	(0, 1/2) (2, 3/2) (2, 5/2)	(0, 1/2) (2, 3/2) (2, 5/2) (4, 7/2)	(1, 1/2) (1, 3/2) (3, 5/2)	(1, 1/2) (1, 3/2) (3, 5/2) (3, 7/2)	(1, 3/2) (3, 5/2) (3, 7/2)
$5d_{5/2}n(l, j)$ (resonances)	(2, 5/2)	(2, 3/2) (2, 5/2) (4, 7/2)	(0, 1/2) (2, 3/2) (2, 5/2) (4, 7/2) (4, 9/2)	(1, 3/2) (3, 5/2) (3, 7/2)	(1, 1/2) (1, 3/2) (3, 5/2) (3, 7/2)	(1, 1/2) (1, 3/2) (3, 5/2) (3, 7/2)

7.1.2 The blow-up of phenomenological model description

Previous theoretical investigations of the phase δ_0 were based on the partitioned Lippmann-Schwinger equation, which separates the transition amplitude $f e^{i\delta}$ into a direct ($f^d e^{i\delta^d}$) and a resonance-mediated ($f^r e^{i\delta^r}$) component [37, 129, 130, 132, 133]. The first term describes

the direct ionization from the initial state i directly to the continuum final state ξ , while the latter describes the pathway to the continuum via an autoionizing state n that couples to ξ through an electron correlation matrix element $V_{n\xi}$. These two amplitudes are represented as:

$$f^d e^{i\delta^d} = D_{\xi i} \quad f^r e^{i\delta^r} = \sum_n \frac{V_{\xi n} \Omega_{ni} (1 - i/q_n)}{E - (E_n - i\Gamma_n/2)}, \quad (7.6)$$

where $\Omega_{ni}(1 - \frac{i}{q_n}) = D_{ni} + \sum_{\xi'} \int dE_{\xi'} \frac{V_{n\xi'} D_{\xi'i}}{E_n - E_{\xi'}}$, q_n is the Fano lineshape asymmetry parameter and Γ_n is the line width of resonance n . This model attributes the large value of $\Delta\delta$ and its strong variation near the resonance to the interference between $f^d e^{i\delta^d}$ and $f^r e^{i\delta^r}$. When $f^r e^{i\delta^r} = 0$ (far from resonances), $\delta_0(E)$ is almost constant. When $D_{\xi i} = 0$, $q_n \rightarrow \infty$ (in the centre of an isolated symmetric resonance), δ_0 are determined by the complex resonance energy $(E_n - i\Gamma_n/2)$, in situations discussed by those papers where both optical paths lead to the same final state, $\Delta\delta$ obtain a local minimum.

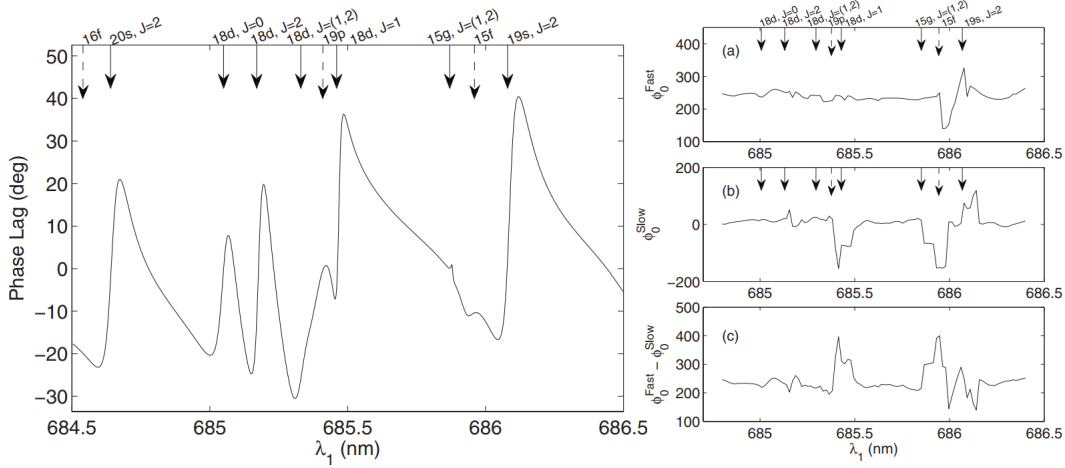


Figure 7.2. Recopy of Fig. 11 and 12 in Ref.[37]. Left panel: Resulting phase lag between the two photoionization channels calculated using the autoionizing parameters presented in Ref.[37], Tables I and II. Locations of resonances are marked with dashed and solid arrows at the top. Right panel: Calculated phase lag due to the variation of the outgoing electron waves. First row, ϕ_0 variation for the fast-electron channel; second row, ϕ_0 variation for the slow-electron channel; third row, ϕ_0 variation. The variation of the phase lag was calculated to be as large as 210° .

The Yamazaki *et al.* theory comparison with their experiment used Eq. 7.6 to extract resonance parameters q_n, Γ_n by fitting to their spectra, and it showed a large discrepancy. One sees, in Fig. 7.3 for example, where the experimentally observed $\Delta\delta$ is represented by the blue points, a huge phase variation of 2π is observed at $J_f^\pi = 1^o$ resonances, while Yamazaki *et al.* predicts a maximum phase lag about $\pi/3$ and $7\pi/6$ due to the resonance effect and the outgoing waves (Fig. 7.2 demonstrate the theoretical results in Ref.[37]).

Our analysis of the phase lag $\Delta\delta$ derives from a different picture than the aforementioned single-resonance model, as ours is based on the multichannel quantum defect (MQDT) [7, 24, 25, 26] and the streamlined R -matrix method [1]. The electron correlation is therefore modeled in a realistic manner, and the resonance structure is described in its full multichannel complexity. The details of our calculation have been given in Chap. 3. When one of the electron moves beyond the reaction zone, it experiences an overall Coulomb potential from the other part of the system. The energy range treated here is $E_{6s_{1/2}}, E_{5d_{3/2}} < E < E_{5d_{5/2}}$. Depending on whether the inner electron resides in the $6s_{1/2}$, $5d_{3/2}$ or $5d_{5/2}$ state, it can be described by Coulomb functions with either incoming-wave boundary conditions appropriate to a photofragmentation process into the $E_{6s_{1/2}}, E_{5d_{3/2}}$ channels [27] or an exponentially decaying boundary condition ($5d_{5/2}$ and higher channels) [28]. The asymptotic wave function of barium can be written in terms of the superposition of those channel states as,

$$\begin{aligned} \psi_{i'} \rightarrow & \mathcal{A} \sum_{i \in o} \frac{\Phi_i}{ir} \frac{1}{\sqrt{2\pi k_i}} (e^{ik_i r} r^{i/k_i} \delta_{ii'} - e^{-ik_i r} r^{-i/k_i} S_{ii'}^{\dagger phys}) \\ & + \mathcal{A} \sum_{i \in c} \frac{\Phi_i}{r} W_i(r) Z_{ii'} \end{aligned}$$

The channel function Φ_i includes all the other parts of the barium except the radial motion of the fragmentation electron. $i = \{n_c L_{cJ_c}, l_j\}$. $i \in o$ or c indicates the quantum numbers of ion core $n_c L_{cJ_c} = 6s_{1/2}, 5d_{3/2}$ or $5d_{5/2}$. \underline{S}^{phys} is the physical scattering matrix and \underline{Z}_{co} is the coefficient of the exponentially decaying (rescaled) Whittaker function $W_i(r)$:

$$\begin{aligned} \underline{S}^{\dagger phys} &= e^{-i\eta} \tilde{\underline{S}}^{\dagger} e^{-i\eta} & \tilde{\underline{S}}^{\dagger} &= \underline{S}_{oo}^{\dagger} - \underline{S}_{oc}^{\dagger} (\underline{S}_{cc}^{\dagger} - e^{2i\beta})^{-1} \underline{S}_{co}^{\dagger} \\ \underline{Z}_{co} &= e^{i\beta} (\underline{S}_{cc}^{\dagger} - e^{2i\beta})^{-1} \underline{S}_{co}^{\dagger} e^{-i\eta} \end{aligned} \tag{7.7}$$

η is the Coulomb plus centrifugal phase, and is almost constant across this energy range, and the negative energy phase parameter is $\beta = \pi(\nu - l)$. Considering the ionization from an initial state i directly to ψ_V , the components with coefficients $\underline{S}_{oc}^\dagger (\underline{S}_{cc}^\dagger - e^{2i\beta})^{-1} \underline{S}_{co}^\dagger$ and \underline{Z}_{co} which represent a pathway through the autoionizing states, correspond to $f^r e^{i\delta^r}$; and components with coefficients $\underline{S}_{oo}^\dagger$, which include the direct transition and transition through couplings between the continua, correspond to $f^d e^{i\delta^d}$. The eigenvalues of \tilde{S}^\dagger are $e^{-2i\pi\tau_\rho}$ [28], as the energy increases across a single isolated resonance, the sum of eigenphases $\sum_\rho \tau_\rho$ changes by 1, which is fundamentally the origin of the variation of the phase lag. The significant differences between our calculated results and the simplified resonance model implemented in Ref.[37] suggests that electron correlation effects, and the rich number of multiple interacting resonances in barium, plays a crucial role in this energy range of barium.

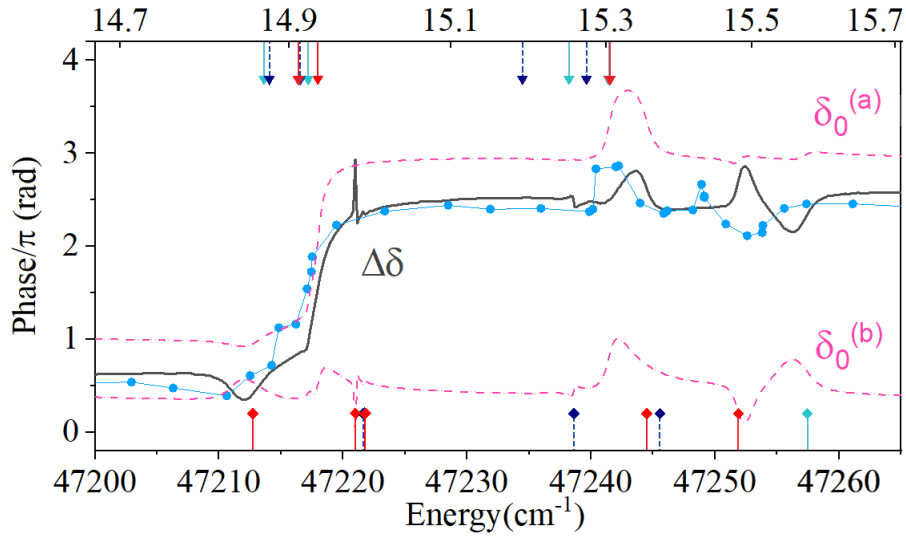


Figure 7.3. Comparison of our calculated phase lag $\Delta\delta = \delta_0^{(a)} - \delta_0^{(b)}$ (solid curve) with the experimental results [38] (blue points) versus energy in cm^{-1} . The top label gives the effective quantum number $\nu = [2(E_{5d_{5/2}} - E)]^{-\frac{1}{2}}$. The dashed curves are δ_0 for $a = 6s_{1/2}$ (upper) and $b = 5d_{3/2}$ (lower) channels. The arrows and the diamonds on the top and bottom give the positions of the two- and one-photon resonances, and their colors correspond to the colors in Fig. 7.4. This figure is taken from Ref.[64].

Table 7.2. The resonances from our calculation (position E and width Γ) and earlier experiments (Ref. [138, 139]). Most experimental two-photon resonances are missing, because of the strong dominance of $J_f = 1$ partial wave. Our classification of the resonances is shown in the $J_f(nl_j)$ basis. For those overlapped resonances, the upper index of Γ give the J_f .

	identification of even-parity resonances $5d_{5/2}nl_j$							
ν	14.86	14.98	14.99	15.26	15.36	15.38	15.48	15.58
$E(cm^{-1})$	47212.77	47220.99	47221.62	47238.53	47244.70	47245.65	47251.81	47257.50
$\Gamma(cm^{-1})$	3.29	0.06	0.07 ¹ , 0.06 ²	0.42	5.74	5.47	1.15	4.63
Exp [138]	47210.86	47220.59	47221.18	47238.77	47241.75	47244.56	47250.81	47256.77
$J_f^e(nl_j)$	2(19s _{1/2})	2(15g _{7/2})	1(15g _{7/2})	1(18d _{5/2})	2(18d _{3/2})	1(18d _{3/2})	2(18d _{5/2})	0(18d _{5/2})
			2(15g _{9/2})					
	identification of odd-parity resonances $5d_{5/2}nl_j$							
ν	14.87	14.88	14.91	14.92	14.93	14.94	15.19	15.26
$E(cm^{-1})$	47213.61	47214.05	47216.39	47216.55	47217.18	47217.99	47234.47	47238.23
$\Gamma(cm^{-1})$	1.34	1.02	2.16	1.11	0.40	1.08	3.32	2.69
Exp [139]						47218.27		
$J_f^o(nl_j)$	3(15f _{5/2})	2(15f _{7/2})	1(15f _{5/2})	2(15f _{5/2})	3(15f _{7/2})	1(15f _{7/2})	2(19p _{1/2})	3(19p _{1/2})
							2(19p _{3/2})	1(19p _{3/2})
								3(19p _{3/2})

7.2 Results

Our computed phase lag and its experimental observations are presented in Fig. 7.3, shown respectively as the solid curve and the points. When $\nu < 15.1$, the two results agrees well, but a significant energy shift of features of around 1.6×10^{-5} *a.u.* shows up when $\nu > 15.1$, which is larger than the difference between the theoretical and experimental resonance positions listed in Table. 7.2. The calculated resonance positions are indicated by the diamonds and the arrows. The ones on the bottom (top) are for one (two)-photon pathway autoionization, and the color labels the resonance angular momentum J_f . The dashed curves in Fig. 7.3 give the interference phases $\delta_0^{(a),(b)}$ for each channel; after each resonance-caused variation, they return to their initial values at $\delta_0^{(a)} = \pi$ and $\delta_0^{(b)} = 0.38\pi$. This indicates that the phase change across the resonances either shift by $2N\pi$, or else they shift back and forth by an arbitrary value, returning to their initial value. It is interesting to note that although our results for the phase lag is derived from the photoelectron angular distributions β_k , the agreement in the phase lag is much better than photoelectron angular distributions results (see Fig.3.11), which suggests that the phase lag could be more robust against small calculated phase and amplitude errors.

To analyze the influence of resonances to the phase shifts, Fig. 7.4 presents our calculated partial cross-sections (Eq. 3.29) for one- and two-photon processes separately. Among the two-photon pathways, the $J_f = 1$ partial wave dominate over other partial wave by orders of magnitude. The $J_f = 3$ resonances, often overlapping with stronger $J_f = 1$ resonances, are therefore hard to observe. Since δ_0 is obtained by a coherent sum over all the partial waves (Eq. 7.5), those with tiny amplitudes do not play a major role. Consequently, only the three resonances from $J_f = 1$ (the red arrows in Fig. 7.3) can appreciably influence the interference phase. Similarly, among the one-photon pathways, it is the resonances from the prominent $J_f = 2$ partial wave, and $J_f = 1, 0$ resonances at $E = 47238.53$ cm^{-1} and 47257.50 cm^{-1} whose signals are strong enough to affect δ_0 .

It is a mysterious that the influence of those resonances to different channels appears quite differently in Fig. 7.3: $\delta_0^{(b)}$ responds sensitively to both one- and two-photon resonances, while $\delta_0^{(a)}$ responds strongly to the two-photon resonances, but remains almost unaltered by

one-photon resonances. One plausible explain is, some of the prominent resonances for one-photon pathway have window-type lineshapes (lower panel solid lines) in $6s_{1/2}$ channel, their transition amplitudes obtain a local minimum and no longer dominant in Eq.7.5, therefore do not affect $fe^{i\delta}$ strongly. As an attempt to explaining why the one- and two-photon resonances can influence $6s_{1/2}$ and $5d_{3/2}$ channels in such a completely difference manner, we preformed time-delay calculations for $J_f^\pi = 1^o$ and 2^e , the dominant partial waves for two- and one- photon ionization. As introduced in Sec.4.2, the largest eigenvalues (q_{max}) of $\underline{Q}^{phys} = -i\underline{S}^{phys\dagger} \frac{d\underline{S}^{phys}}{dE}$ gives the resonance lifetime, and its corresponding eigenvector gives the amplitudes of decaying into each open channel.

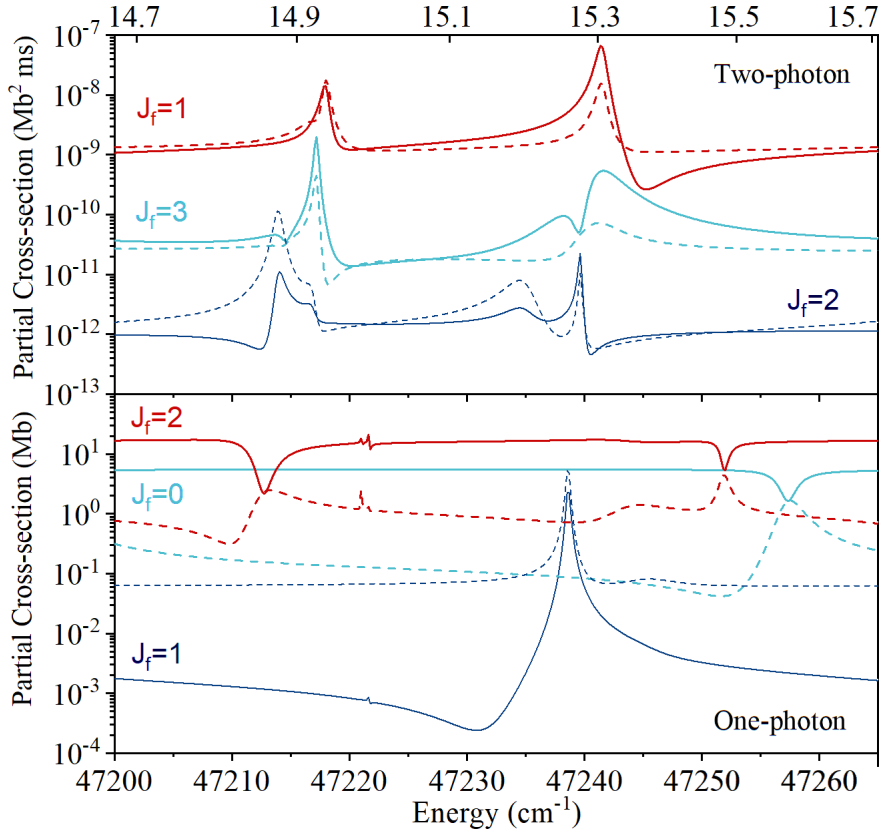


Figure 7.4. Partial cross-sections for two- and one-photon ionization, separately. The solid (dashed) curves give partial cross sections for $a = 6s_{1/2}$ ($b = 5d_{3/2}$) channel. Resonance identification and their comparisons with experiment are given in Table. 7.2. This figure is taken from Ref.[64].

In Fig.7.5 and 7.6, we present the eigenvalues q and the decay probability into each open channel for $J_f^\pi = 1^o$ and 2^e partial waves. For the three $J_f^\pi = 1^o$ resonances, two of them mainly decay into $6s_{1/2}$ channels, as what we have expected. The rest one resonance decays into $5d_{3/2}(1, 3/2)$ channel, but its influence to $\delta_0^{(b)}$ is negligible in Fig. 7.3. As for the five $J_f^\pi = 2^e$ resonances, the dominant channel for two board ones on the right part of Fig.7.6 is $5d_{3/2}(2, 5/2)$. The other board resonance and some of the narrow resonances, however, decay into the $6s_{1/2}(2, 5/2)$ channel, which cannot explain the fact that those resonance have a much larger affect to $\delta_0^{(b)}$ than to $\delta_0^{(a)}$.

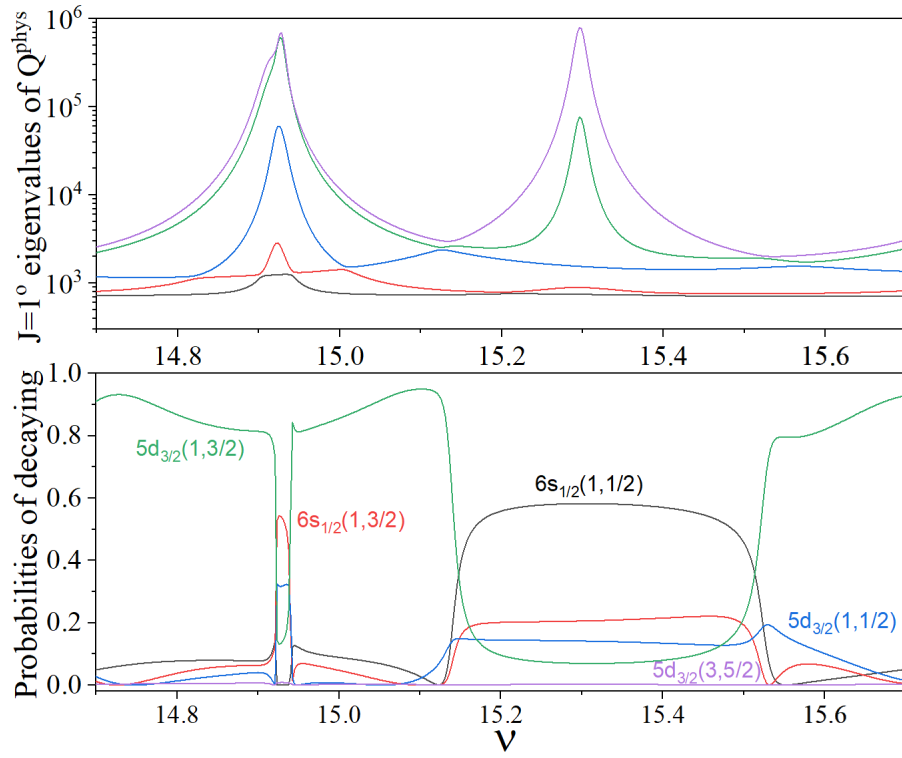


Figure 7.5. Time delay analysis for $J_f^\pi = 1^o$ resonances. The upper figure shows the eigenvalues of the the time-delay matrix and the lower figure shows partial decay probabilities.

To conclude, we provide quantitative agreement between theory and experiment about phase lag from optical control of photoelectron angular distribution in atomic barium. A full treatment of nonperturbative electron correlations is crucial to incorporate, in order to correctly predict the phase lag behavior, which is beyond the description of a toy-model. Finally, this work provides a detailed study of the barium photoabsorption spectrum be-

tween the $5d_{3/2}$ and $5d_{5/2}$ thresholds, it identifies some resonances that are hardly resolved experimentally, and based on that it enables an attribution of the different influences of those resonances to the phases.

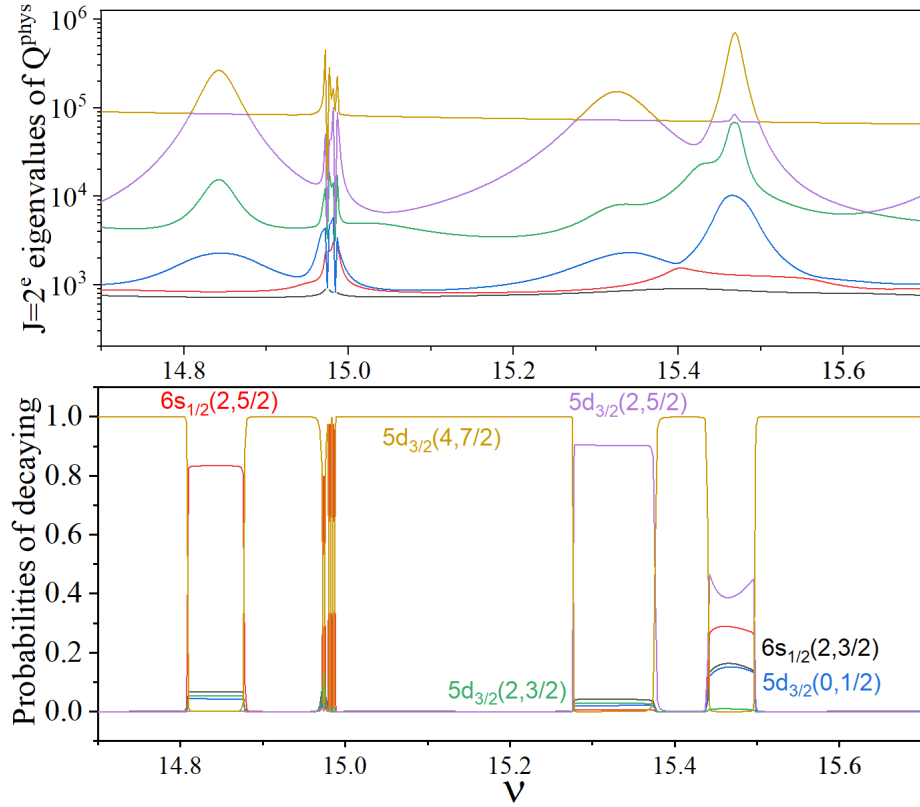


Figure 7.6. Time delay analysis for $J_f^\pi = 2^e$ resonances. The upper figure shows the eigenvalues of the the time-delay matrix and the lower figure shows partial decay probabilities.

8. SUMMARY

Multiphoton ionization provides a clear window into the nature of electron correlations in helium and other alkaline earth atoms. In this thesis, atomic spectra for helium and barium are calculated and discussed, based on the multichannel quantum defect theory (MQDT) and the streamlined R -matrix method. For the ionization of helium, we considered the final-state energy range near the $N = 2$ and $N = 3$ ionization thresholds, with two-photon ionizations proceeding via continuum intermediate states above the lowest threshold, and three-photon ionization with intermediate resonances. Then our analysis classifies the resonances above the $N = 2$ threshold in terms of the $SO(4)$ -group-theory quantum numbers. Their dominant decay channels are found to obey the previously conjectured propensity rule far more weakly for these even-parity states than was observed for the $^1P^o$ states relevant to single-photon ionization.

Next, we propose the generation of attosecond entangled bi-photons in the extreme-ultraviolet regime by two-photon decay of $1s2s\ ^1S^e$ metastable state in helium. This results in an entangled photon pair with correlation time in the attosecond regime, which is a highly suitable source for attosecond pump-probe experiments. We calculate the bi-photon generation rate from a direct four-photon excitation scheme and discuss other feasible schemes to generate these bi-photons.

Besides, our study develops a two-pathway coherent control of helium photoionization for energy up to the $N = 2$ threshold, and three parameters are controlled: the optical interference phase, the electric field strengths, and the final state energy. A small energy change near resonance is shown to flip the emission direction of photoelectrons with high efficiency, through an example where 90% of photoelectrons whose energy is near the $2p^2$ resonance flip their emission direction.

Finally, we considered the ionization of barium, which is firstly pumped onto $6s6p$ state and then be ionized by one or two non-sequential photons, with the final-state energy lying between $5d_{3/2}$ and $5d_{5/2}$ ionization thresholds. We discussed the effects of hyperfine depolarization and extended the formulas to describe the processes from two-photon ionization to three-photon ionization. By treating the phase lag quantitatively in a multichannel coupling

formulation, we achieve quantitative agreement with the experimental observations, which haven't been approached by previous theoretical studies.

REFERENCES

- [1] Mireille Aymar, Chris H. Greene, and Eliane Luc-Koenig. “Multichannel Rydberg spectroscopy of complex atoms”. In: *Rev. Mod. Phys.* 68 (4 Oct. 1996), pp. 1015–1123.
- [2] R. P. Madden and K. Codling. “New Autoionizing Atomic Energy Levels in He, Ne, and Ar”. In: *Phys. Rev. Lett.* 10 (12 June 1963), pp. 516–518.
- [3] J. W. Cooper, U. Fano, and F. Prats. “Classification of Two-Electron Excitation Levels of Helium”. In: *Phys. Rev. Lett.* 10 (12 June 1963), pp. 518–521.
- [4] David R. Herrick. “Resonance-channel quantum numbers in electron-hydrogen and proton-hydrogen scattering from group theory of the long-range dipole interaction”. In: *Phys. Rev. A* 12 (2 Aug. 1975), pp. 413–424.
- [5] Y.K. Ho. “The method of complex coordinate rotation and its applications to atomic collision processes”. In: *Physics Reports* 99.1 (1983), pp. 1–68. ISSN: 0370-1573.
- [6] M J Seaton. “Quantum defect theory I. General formulation”. In: *Proceedings of the Physical Society* 88.4 (Aug. 1966), pp. 801–814.
- [7] M. J. Seaton. *Quantum defect theory*. Rep. Prog. Phys. 46 167, 1983.
- [8] J. Macek. “Properties of autoionizing states of He”. In: *J. Phys. B* 1.5 (1968), p. 831.
- [9] U Fano. “Correlations of Two Excited Electrons”. In: *Rep. Prog. Phys.* 46.2 (1983), pp. 97–165.
- [10] C. D. Lin. “Doubly Excited-States, Including New Classification Schemes”. English. In: *Adv. At. Mol. Opt. Phys.* 22 (1986), pp. 77–142. ISSN: 0065-2199.
- [11] P. G. Burke and Kenneth Smith. “The Low-Energy Scattering of Electrons and Positrons by Hydrogen Atoms”. In: *Rev. Mod. Phys.* 34 (3 July 1962), pp. 458–502.
- [12] Eugene P. Wigner. “Resonance Reactions and Anomalous Scattering”. In: *Phys. Rev.* 70 (1-2 July 1946), pp. 15–33.
- [13] Eugene P. Wigner. “Resonance Reactions”. In: *Phys. Rev.* 70 (9-10 Nov. 1946), pp. 606–618.
- [14] E. P. Wigner and L. Eisenbud. “Higher Angular Momenta and Long Range Interaction in Resonance Reactions”. In: *Phys. Rev.* 72 (1 July 1947), pp. 29–41.

- [15] T. Teichmann and E. P. Wigner. “Sum Rules in the Dispersion Theory of Nuclear Reactions”. In: *Phys. Rev.* 87 (1 July 1952), pp. 123–135.
- [16] P.G. Burke and W.D. Robb. *The R-Matrix Theory of Atomic Processes*. Vol. 11. Advances in Atomic and Molecular Physics. Academic Press, 1976, pp. 143–214.
- [17] P.G. Burke. *Atomic and molecular processes: an R-matrix approach*. Institute of Physics Publishing Ltd, 1993.
- [18] Cheng Chin et al. “Feshbach resonances in ultracold gases”. In: *Rev. Mod. Phys.* 82 (2 Apr. 2010), pp. 1225–1286.
- [19] Jack Simons. *Role played by metastable states in chemistry*. ACS symposium series No.263: resonance in electron-molecular scattering, van de waals complex and reactive chemical dynamics, 1984.
- [20] Harald Friedrich. *Theoretical Atomic Physics, Third Edition*. Springer-Verlag Berlin Heidelberg, 2006.
- [21] U. Fano. “Effects of Configuration Interaction on Intensities and Phase Shifts”. In: *Phys. Rev.* 124 (6 Dec. 1961), pp. 1866–1878.
- [22] P. W. Anderson. “Localized Magnetic States in Metals”. In: *Phys. Rev.* 124 (1 Oct. 1961), pp. 41–53.
- [23] Herman Feshbach. “Unified theory of nuclear reactions”. In: *Annals of Physics* 5.4 (1958), pp. 357–390. ISSN: 0003-4916.
- [24] C. Greene, U. Fano, and G. Strinati. “General form of the quantum-defect theory”. In: *Phys. Rev. A* 19 (4 Apr. 1979), pp. 1485–1509.
- [25] Chris H. Greene, A. R. P. Rau, and U. Fano. “General form of the quantum-defect theory. II”. In: *Phys. Rev. A* 26 (5 Nov. 1982), pp. 2441–2459.
- [26] Chris H. Greene, A. R. P. Rau, and U. Fano. “Erratum: General form of the quantum-defect theory. II”. In: *Phys. Rev. A* 30 (6 Dec. 1984), pp. 3321–3321.
- [27] G. Breit and H. A. Bethe. “Ingoing Waves in Final State of Scattering Problems”. In: *Phys. Rev.* 93 (4 1954), pp. 888–890.
- [28] Chris H. Greene and Ch. Jungen. *Molecular applications of Quantum defect theory*. Advances in Atomic and Molecular Physics, Vol.21, 1985.

- [29] Ellen B. Stechel John C. Light Robert B. Walker and Thomas G. Schmalz. *R-Matrix Propagation Methods in Inelastic And Reactive Collisions*. Computer Physics Communications 17 (1979) 89-97, 1979.
- [30] M S Pindzola and F Robicieux. *Two-photon double ionization of He and H⁻*. J. Phys. B: At. Mol. Opt. Phys. 31 (1998) L823–L831, 1998.
- [31] Liang Feng and Hugo W van der Hart. *Two-photon double ionization of He*. J. Phys. B: At. Mol. Opt. Phys. 36 (2003) L1–L7, 2003.
- [32] L A A Nikolopoulos and P Lambropoulos. *Multichannel theory of two-photon single and double ionization of helium*. J. Phys. B: At. Mol. Opt. Phys. 34 (2001) 545–564, 2001.
- [33] Christian Ott et al. “Lorentz Meets Fano in Spectral Line Shapes: A Universal Phase and Its Laser Control”. In: *Science* 340.6133 (2013), pp. 716–720. ISSN: 0036-8075.
- [34] C. D. Lin and Wei-Chun Chu. “Controlling Atomic Line Shapes”. In: *Science* 340.6133 (MAY 10 2013), 694–695. ISSN: 0036-8075.
- [35] Mengxi Wu et al. “Time-domain perspective on Autler-Townes splitting in attosecond transient absorption of laser-dressed helium atoms”. In: *Phys. Rev. A* 88 (4 Oct. 2013), p. 043416.
- [36] Wei-Chun Chu, Toru Morishita, and C. D. Lin. “Probing and Controlling Autoionization Dynamics with Attosecond Light Pulses in a Strong Dressing Laser Field”. In: *Chinese Journal Of Physics* 52.1, 2, SI (Feb. 2014), pp. 301–319. ISSN: 0577-9073.
- [37] Rekishu Yamazaki and D. S. Elliott. “Strong variation of the phase lag in the vicinity of autoionizing resonances”. In: *Phys. Rev. A* 76 (5 2007), p. 053401.
- [38] Rekishu Yamazaki and D. S. Elliott. “Observation of the Phase Lag in the Asymmetric Photoelectron Angular Distributions of Atomic Barium”. In: *Phys. Rev. Lett.* 98 (5 2007), p. 053001.
- [39] John R. Tolsma et al. “One- and two-photon ionization cross sections of the laser-excited $6s6p\ ^1P_1$ state of barium”. In: *Phys. Rev. A* 80 (3 2009), p. 033401.
- [40] Rekishu Yamazaki and D. S. Elliott. “Product-state control in barium”. In: *Phys. Rev. A* 73 (2 Feb. 2006), p. 023415.
- [41] M. D. Lindsay et al. “Angular distributions of ejected electrons from autoionizing $3pnd$ states of magnesium”. In: *Phys. Rev. A* 46 (7 Oct. 1992), pp. 3789–3806.

- [42] Hugo W. van der Hart and Chris H. Greene. “Regularities and irregularities in partial photoionization cross sections of He”. In: *Phys. Rev. A* 66 (2 Aug. 2002), p. 022710.
- [43] Robert P. Wood, Chris H. Greene, and Darrell Armstrong. “Photoionization of the barium $6s6p\ ^1P^{\circ}_1$ state: Comparison of theory and experiment including hyperfine-depolarization effects”. In: *Phys. Rev. A* 47 (1 Jan. 1993), pp. 229–235.
- [44] Robert P. Wood and Chris H. Greene. *Asymmetric two-electron excitations in atomic strontium and barium*. *Phys. Rev. A*, Vol. 49, No. 2, 1994.
- [45] D. Z. Anderson et al. “Interference of one- and two-photon processes in the ionization of atoms and molecules”. In: *Soviet Physics JETP* 75 (1992), p. 210.
- [46] Joseph H. Macek U. Fano. *Impact excitation and polarization of the emitted light*. *Reviews of Modern Physics*, Vol.45, No.4, 1973.
- [47] Chris H. Greene and Longhuan Kim. “Two-electron excitations in atomic calcium. I”. In: *Phys. Rev. A* 36 (6 Sept. 1987), pp. 2706–2717.
- [48] Chris H. Greene and Constantine E. Theodosiou. “Photoionization of the Ba $6s6p\ ^1P_1$ state”. In: *Phys. Rev. A* 42 (9 Nov. 1990), pp. 5773–5775.
- [49] Chris H. Greene and Mireille Aymar. “Spin-orbit effects in the heavy alkaline-earth atoms”. In: *Phys. Rev. A* 44 (3 Aug. 1991), pp. 1773–1790.
- [50] I.I.Sobel’man. *Introduction to the theory of atomic spectral*. Pergaman Press Ltd, Headington Hill Hall, Oxford, 1972.
- [51] Alejandro Saenz and P Lambropoulos. *Theoretical two-, three- and four-photon ionization cross sections of helium in the XUV range*. *J. Phys. B: At. Mol. Opt. Phys.* 32 5629–5637, 1999.
- [52] Lester Lipsky, Russell Anania, and M.J. Conneely. “Energy levels and classifications of doubly-excited states in two-electron systems with nuclear charge, $Z = 1, 2, 3, 4, 5$, below the $N = 2$ and $N = 3$ thresholds”. In: *Atomic Data and Nuclear Data Tables* 20.2 (1977), pp. 127–141. ISSN: 0092-640X.
- [53] F. Robicheaux and Bo Gao. “Two-photon processes in real atoms”. In: *Phys. Rev. Lett.* 67 (22 Nov. 1991), pp. 3066–3069.
- [54] F. Robicheaux and Bo Gao. “Multichannel quantum-defect approach for two-photon processes”. In: *Phys. Rev. A* 47 (4 Apr. 1993), pp. 2904–2912.

- [55] Bo Gao and Anthony F. Starace. *Numerical methods for free-free radiative transition matrix element*. Computers in Physics(1987), P70-73, 1987.
- [56] M. Gailitis and R Damburg. “Some Features of the Threshold Behavior of the Cross Sections for Excitation of Hydrogen by Electrons Due to the Existence of a Linear Stark Effect in Hydrogen”. In: *Journal of Experimental and Theoretical Physics* 17 (5 Nov. 1963), p. 1107.
- [57] H. R. Sadeghpour, Chris H. Greene, and Michael Cavagnero. “Extensive eigenchannel R-matrix study of the H^- photodetachment spectrum”. In: *Phys. Rev. A* 45 (3 Feb. 1992), pp. 1587–1595.
- [58] Yimeng Wang and Chris H. Greene. “Two-photon above-threshold ionization of helium”. In: *Phys. Rev. A* 103 (3 2021), p. 033103.
- [59] Diego I. R. Boll et al. “Angularly resolved two-photon above-threshold ionization of helium”. In: *Phys. Rev. A* 99 (2 Feb. 2019), p. 023416.
- [60] I Sanchez, H Bachau, and E Cormier. “Theory of two-photon spectroscopy of autoionizing states in helium and beryllium”. In: *Journal of Physics B: Atomic, Molecular and Optical Physics* 28.12 (June 1995), pp. 2367–2384.
- [61] Johannes Eiglsperger. *Highly doubly excited states of two-electron atoms: spectra, cross sections and localization properties*. Technische Universitat Munchen, PhD Dissertation, 2010.
- [62] Y K Ho and J Callaway. “Doubly excited states of helium atoms between the $N=2$ and $N=3$ He^+ thresholds”. In: *Journal of Physics B: Atomic and Molecular Physics* 18.17 (Sept. 1985), pp. 3481–3486.
- [63] Misha Ivanov and Emilio Pisanty. *Taking control of polarization*. Nature Photonics, Vol. 8, 2014.
- [64] Yimeng Wang and Chris H. Greene. “Multichannel photoelectron phase lag across atomic barium autoionizing resonances”. In: *Phys. Rev. A* 105 (1 Jan. 2022), p. 013113.
- [65] J. Emsley. *The Elements*. Oxford Univ. Press, New York: Oxford Chemistry Guides, 1995.
- [66] Robert P. Wood, Chris H. Greene, and Darrell Armstrong. “Photoionization of the barium $6s6p\ ^1P^{\circ}_1$ state: Comparison of theory and experiment including hyperfine-depolarization effects”. In: *Phys. Rev. A* 47 (1 Jan. 1993), pp. 229–235.

- [67] Chris H. Greene and R. N. Zare. “Determination of product population and alignment using laser-induced fluorescence”. In: *The Journal of Chemical Physics* 78.11 (1983), pp. 6741–6753.
- [68] Andrew C. Kummel, Greg O. Sitz, and Richard N. Zare. “Determination of population and alignment of the ground state using two-photon nonresonant excitation”. In: *The Journal of Chemical Physics* 85.12 (1986), pp. 6874–6897.
- [69] David Herrick and Oktay Sinano ğlu. “Algebra of the Noncompact Group $O(3, 2)$ and the Hydrogen-Atom Radial Functions”. In: *Phys. Rev. A* 5 (6 June 1972), pp. 2309–2313.
- [70] C. D. Lin. “Classification and supermultiplet structure of doubly excited states”. In: *Phys. Rev. A* 29 (3 Mar. 1984), pp. 1019–1033.
- [71] B. G. Adams, J. Čížek, and J. Paldus. “Representation theory of $so(4,2)$ for the perturbation treatment of hydrogenic-type hamiltonians by algebraic methods”. In: *International Journal of Quantum Chemistry* 21.1 (1982), pp. 153–171.
- [72] A R P Rau. “Group theoretical treatments of strongly correlated atomic dynamics”. In: *Reports on Progress in Physics* 53.2 (Feb. 1990), pp. 181–220.
- [73] David R. Herrick and Oktay Sinano ğlu. “Comparison of doubly-excited helium energy levels, isoelectronic series, autoionization lifetimes, and group-theoretical configuration-mixing predictions with large-configuration-interaction calculations and experimental spectra”. In: *Phys. Rev. A* 11 (1 Jan. 1975), pp. 97–110.
- [74] H. R. Sadeghpour. “Nonadiabatic selection rules for the photoabsorption of H^- and He”. In: *Phys. Rev. A* 43 (11 June 1991), pp. 5821–5831.
- [75] M. Domke et al. “Extensive double-excitation states in atomic helium”. In: *Phys. Rev. Lett.* 66 (10 Mar. 1991), pp. 1306–1309.
- [76] H. R. Sadeghpour and Chris H. Greene. “Dominant photodetachment channels in H^- ”. In: *Phys. Rev. Lett.* 65 (3 July 1990), pp. 313–316.
- [77] Konstantin E Dorfman, Frank Schlawin, and Shaul Mukamel. “Nonlinear optical signals and spectroscopy with quantum light”. In: *Reviews of Modern Physics* 88.4 (2016), p. 045008.
- [78] Dong-Ik Lee and Theodore Goodson. “Entangled photon absorption in an organic porphyrin dendrimer”. In: *The Journal of Physical Chemistry B* 110.51 (2006), pp. 25582–25585.
- [79] Frank Schlawin, Konstantin E. Dorfman, and Shaul Mukamel. “Entangled Two-Photon Absorption Spectroscopy”. In: *Accounts of Chemical Research* 51.9 (2018). PMID: 30179458, pp. 2207–2214.

- [80] Bahaa E. A. Saleh et al. “Entangled-Photon Virtual-State Spectroscopy”. In: *Phys. Rev. Lett.* 80 (16 Apr. 1998), pp. 3483–3486.
- [81] Dmitry Strekalov et al. “Relationship between quantum two-photon correlation and classical spectrum of light”. In: *Phys. Rev. A* 71 (4 Apr. 2005), p. 041803.
- [82] Peter Pfeifer and Jürg Fröhlich. “Generalized time-energy uncertainty relations and bounds on lifetimes of resonances”. In: *Rev. Mod. Phys.* 67 (4 Oct. 1995), pp. 759–779.
- [83] Jan Peřina, Bahaa E. A. Saleh, and Malvin C. Teich. “Multiphoton absorption cross section and virtual-state spectroscopy for the entangled n -photon state”. In: *Phys. Rev. A* 57 (5 May 1998), pp. 3972–3986.
- [84] Hong-Bing Fei et al. “Entanglement-Induced Two-Photon Transparency”. In: *Phys. Rev. Lett.* 78 (9 Mar. 1997), pp. 1679–1682.
- [85] Ashok Muthukrishnan, Girish S. Agarwal, and Marlan O. Scully. “Inducing Disallowed Two-Atom Transitions with Temporally Entangled Photons”. In: *Phys. Rev. Lett.* 93 (9 Aug. 2004), p. 093002.
- [86] Marten Richter and Shaul Mukamel. “Collective two-particle resonances induced by photon entanglement”. In: *Phys. Rev. A* 83 (6 June 2011), p. 063805.
- [87] Jean-Philippe W MacLean, John M Donohue, and Kevin J Resch. “Direct characterization of ultrafast energy-time entangled photon pairs”. In: *Physical Review Letters* 120.5 (2018), p. 053601.
- [88] S Sofer et al. “Quantum enhanced X-ray detection”. In: *Physical Review X* 9.3 (2019), p. 031033.
- [89] Aaron T Bondy, Donald C Morton, and GWF Drake. “Two-photon decay rates in helium-like ions: Finite-nuclear-mass effects”. In: *Physical Review A* 102.5 (2020), p. 052807.
- [90] M. Lipeles, R. Novick, and N. Tolk. “Direct Detection of Two-Photon Emission from the Metastable State of Singly Ionized Helium”. In: *Phys. Rev. Lett.* 15.17 (Oct. 1965), pp. 690–693.
- [91] G. W. F. Drake, G. A. Victor, and A. Dalgarno. “Two-Photon Decay of the Singlet and Triplet Metastable States of Helium-like Ions”. In: *Phys. Rev.* 180 (1 Apr. 1969), pp. 25–32.
- [92] MH Prior. “Lifetime of the 2S State of He⁺”. In: *Physical Review Letters* 29.10 (1972), p. 611.

- [93] Paul H Mokler and Robert W Dunford. “Two-photon decay in heavy atoms and ions”. In: *Physica Scripta* 69.1 (2004), p. C1.
- [94] Robert S. Van Dyck, Charles E. Johnson, and Howard A. Shugart. “Radiative Lifetime of the 2^1S_0 Metastable State of Helium”. In: *Phys. Rev. A* 4 (4 Oct. 1971), pp. 1327–1336.
- [95] Yanhua Shih. “Entangled biphoton source - property and preparation”. In: *Reports on Progress in Physics* 66.6 (May 2003), pp. 1009–1044.
- [96] U. M. Titulaer and R. J. Glauber. “Correlation Functions for Coherent Fields”. In: *Phys. Rev.* 140 (3B Nov. 1965), B676–B682.
- [97] Christian G Parthey et al. “Improved measurement of the hydrogen 1 s–2 s transition frequency”. In: *Physical review letters* 107.20 (2011), p. 203001.
- [98] U Gaubatz et al. “Population transfer between molecular vibrational levels by stimulated Raman scattering with partially overlapping laser fields. A new concept and experimental results”. In: *The Journal of Chemical Physics* 92.9 (1990), pp. 5363–5376.
- [99] L. P. Yatsenko et al. “Stimulated hyper-Raman adiabatic passage. I. The basic problem and examples”. In: *Phys. Rev. A* 58 (6 Dec. 1998), pp. 4683–4690.
- [100] S. Guérin et al. “Stimulated hyper-Raman adiabatic passage. II. Static compensation of dynamic Stark shifts”. In: *Phys. Rev. A* 58 (6 Dec. 1998), pp. 4691–4704.
- [101] LP Yatsenko et al. “Two-photon excitation of the metastable 2 s state of hydrogen assisted by laser-induced chirped Stark shifts and continuum structure”. In: *Physical Review A* 71.3 (2005), p. 033418.
- [102] Peter L Knight, MA Lauder, and Bill Jack Dalton. “Laser-induced continuum structure”. In: *Physics Reports* 190.1 (1990), pp. 1–61.
- [103] Tiemo Landes et al. “Quantifying the enhancement of two-photon absorption due to spectral-temporal entanglement”. In: *Optics Express* 29.13 (2021), pp. 20022–20033.
- [104] Tiemo Landes et al. “Experimental feasibility of molecular two-photon absorption with isolated time-frequency-entangled photon pairs”. In: *Physical Review Research* 3.3 (2021), p. 033154.
- [105] Thomas Gaumnitz et al. “Streaking of 43-attosecond soft-X-ray pulses generated by a passively CEP-stable mid-infrared driver”. In: *Optics express* 25.22 (2017), pp. 27506–27518.
- [106] Joseph Duris et al. “Tunable isolated attosecond X-ray pulses with gigawatt peak power from a free-electron laser”. In: *Nature Photonics* 14.1 (2020), pp. 30–36.

- [107] Linda Young et al. “Femtosecond electronic response of atoms to ultra-intense X-rays”. In: *Nature* 466.7302 (2010), pp. 56–61.
- [108] Tenio Popmintchev et al. “Bright coherent ultrahigh harmonics in the keV x-ray regime from mid-infrared femtosecond lasers”. In: *science* 336.6086 (2012), pp. 1287–1291.
- [109] C. Hernández-García et al. “Zeptosecond High Harmonic keV X-Ray Waveforms Driven by Midinfrared Laser Pulses”. In: *Phys. Rev. Lett.* 111 (3 July 2013), p. 033002.
- [110] Langchi Zhu et al. “Coherent Laser Control of the Product Distribution Obtained in the Photoexcitation of *HI*”. In: *Science* 270.5233 (1995), pp. 77–80. ISSN: 0036-8075.
- [111] Hideki Ohmura, Taisuke Nakanaga, and M. Tachiya. “Coherent Control of Photofragment Separation in the Dissociative Ionization of *I*Br”. In: *Phys. Rev. Lett.* 92 (11 2004), p. 113002.
- [112] B. Sheehy, B. Walker, and L. F. DiMauro. “Phase Control in the Two-Color Photodissociation of *HD*⁺”. In: *Phys. Rev. Lett.* 74 (24 1995), pp. 4799–4802.
- [113] Hideki Ohmura, Naoaki Saito, and M. Tachiya. “Selective Ionization of Oriented Non-polar Molecules with Asymmetric Structure by Phase-Controlled Two-Color Laser Fields”. In: *Phys. Rev. Lett.* 96 (17 2006), p. 173001.
- [114] E. Dupont et al. “Phase-Controlled Currents in Semiconductors”. In: *Phys. Rev. Lett.* 74 (18 1995), pp. 3596–3599.
- [115] T. M. Fortier et al. “Carrier-Envelope Phase-Controlled Quantum Interference of Injected Photocurrents in Semiconductors”. In: *Phys. Rev. Lett.* 92 (14 2004), p. 147403.
- [116] Chao Zhuang et al. “Coherent Control of Population Transfer between Vibrational States in an Optical Lattice via Two-Path Quantum Interference”. In: *Phys. Rev. Lett.* 111 (23 2013), p. 233002.
- [117] Michael Förster et al. “Two-Color Coherent Control of Femtosecond Above-Threshold Photoemission from a Tungsten Nanotip”. In: *Phys. Rev. Lett.* 117 (21 2016), p. 217601.
- [118] D. W. Schumacher et al. “Phase Dependence of Intense Field Ionization: A Study Using Two Colors”. In: *Phys. Rev. Lett.* 73 (10 1994), pp. 1344–1347.
- [119] Leonardo Brugnera et al. “Trajectory Selection in High Harmonic Generation by Controlling the Phase between Orthogonal Two-Color Fields”. In: *Phys. Rev. Lett.* 107 (15 2011), p. 153902.

- [120] E. V. Gryzlova et al. “Coherent control of the photoelectron angular distribution in ionization of neon by a circularly polarized bichromatic field in the resonance region”. In: *Phys. Rev. A* 100 (6 2019), p. 063417.
- [121] Daehyun You et al. “New Method for Measuring Angle-Resolved Phases in Photoemission”. In: *Phys. Rev. X* 10 (3 2020), p. 031070.
- [122] Amalia Apalategui, Alejandro Saenz, and P. Lambropoulos. “Ab Initio Investigation of the Phase Lag in Coherent Control of H_2 ”. In: *Phys. Rev. Lett.* 86 (24 2001), pp. 5454–5457.
- [123] N. L. Manakov, V. D. Ovsiannikov, and Anthony F. Starace. “dc Field-Induced, Phase and Polarization Control of Interference between One- and Two-Photon Ionization Amplitudes”. In: *Phys. Rev. Lett.* 82 (24 1999), pp. 4791–4794.
- [124] P. Kalaitzis, D. Spasopoulos, and S. Cohen. “One- and two-photon phase-sensitive coherent-control scheme applied to photoionization microscopy of the hydrogen atom”. In: *Phys. Rev. A* 100 (4 2019), p. 043409.
- [125] Yimeng Wang and Chris H. Greene. “Resonant control of photoelectron directionality by interfering one- and two-photon pathways”. In: *Phys. Rev. A* 103 (5 May 2021), p. 053118.
- [126] Hossein R. Sadeghpour and Chris H. Greene. “Anisotropy of excited He^+ formed in the photoionization of helium”. In: *Phys. Rev. A* 39 (1 Jan. 1989), pp. 115–125.
- [127] Kurt W. Meyer, Chris H. Greene, and Brett D. Esry. “Two-Electron Photoejection of He and H^- ”. In: *Phys. Rev. Lett.* 78 (26 June 1997), pp. 4902–4905.
- [128] Kurt W. Meyer and Chris H. Greene. “Double photoionization of helium using R-matrix methods”. In: *Phys. Rev. A* 50 (5 Nov. 1994), R3573–R3576.
- [129] Langchi Zhu et al. “Effect of Resonances on the Coherent Control of the Photoionization and Photodissociation of HI and DI ”. In: *Phys. Rev. Lett.* 79 (21 1997), pp. 4108–4111.
- [130] Jeanette A. Fiss et al. “Origin of the Phase Lag in the Coherent Control of Photoionization and Photodissociation”. In: *Phys. Rev. Lett.* 82 (1 1999), pp. 65–68.
- [131] Yi-Yian Yin et al. “Asymmetric photoelectron angular distributions from interfering photoionization processes”. In: *Phys. Rev. Lett.* 69 (16 1992), pp. 2353–2356.
- [132] Takashi Nakajima, Jian Zhang, and P Lambropoulos. “Phase control through channels involving multiple continua and multiple thresholds”. In: *Journal of Physics B: Atomic, Molecular and Optical Physics* 30.4 (Feb. 1997), pp. 1077–1095.

- [133] P. Lambropoulos and Takashi Nakajima. “Origin of the Phase Lag in the Modulation of Photoabsorption Products under Two-Color Fields”. In: *Phys. Rev. Lett.* 82 (11 Mar. 1999), pp. 2266–2269.
- [134] Takashi Nakajima and P. Lambropoulos. “Effects of the phase of a laser field on autoionization”. In: *Phys. Rev. A* 50 (1 July 1994), pp. 595–610.
- [135] Tamar Seideman. “Phase-sensitive observables as a route to understanding molecular continua”. In: *The Journal of Chemical Physics* 111.20 (1999), pp. 9168–9182.
- [136] Takashi Nakajima and P. Lambropoulos. “Manipulation of the line shape and final products of autoionization through the phase of the electric fields”. In: *Phys. Rev. Lett.* 70 (8 Feb. 1993), pp. 1081–1084.
- [137] Tamar Seideman. “The role of a molecular phase in two-pathway excitation schemes”. In: *The Journal of Chemical Physics* 108.5 (1998), pp. 1915–1923.
- [138] P Camus et al. “Two-Step Optogalvanic Spectroscopy of Neutral Barium: Observation and Interpretation of the Even Levels Above the 6s Ionization Limit Between 5.2 and 7 eV”. In: *Physica Scripta* 27.2 (Feb. 1983), pp. 125–159.
- [139] K Maeda et al. “Absolute photoionization cross sections of the Ba ground state in the autoionization region: II. 221–209 nm”. In: *Journal of Physics B: Atomic, Molecular and Optical Physics* 33.10 (May 2000), pp. 1943–1966.
- [140] M Aymar. “Eigenchannel R-matrix calculation of the J=1 odd-parity spectrum of barium”. In: *Journal of Physics B: Atomic, Molecular and Optical Physics* 23 (1990), pp. 2697–2716.
- [141] G. Zürn et al. “Precise Characterization of ^6Li Feshbach Resonances Using Trap-Sideband-Resolved RF Spectroscopy of Weakly Bound Molecules”. In: *Phys. Rev. Lett.* 110 (13 Mar. 2013), p. 135301.
- [142] James P. Burke et al. “Impact of the ^{87}Rb singlet scattering length on suppressing inelastic collisions”. In: *Phys. Rev. A* 55 (4 Apr. 1997), R2511–R2514.
- [143] James P. Burke, Chris H. Greene, and John L. Bohn. “Multichannel Cold Collisions: Simple Dependences on Energy and Magnetic Field”. In: *Phys. Rev. Lett.* 81 (16 Oct. 1998), pp. 3355–3358.
- [144] Brandon P. Ruzic, Chris H. Greene, and John L. Bohn. “Quantum defect theory for high-partial-wave cold collisions”. In: *Phys. Rev. A* 87 (3 Mar. 2013), p. 032706.

- [145] Jesús Pérez-Ríos et al. “Quantum defect theory description of weakly bound levels and Feshbach resonances in LiRb”. In: *New Journal of Physics* 17.4 (Apr. 2015), p. 045021.
- [146] C. Marzok et al. “Feshbach resonances in an ultracold ${}^7\text{Li}$ and ${}^{87}\text{Rb}$ mixture”. In: *Phys. Rev. A* 79 (1 Jan. 2009), p. 012717.
- [147] R. A. W. Maier et al. “Efimov Resonance and Three-Body Parameter in a Lithium-Rubidium Mixture”. In: *Phys. Rev. Lett.* 115 (4 July 2015), p. 043201.
- [148] R. A. W. Maier et al. “Supplemental Material for Efimov Resonance and Three-Body Parameter in a Lithium-Rubidium Mixture”. In: *Phys. Rev. Lett.* 115 (4 July 2015), p. 043201.
- [149] Fang Fang et al. “Cross-dimensional relaxation of ${}^7\text{Li}$ – ${}^{87}\text{Rb}$ atomic gas mixtures in a spherical-quadrupole magnetic trap”. In: *Phys. Rev. A* 101 (1 Jan. 2020), p. 012703.
- [150] Fang Fang et al. “Collisional spin transfer in an atomic heteronuclear spinor Bose gas”. In: *Phys. Rev. Research* 2 (3 Aug. 2020), p. 032054.
- [151] C. Marzok et al. “Ultracold thermalization of ${}^7\text{Li}$ and ${}^{87}\text{Rb}$ ”. In: *Phys. Rev. A* 76 (5 Nov. 2007), p. 052704.

A. COLD COLLISIONS

The atomic cold collision problem is the basis to understanding the quantum behavior of particles, and is the most simple starting point to investigate universality for more complex system. In this Appendix, we will demonstrate our work on cold atomic collision, which used similar concepts and methods as introduced in Chap.2. Our calculations of Fano-Feshbach resonances and explanations towards the relaxation of ${}^7\text{Li}{}^{87}\text{Rb}$ will be discussed.

A.1 Cold collisions of ${}^7\text{Li}$ - ${}^{87}\text{Rb}$ and ${}^6\text{Li}$ - ${}^6\text{Li}$

Collisions between two atoms A and B can be modeled by the Hamiltonian:

$$\begin{aligned}
 H(\vec{R}, \omega) &= -\frac{\hbar^2}{2\mu} \nabla_{\vec{R}}^2 + U(R, \omega) + H_{spin}(\omega) \\
 U(R, \omega) &= U_X(R)P_X(\omega) + U_a(R)P_a(\omega) \\
 H_{spin}(\omega) &= H_{hf}(\omega) + H_Z(\omega) = \sum_{\beta=A,B} \alpha_{\beta} \vec{s}_{\beta} \cdot \vec{i}_{\beta} + (g_{s\beta} s_{z\beta} - g_{i\beta} i_{z\beta}) \mu_B B_z
 \end{aligned} \tag{A.1}$$

The Hamiltonian is defined in the center of mass reference frame, where \vec{R} is the spatial distance between the two atoms, and $\mu = \frac{m_A m_B}{m_A + m_B}$ is the reduced mass. The H_{spin} gives the interaction due to the spin configurations. ω includes all the nuclear and electronic spin degree of freedom and determines the channels of the collision.

The Born-Oppenheimer potential $U(R, \omega)$ is obtained from experimental fittings. $P_X(P_a)$ is the projection operator for electronic spin singlet (triplet) state, with $U_X(U_a)$ its correspondence potential curve. At a large distance, both $U_{X(a)}(R)$ converge to the same van der Waals tail $-\frac{C_6}{R^6}$, and it is H_{spin} that determines the threshold energy of each channel. \vec{s} and \vec{i} in Eq.A.1 denote the nuclear and electronic spin, α and $g_{s(i)}$ denote the hyperfine constant and g-factor for $\vec{s}(\vec{i})$, respectively, and μ_B is the Bohr magneton. No spin-orbit coupling is involved as both atoms are neutral.

The eigenstate of the spin manifold in Eq.A.1 is different for short- and long-distance of R (assuming magnetic field B is large):

$$|\omega\rangle = \begin{cases} |(s_A, s_B)S M_S, (i_A, i_B)I M_I\rangle^{(M)} & \text{short range} \\ |(s_A, i_A)f_A m_A, (s_B, i_B)f_B m_B\rangle^{(M)} & \text{long range} \end{cases} \quad (\text{A.2})$$

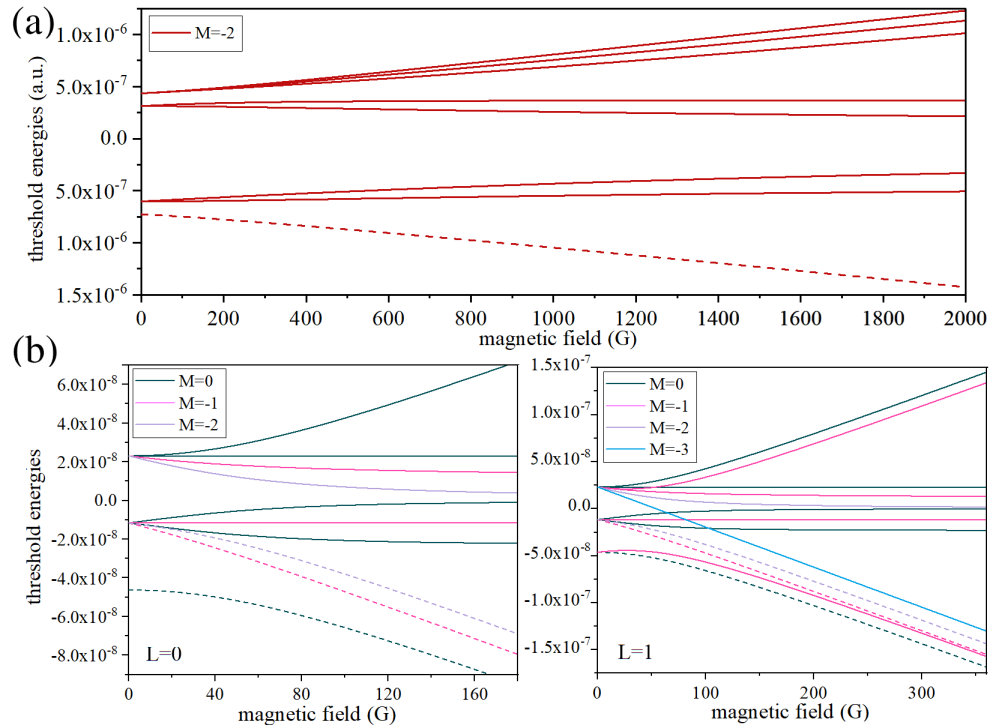


Figure A.1. Threshold energies for (a) ${}^7\text{Li}{}^{87}\text{Rb}$ for $M = -2$ manifold for arbitrary L and (b) ${}^6\text{Li}_2$ for $M = 0, -1, -2$ and -3 manifold for $L = 0, 1$. The dashed curves are the entrance channels in the experiments we compared with.

The division between “short” and “long” range depends on either $H_{spin}(\omega)$ or $|U_X(R) - U_a(R)|$ is negligible compared to the other. The (f_β, m_β) is the total angular momentum for a single-atom and its projection. The good quantum numbers of this system include the angular momenta of the atomic pair (L, M_L) the momentum $M = M_S + M_I = m_A + m_B$. For hetero-nucleus ${}^7\text{Li}{}^{87}\text{Rb}$, the values of L do not influence the size of spin configurations. We consider the experiment where both atoms in state $|f_\beta, m_\beta\rangle = |1, -1\rangle$ are loaded. This incident channel is the lowest one among the total 8 channels in the $M = -2$ subspace,

with the second-lowest threshold about $0.038K$ higher, therefore only single-channel elastic collision is involved. For homo-nucleus collision, the parity of L will influence the symmetry of the system and therefore affect the configuration space, which can be demonstrated by the case for two identical fermions ${}^6\text{Li}_2$. The eigen-energies for $H_{spin}(\omega)$ are computed and given in Fig. A.1.

Sometimes the spin-spin interaction and second-order spin-orbital interaction can be crucial to the system. They add an extra term, $H_{dd} = \frac{2}{3}\lambda(R)(3S_Z^2 - S^2)$ into H_{spin} , where $\lambda(R) \propto -\frac{3\alpha^2}{4R^3}$. This term is very weak and decays rapidly as R increases, therefore usually being neglected, but it couples between partial waves L and $L \pm 2$, which some times leads into extra Fano-Feshbach resonances. For the collision of ${}^7\text{Li}{}^{87}\text{Rb}$, the $s-d$ coupling gives a resonance feature at 535 G, where its conserved quantum number becomes $M_F = M + M_L$, and the spin configuration eigenstates is $|S M_S, I M_I, L M_L\rangle^{(M_F)} \xrightarrow{R \rightarrow \infty} |f_A m_A, f_B m_B, L M_L\rangle^{(M_F)}$. The lowest channels are two-fold degenerate $|f_A, m_A; f_B, m_B; L, M_L\rangle = |1, -1; 1, -1; 0(2), 0\rangle$, among total 47 channels in the $M_F = -2$ subspace.

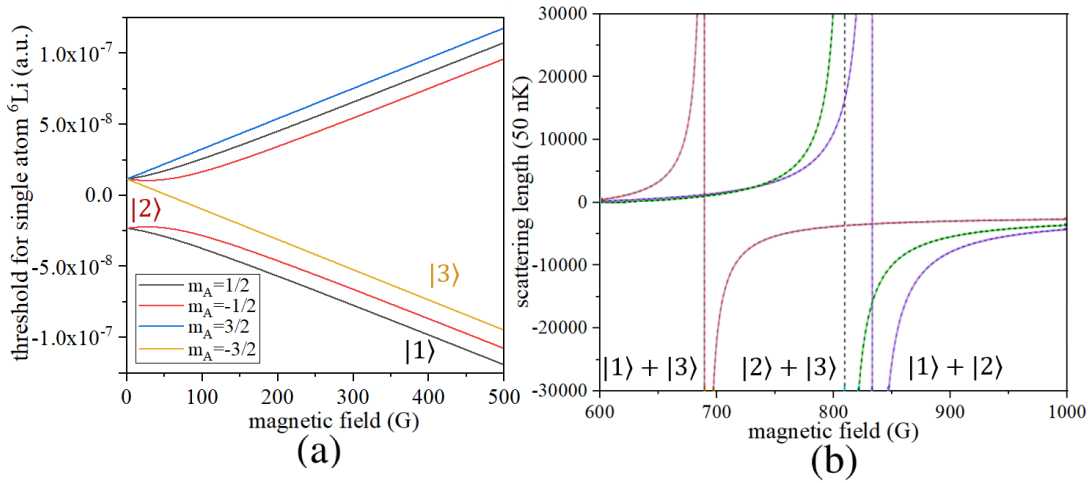


Figure A.2. (a) Threshold energies single ${}^6\text{Li}$ atom. (b) The s-wave scattering length near the ${}^6\text{Li}_2$ resonances for 1+3, 2+3, and 1+2 collision, our calculations (dashed lines) agree with the calculations from Ref. [141] supplemental material (solid lines).

Here we give some Fano-Feshbach resonance calculation of hetero-nucleus ${}^7\text{Li}{}^{87}\text{Rb}$ and homo-nucleus ${}^6\text{Li}_2$, both are carried out by the R matrix method with $R_0 = 8000 a.u.$,

and basis functions inside the reaction zone are constructed by the finite element method (FEM)[142] with more than 600 radial nodes. For ${}^7\text{Li}{}^{87}\text{Rb}$ collisions which have been carried out by many groups[143, 144, 145], we used model potentials (U_X, U_a) from Maier et al.[146] and we are able to reproduce the known Feshbach resonances at $B_{res} = 569.63$ G, 661.45 G (s-wave), 388.95 G, 445.97 G (p-wave), and 535.12 G (d-wave) at $9\mu\text{K}$ with $M = -2$, being consistent with previous calculations[146, 147] at 569.68 G, 661.34 G (s), 389.0 G, 446.0 G (p), and 535.09 (d), and experimental resonances at $B_{exp} = 569.49$ G, 661.53 G (s), 389.5 G, 447.4 G (p), and 534.97 G (d)[148]. For ${}^6\text{Li}_2$ calculations the Born-Oppenheimer potentials (U_X, U_a) are from Paul Julienne, we consider s-wave collision between particles in three different $|f_A, m_A\rangle$ channels: $|1\rangle = |1/2, 1/2\rangle, |2\rangle = |1/2, -1/2\rangle, |3\rangle = |3/2, -3/2\rangle$. our calculated Feshbach resonances for 1+3, 2+3, and 1+2 colliding process at 150 nK give, $B_{res}=690$ G ($M = -1$), 810 G ($M = -2$), and 832 G ($M = 0$) respective, which agree with previous calculation at 689.68 G, 809.76 G, and 832.18 G [141]. The s-wave scattering length $a_0 = -\lim_{k\rightarrow 0} \frac{\tan\delta(k)}{k}$ is given in Fig.A.2. For p-wave, there is no relevant two-body resonances have been found.

A.2 ${}^7\text{Li}{}^{87}\text{Rb}$ relaxation experiments

This part demonstrates our works in collaborating with experimentalists, about the cross-dimensional and the spin relaxation of ${}^7\text{Li}{}^{87}\text{Rb}$ atoms, which will be introduced by the following two subsections, respectively. Our works have been published at Ref.[149, 150], which include the contents of this section.

A.2.1 Comparison with cross dimensional relaxation experiments

This section compares our calculated cross-section at collision energies of several $100\mu\text{K}$ with the experimental measured cross-dimensional relaxation rate[149], where laser-cooled lithium and rubidium gases were loaded and trapped inside a spherical quadrupole magnetic trap. It is noted that the initial atomic momentum distribution in the trap is anisotropic from a mismatch between atoms and the trap and that the kinetic energy E_z along the axial trap direction is larger than that along with the radial directions $E_{x(y)}$ Over the timescales of the

B' (G/cm)	T_{Rb} (μ K)	$\tau^{(ex)}$ (s)	$\sigma_{cdr}^{(ex)}$ (cm^2)	$\tau^{(th)}$ (s)	$\sigma_{cdr}^{(th)}$ (cm^2)
328	223(2)	4.4(3)	$7.27(56) \times 10^{-12}$	4.9(1)	$6.56(29) \times 10^{-12}$
249	418.2(2)	28(4)	$8.5(1.1) \times 10^{-14}$	69(1)	$3.5(1) \times 10^{-14}$
170	297.7(1)	37(6)	$10.3(1.8) \times 10^{-14}$	95(2)	$4.0(2) \times 10^{-14}$

Table A.1. Measured cross-dimensional relaxation rates $\tau^{(ex)}$ and comparisons to theory for several experimental settings. Monte-Carlo simulations for atoms interacting via s-wave-only collisions with an energy-independent cross section, under conditions matching the experimental setting, are used to quantify the cross-dimensional relaxation cross sections $\sigma_{cdr}^{(ex)}$, which matches the experimental relaxation time $\tau^{(ex)}$, and $\sigma^{(th)}$, which matches the theoretically predicted relaxation time $\tau^{(th)}$. This table is from [149].

measurement, the lithium is not fully thermalized in the rubidium bath. The relaxation time $\tau^{(ex)}$ is determined by fitting the ratio of kinetic energies E_z/E_x which decays exponentially to equilibrium, $\frac{E_z}{E_x} = \frac{1+2\epsilon \exp(-t/\tau^{(ex)})}{1-\epsilon \exp(-t/\tau^{(ex)})}$, where ϵ quantifies the initial departure from equilibrium. With the relaxation time $\tau^{(ex)}$, one can obtain the cross-dimensional relaxation cross-section by, $\tau = \alpha \times \frac{32\pi(T_a+T_b)^3}{k^3 N_b \sigma_{cdr} v_{rel}}$, where $k = \mu B'/k_B$ and the ensemble-averaged relative velocity $v_{rel} = \sqrt{\frac{8k_B}{\pi} (\frac{T_a}{m_a} + \frac{T_b}{m_b})}$. The derivations and details of these formulae can be found in [149, 151]. In Table.A.1 we list both experimental measurements and our theory prediction. $\sigma_{cdr}^{(th)}$ is the theoretical cross-section assuming both Li and Rb gases have uniform density and are in thermal equilibrium at temperatures T_{Li} and T_{Rb} . It turns out that the measured collisional cross-section between ${}^7\text{Li}$ and ${}^{87}\text{Rb}$ atoms is much larger than the one predicted by Maier et al.'s potential, within the energy range probed in this experiment.

Table A.2. Candidates with largest and smallest cross section from alternative potentials

	χ_5^2	$B_{res}s$	$B_{res}p$	$B_{res}d$	$\sigma_T(418, 297\mu K)$
Experiment[148]	—	569.49 G 660.53 G	389.5 G 447.4 G	534.97 G	$8.5(1.1) \times 10^{-14} \text{ cm}^2$ $10.3(1.8) \times 10^{-14} \text{ cm}^2$
Model potential[146] $C_6 = 2550.04 \text{ a.u.}$	11.02	569.68 G 661.30 G	389.00 G 446.03 G	534.98 G	$3.51 \times 10^{-14} \text{ cm}^2$ $4.82 \times 10^{-14} \text{ cm}^2$
Potential with $\sigma_{largest}$ $C_6 = 2570.45 \text{ a.u.}$	19.31	569.00 G 661.86 G	388.69 G 445.93 G	535.00 G	$3.75 \times 10^{-14} \text{ cm}^2$ $5.14 \times 10^{-14} \text{ cm}^2$
Potential with $\sigma_{smallest}$ $C_6 = 2535.55 \text{ a.u.}$	14.80	570.01 G 660.33 G	389.21 G 445.96 G	536.08 G	$3.26 \times 10^{-14} \text{ cm}^2$ $4.49 \times 10^{-14} \text{ cm}^2$

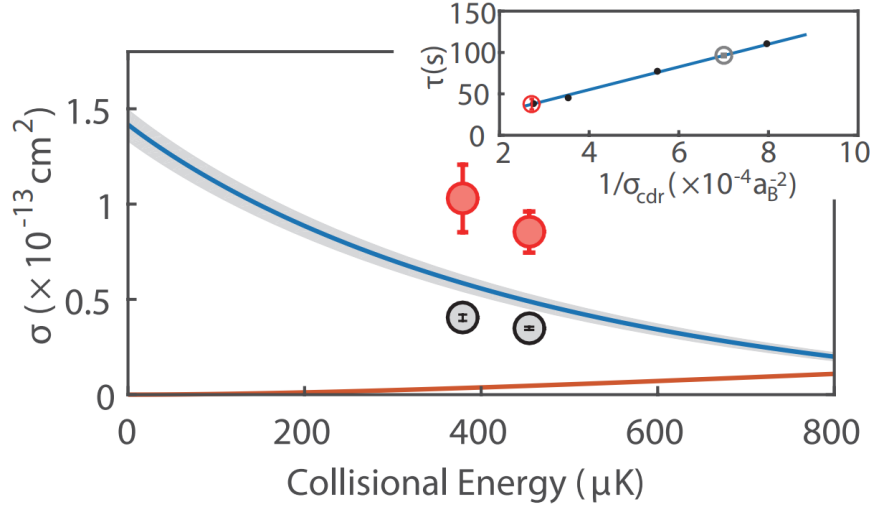


Figure A.3. Comparison of theoretical and experimentally determined cross section. Solid blue(orange) line is s(p) wave ${}^7\text{Li}{}^{87}\text{Rb}$ interspecies cross section calculated by quantum defect theory(QDT). Red circles represent σ_{cdr} determined by experimental measurements. Error bars are statistical. Blue circles are σ_{cdr} determined by Monte Carlo simulation using the theoretical differential cross section. Both the experimental and theoretical points are placed at the averaged collisional energy under experimental condition. Inset: Determine σ_{cdr} at through matching. Solid black spots are Monte-Carlo simulated results. The solid blue line is a linear fit: $\tau = k/\sigma_{cdr}$. The red circle represents experimental result. The blue circle represents Monte Carlo simulation. Reprint from [149].

The following part of this section describes the explorations we have carried out to modify the theoretical description of two-body Li-Rb scattering in a way that preserves existing agreement between theory and experimentally measured Fano-Feshbach resonance properties, while also agreeing with the present experimental results. Since the s-wave cross section decays rapidly with increasing energy (at zero energy, it gives $1.40 \times 10^{-13} \text{cm}^2$, but at 1.69 mK it goes to zero), it suggests the theoretical result might be rather sensitive to a small perturb of the potential curve. Therefore we hope slight modifications on the Born-Oppenheimer potential (U_x, U_a) from Maier et al.[146] could reconcile the difference.

We confirm that our calculation method is valid by using the Maier et al. model potentials and reproducing the calculated positions of several reported s-, p- and d-wave Fano-Feshbach resonances in ${}^7\text{Li}-{}^{87}\text{Rb}$. The agreement between these theoretical predictions and experimen-

tal findings is quantified by calculating $\chi_5^2 = \sum \frac{(B_{calc} - B_{exp})^2}{(\delta B)^2}$ where the sum is taken over the five measured Fano-Feshbach resonances, with B_{calc} being the theoretically predicted and B_{exp} the experimentally measured magnetic field position of the resonance, and $\delta B = 0.5G$ being the experimentally reported uncertainty. For the Maier et al. model potential, which was selected to match all experimental data on the $LiRb$ potential at the time of its publication (obviously excluding the present measurements), one finds $\chi_5^2 = 11$. The cross-sections predicted by the Maier et al. model potential are significantly smaller than that determined by measurement, as presented in Fig. A.3. Monte Carlo simulations using those results obtain a cross-dimensional relaxation cross-section (also in Fig. A.3) which is even smaller.

We explored the elasticity of the model predictions to variations in several model parameters, i.e., we explore to what extent the collision cross-section between 7Li and ${}^{87}Rb$, with both atoms in the $|F = 1; m_F = -1\rangle$ hyperfine state, can vary while maintaining agreement also with the measured Fano-Feshbach resonance positions. For this, we consider the following modifications of the two-body potential: a modification of the van der Waals coefficient C_6 that characterizes the long-range interaction, and modifications of the inner part of the spin-singlet (U_X) and triplet (U_a) potentials, i.e. adding the singlet(triplet) potentials a short-range term $c_{0(1)} \tan^{-1} [(R - R_{min})(R + R_{min})/4]$ before the potentials reach their minimum at $U(R_{min})$. After making such modifications, we recompute the predicted positions of the five Fano-Feshbach resonances and compare them with the Maier et al. measurements [146]. The details can be found in Table. A.2.

We consider modifications to the Li-Rb molecular potentials that remain somewhat consistent with the measured positions of the Fano-Feshbach resonances, where we qualify a modification as consistent so long as χ_5^2 remains of the same order as its value for the Maier et al. potential. Specifically, by assessing how the predicted Fano-Feshbach resonance predictions and also the thermally averaged cross-section vary linearly with the three potential model modifications, we determine model settings that produce the largest and smallest σ_T within the space bounded by $\chi_5^2 < 20$ (Fig. A.3 shaded area). We compute the full energy-dependent cross-section for these two model settings. As shown in Fig. A.3, constraining the model to remain consistent with the measured positions of the Fano-Feshbach resonances

permits only slight modifications, at the level of less than 10%, to the predicted collision cross-section and, similarly, to the predicted cross-dimensional relaxation rate. These modifications are insufficient to bridge the difference between the experimental findings and theoretical predictions. Overall, we conclude that the measured Fano-Feshbach resonance potentials and the measured cross-dimensional relaxation rate cannot all be made simultaneously consistent with present-day models of the $Li - Rb$ molecular potential.

A.2.2 Comparison with spin relaxation experiments

This section compares the calculated cross-section at collision energies around $50 \mu K$ with the experimentally measured spin relaxation rate[150], and the two results achieve good agreements (Table. A.3). The lithium and rubidium gases are loaded in a magneto-optical trap and polarized through element-selective optical pumping to initiate the spin dynamics, then evolved for a variable time of several seconds before the spin composition of each gas is measured. Since the number of rubidium atoms is 10 times larger than the number of lithium atoms, the Li-Li spin relaxation collision is negligible compared to Li-Rb. Besides, since the spin-changing Rb-Rb collisions are anomalously small, the co-trapped rubidium gas serves as a large magnetization reservoir whose spin distribution is kept constant during the experiment. As a result, only the change of lithium spin distribution $\underline{N}^{(Li)} = \left(N_{+1}^{(Li)} \quad N_0^{(Li)} \quad N_{-1}^{(Li)} \right)^T$ as an indicator of spin-dependent Li-Rb evolution is observed, which can be described through the rate equation,

$$\frac{d}{dt} \underline{N}^{(Li)} = -\frac{\underline{N}^{(Li)}}{\tau} + \underline{R} \underline{N}^{(Li)} \quad (\text{A.3})$$

where the matrix \underline{R} can be expressed by the rate for specific spin-changing collision Γ_α and the fraction of rubidium atoms in the incident spin state $p_{m_f, Rb}$ as,

$$\left(\begin{array}{ccc} -\Gamma_{se} p_0 - (\Gamma_{sm} + \Gamma_{qe}) p_{-1} & \Gamma_{se} p_{+1} + \Gamma_{sm} p_0 & \Gamma_{qe} p_{+1} \\ \Gamma_{se} p_0 + \Gamma_{sm} p_{-1} & -\Gamma_{se} (p_{+1} + p_{-1}) - 2\Gamma_{sm} p_0 & \Gamma_{se} p_0 + \Gamma_{sm} p_{+1} \\ \Gamma_{qe} p_{-1} & \Gamma_{se} p_{-1} + \Gamma_{sm} p_0 & -\Gamma_{se} p_0 - (\Gamma_{sm} + \Gamma_{qe}) p_{+1} \end{array} \right) \quad (\text{A.4})$$

For the experimental measured $F = 1$ manifold, there are three possible spin-changing of $|m_{f,Li}, m_{f,Rb}\rangle$ state, which are denoted as $\alpha = \{se, sm, qe\}$ in the equation, they are the spin exchange ($|0, -1\rangle \rightarrow |-1, 0\rangle$), spin mixing ($|-1, +1\rangle \rightarrow |0, 0\rangle$), and quadrupole exchange ($|+1, -1\rangle \rightarrow |-1, +1\rangle$). For a single $m_{f,Rb}$, $\Gamma_\alpha p = n^{(Rb)}\bar{v}\sigma_\alpha p$, where $n^{(Rb)}$ is the density of gas Rb atoms, $\bar{v} = \sqrt{\frac{8k_B}{\pi}(\frac{T_{Rb}}{m_{Rb}} + \frac{T_{Li}}{m_{Li}})}$ is the rms incident velocity, and σ_α is the cross section. The measured cross-sections $\sigma_{se,sm,qe}$ is therefore obtained by fitting the evolution of heteronuclear spin populations to Eq.A.3.

Table A.3. Comparison between experiment and theoretical calculations for three spin-dependent collision processes at $50\mu K$. This table is from [150].

Cross Section($\times 10^{-14}$ cm ²)	σ_{se}	σ_{sm}	σ_{qe}	σ_{se}/σ_{sm}
Experiment	2.4(7)	1.7(6)	0-0.5	1.4(6)
This work	2.2	1.8	0.02	1.2

The theoretical predictions of above processes are roughly described by the Fermi pseudopotential, with the scattering lengths $a_{F,M}$ being obtained by Maier et al.'s potential curves. Specifically, the cross-section can be obtained by, $\sigma_\alpha = 4\pi a_\alpha^2$ with $a_{se} = (a_{F=2,M=1} - a_{F=1,M=1})/2$, $a_{sm} = (a_{F=2,M=0} - a_{F=1,M=0})/3$ and $a_{qe} = (a_{F=2,M=0} - 3a_{F=1,M=0} + 2a_{F=0,M=0})/6$, which give the cross-sections listed in the second row of Table. A.3.

VITA

Yimeng Wang

Education

Purdue University, Ph.D, physics (August 2017 - May 2022)

Southern University of Science and Technology, B.S, physics (August 2013 - June 2017)

Publications

Yimeng Wang and Chris H. Greene, Multichannel photoelectron phase lag across atomic barium autoionizing resonances, *Phys. Rev. A*, 105, 013113 (2022)

Yimeng Wang and Chris H. Greene, Resonant control of photoelectron directionality by interfering one- and two-photon pathways, *Phys. Rev. A*, 103, 053118 (2021)

Yimeng Wang and Chris H. Greene, Two-photon above-threshold ionization of helium, *Phys. Rev. A*, 103, 033103 (2021)

Fang Fang, Joshua A. Isaacs, Aaron Smull, Katinka Horn, L. Dalila Robledo-De Basabe, Yimeng Wang, Chris H. Greene, and Dan M. Stamper-Kurn, Collisional spin transfer in an atomic heteronuclear spinor Bose gas, *Phys. Rev. Research* 2, 032054(R) (2020)

Fang Fang, Shun Wu, Aaron Smull, Joshua A. Isaacs, Yimeng Wang, Chris H. Greene, and Dan M. Stamper-Kurn, Cross-dimensional relaxation of ^7Li - ^{87}Rb atomic gas mixtures in a spherical-quadrupole magnetic trap, *Phys. Rev. A* 101, 012703 (2020)

Yimeng Wang, Zhen-Hua Wang, Wei-Qiang Chen, Nodal and nodeless gap in proximity induced superconductivity: application to monolayer CuO_2 on $\text{Bi}_2\text{Sr}_2\text{CaCu}_2\text{O}_{8+\delta}$ substrate, *Phys. Rev. B* 96, 104507 (2017)